Hot electron injection laser : variable carrier heating for high-speed, low-chirp direct modulation

Citation for published version (APA):
Hoskens, R. C. P. (2005). *Hot electron injection laser : variable carrier heating for high-speed, low-chirp direct modulation*. [Phd Thesis 1 (Research TU/e / Graduation TU/e), Electrical Engineering]. Technische Universiteit Eindhoven. https://doi.org/10.6100/IR594577

DOI:
10.6100/IR594577

Document status and date:
Published: 01/01/2005

Document Version:
Publisher's PDF, also known as Version of Record (includes final page, issue and volume numbers)

Please check the document version of this publication:

• A submitted manuscript is the version of the article upon submission and before peer-review. There can be important differences between the submitted version and the official published version of record. People interested in the research are advised to contact the author for the final version of the publication, or visit the DOI to the publisher's website.
• The final author version and the galley proof are versions of the publication after peer review.
• The final published version features the final layout of the paper including the volume, issue and page numbers.

Link to publication

General rights
Copyright and moral rights for the publications made accessible in the public portal are retained by the authors and/or other copyright owners and it is a condition of accessing publications that users recognise and abide by the legal requirements associated with these rights.

- Users may download and print one copy of any publication from the public portal for the purpose of private study or research.
- You may not further distribute the material or use it for any profit-making activity or commercial gain
- You may freely distribute the URL identifying the publication in the public portal.

If the publication is distributed under the terms of Article 25fa of the Dutch Copyright Act, indicated by the "Taverne" license above, please follow below link for the End User Agreement:

www.tue.nl/taverne

Take down policy
If you believe that this document breaches copyright please contact us at:

openaccess@tue.nl

providing details and we will investigate your claim.

Download date: 04. Oct. 2023

Hot Electron Injection Laser

Variable Carrier Heating for
High-Speed, Low-Chirp
Direct Modulation

Roger Hoskens

Hot Electron Injection Laser

Variable Carrier Heating for High-Speed, Low-Chirp Direct Modulation

PROEFSCHRIFT

TER VERKRIJGING VAN DE GRAAD VAN DOCTOR
AAN DE TECHNISCHE UNIVERSITEIT EINDHOVEN,
OP GEZAG VAN DE RECTOR MAGNIFICUS, PROF.DR.IR. C.J. VAN DUIJN,
VOOR EEN COMMISSIE AANGEWEZEN DOOR HET COLLEGE VOOR PROMOTIES
IN HET OPENBAAR TE VERDEDIGEN
OP DINSDAG 6 SEPTEMBER OM 16.00 UUR

door

Roger Cornelis Petrus Hoskens

geboren te Bladel

Dit proefschrift is goedgekeurd door de promotoren:

prof.dr. G.A. Acket

en

prof. C. Jagadish

Copromotor:
dr.ir. T.G. van de Roer

This work was supported by the Dutch Technology Foundation (STW).

The results reported in this thesis were realized in close cooperation with the Electronic Materials Engineering Department of the Australian National University in Canberra, Australia.

Printed by the University Press of the Technische Universiteit Eindhoven.
Cover illustration by Paul Verspaget.

CIP-DATA LIBRARY TECHNISCHE UNIVERSITEIT EINDHOVEN

Hoskens, Roger C.P.

Hot electron injection laser : variable carrier heating for high-speed, low-chirp direct modulation / by Roger Cornelis Petrus Hoskens. - Eindhoven : Technische Universiteit Eindhoven, 2005.
Proefschrift. - ISBN 90-386-1753-4
NUR 959
Trefw.: opto-elektronica / halfgeleiderlasers / laserdioden.
Subject headings: optoelectronic devices / semiconductor lasers / hot carriers.

a l'Ariadna
i / en
aan mijn ouders

Contents

1 Introduction

2 Carrier heating efficiency

3 Device design

4 Device fabrication

5 Device results

6 Discussion and recommendations

Chapter 1

Introduction

The novel Hot Electron Injection Laser (HEL), a three-terminal vertically integrated transistor-laser structure, is designed to investigate and possibly utilize the effects of carrier-heating on the optical gain and wavelength chirp. Simulations show the potential of carrier heating assisted gain switching to directly modulate the optical field intensity at frequencies up to 100GHz while minimizing the parasitic wavelength chirp. The HEL is designed to demonstrate these results through independent but complementary control over both the concentration and the energy of the electrons injected into the active layer.

1.1 Direct modulation of diode lasers

Due to the impact of low-loss optical fibers on lightwave telecommunications, the most important characteristic required from semiconductor lasers used as transmitters is modulation speed under single-mode operating conditions. The simplest modulation technique is direct intensity modulation where the pulse-shaped signal is imposed on the laser injection current. However, the resulting dynamic changes in carrier concentration give rise also to such unwelcome phenomena as relaxation oscillations in the carrier-photon system and wavelength chirping. The former limits the modulation rate and the latter, in combination with fiber dispersion, restricts the transmission distance. For these reasons, direct modulation is hardly acceptable for long-haul and high bit rate transmission systems and the development of modulation techniques surpassing these limitations is urgently needed. There are two alternative approaches to the above-mentioned problem. One solution is to connect an external modulator to the output of a stationary operating semiconductor laser. However, other problems are introduced: insertion loss and circuit complexity. Moreover, even external modulators have speed limits and cause phase modulation, by refractive index change or by optical feedback into the laser [1].

1.2 Complementary modulation using dynamic carrier heating

Another solution is to compensate for the parasitic effects associated with modulation of the pumping rate by influencing the active medium of a laser in some complementary way. Improvement of the internal modulation technique in such a manner can be a reasonable option provided a mechanism is present that exerts an influence opposing that of the carrier concentration. It was shown by recent studies that both gain and refractive index of semiconductor lasers are strongly dependent on the effective temperature of the thermalized electron-hole plasma as well as the carrier concentration. And since the thermalization time is of the order of one picosecond, gain switching via the temperature can be extremely fast. Thus, if a way can be found to modulate carrier temperature in a predetermined relation to concentration, improved modulation properties will result [2]-[9]. This raises the question on how the modulation response is influenced by concentration and temperature variations, which can only be answered by basic research on (sub)picosecond laser dynamics under carrier heating conditions. The effects of the carrier temperature have been studied through optical pump-probe experiments on semiconductor optical amplifiers [11] and on short cavity and vertical cavity surface emitting lasers [12]. Tunneling injection lasers try to avoid carrier heating by tunneling electrons directly into the active region [13], leading to a "colder" carrier distribution and thereby minimizing hot-carrier related issues.

The next question is by what means the desired combination of carrier density and carrier energy modulation can be achieved. Carrier heating effects can be used to our advantage and different mechanisms for direct and indirect carrier heating have been investigated. Gorfinkel et al. accomplished carrier heating in a conventional semiconductor laser through a lateral microwave electrical field using two additional topside ohmic contacts [2]. Balkan et al. introduced the HELLISH structure, which also uses an electric field parallel to an AlGaAs p-n junction to tunnel hot electrons into the GaAs quantum well [14]. Their design can result into a simpler VCSEL structure and bias-independent polarity of the optical emission. Another possibility to utilize carrier heating effects is the idea to inject electrons over some kind of launcher where their energy is increased and which can be controlled via an additional electrical contact. This can be a high-field region in the collector region of a heterojunction bipolar transistor (HBT) [10], a thin barrier positioned in the collector region of a hot electron transistor (HET) [15], a resonant-tunneling hot electron transistor [16] or a quantum-mechanical double barrier as in a resonant tunneling bipolar transistor (RBT) [17]. This thesis focuses on the first option in which the launcher is implemented using a high-field region inside the HBT’s collector region that accelerates the electrons before entering the laser’s active layer.

1.3 Proposed transistor-laser structure

Tolstikhin and Mastrapasqua proposed this novel three-terminal device structure employing the injection of hot electrons with tuned energy as a means to pump a semiconductor laser [10]. A vertically integrated structure results in which the emitter-base region of an HET, HBT or RBT is used to inject electrons into the active region of a laser diode. The emitter-base voltage of the transistor controls the pumping rate of the carriers injected into the laser, while the electron energy is governed, either by ballistic injection or by electric field heating, by the voltage applied between the base of the transistor and the p-type collector contact. In between these two the laser structure is positioned. Hot electrons entering the laser's active region lose their energy mainly due to intensive inter-carrier scattering, so within a very short thermalization time (usually < 0.3 ps) they increase the effective temperature of the electron-hole plasma. Thus, on a time-scale beyond the thermalization time, concentration and effective temperature of the electron-hole plasma can be controlled separately by two driving voltages, having different pulse shapes, combined in a suitable way. The material system to implement the proposed device is essentially determined by the spectral range of interest. Bearing in mind applications in optical communications, GaInAsP lattice matched to InP is the preferred system for a laser diode covering the important 1.3 and 1.55 micron wavelengths. This can be combined with an AlInAs/InGaAs structure for an HET or RBT, or an InGaAsP/InP launcher in case of an HBT. However, to rapidly demonstrate the feasibility of the proposed approach the AlGaAs/GaAs system is better since with this system considerable experience with lasers and transistors has been gained in the groups OED and HGF of the Technische Universiteit Eindhoven.

1.4 Prior art

Previous authors have suggested and implemented horizontal, meaning lateral, monolithically integrated transistor-laser structures to integrate the electrical driver circuit and the optical lasing cavity [18][19] even using selective epitaxial regrowth [20][21]. Such an approach has also been implemented for vertical-cavity surface-emitting lasers (VCSEL) [22]. The vertical integration of resonant tunneling structures [23][24] or heterojunction bipolar transistors [25] and diode lasers has also been proposed and partially implemented for the purpose of obtaining electrically controllable bistability in a laser. Bistability is obtained using the negative differential resistance (NDR) due to the tunneling effects. The vertical integration of an HBT transistor and a laser has also been implemented for the purpose of optoelectronic integration of the driver circuit [26]. Tolstikhin and Mastrapasqua proposed the first vertical integration of a transistor and a diode laser to modulate both the carrier density and the carrier temperature in a controllable and complementary way [10]. Their proposal was implemented and is the topic of this thesis.

References

[1] D. Marcuse and T.H. Wood, “Time-dependent simulation of a laser-modulator combination,” *IEEE J. Quantum Electron.*, vol. 30, pp. 2743-2755, 1994.

[2] T.Y. Bagaeva, I.I. Filatov, B.M. Gorbovitsky, and V.B. Gorfinkel, “High frequency modulation of quantum well heterostructure diode lasers by carrier heating in microwave electric field,” *Proc. of the 1991 International Device Research Symposium*, Hannover, 1991, pp. 403-406.

[3] V.B. Gorfinkel and I.I. Filatov, “Heating of an electron gas by an hf electric field in the active region of a semiconductor heterolaser,” *Sov. Phys. Semicond.*, vol. 24, pp. 466-469, 1990.

[4] V.B. Gorfinkel, B.M. Gorbovitsky, and I.I. Filatov, “High frequency modulation of light output power in double-heterojunction laser,” *Int. J. of Infrared and Millimeter Waves*, vol. 12, pp. 648-658, 1991.

[5] V.I. Tolstikhin, “High frequency modulation of GaInAsP/InP injection lasers with hot charge carriers,” *Sov. Tech. Phys. Lett.*, vol. 18, pp. 630-632, 1992.

[6] V.B. Gorfinkel and S. Luryi, “Rapid modulation of interband optical properties of quantum wells by intersubband absorption,” *Appl. Phys. Lett.*, vol. 60, pp. 3141-3143, 1992.

[7] V.B. Gorfinkel and S. Luryi, “High-frequency modulation and suppression of chirp in semiconductor lasers,” *Appl. Phys. Lett.*, vol. 62, pp. 2923-2925, 1993.

[8] V.I. Tolstikhin and M. Willander, “Competition between carrier concentration and temperature influences on gain as means for improving modulation response of semiconductor laser,” *J. Appl. Phys.*, vol. 77, pp. 488-493, 1995.

[9] V.I. Tolstikhin and M. Willander, “Carrier heating effects in dynamic-single-frequency GaInAsP-InP laser diodes,” *IEEE J. Quantum Electron.*, vol. 31, pp. 814-832, 1995.

[10] V.I. Tolstikhin and M. Mastrapasqua, “Three-terminal laser structure for high-speed modulation using dynamic carrier heating,” *Appl. Phys. Lett.*, vol. 67, pp. 3868-3870, 1995.

[11] A.P. de Boer, P.C.M. Christianen, J.C. Maan, Th. Rasing, V.I. Tolstikhin, T.G. van de Roer, and H.M. de Vrieze, “Amplified spontaneous emission spectroscopy on semiconductor optical amplifiers subject to active light injection,” *Appl. Phys. Lett.*, vol. 72, pp. 2936-2938, 1998.

[12] O.D. Mücke and M. Wegener, “Hot carrier induced picosecond dynamics of a vertical cavity surface emitting laser: influence of transverse effects,” *Appl. Phys. Lett.*, vol. 73, pp. 569-571, 1998.

[13] X. Zhang, A. Gutierrez-Aitken, D. Klotzkin, P. Bhattacharya, C. Caneau, and R. Bhat, “0.98-mm multiple-quantum-well tunneling injection laser with 98-GHz intrinsic modulation bandwidth,” *IEEE J. Sel. Topics in Quantum Electron.*, vol. 3, pp. 309-314, 1997.

[14] N. Balkan, A. Serpenguzel, A. O'Brien-Davies, I. Sokmen, C. Hepburn, R. Potter, M.J. Adams, and J.S. Roberts, “VCSEL structure hot electron light emitter,” *Materials Science and Engineering B*, vol. 74, pp. 96-100, 2000.

[15] M. Heiblum and M. Fischetti, “Ballistic Electron Transport in Hot electron transistors,” in: F. Capasso (ed.), *Physics of Quantum Electron Devices*, Springer, Berlin, 1990.

[16] N. Yokoyama, K. Imamura, H. Ohnishi, T. Mori, S. Muto, and A. Shibatomi, “Resonant-Tunneling Hot Electron Transistor (RHET),” *Solid-State Electron.*, vol. 31, pp. 577-582, 1988.

[17] T. Futatsugi, Y. Yamaguchi, K. Imamura, S. Muto, and N. Yokoyama, “A Resonant-Tunneling Bipolar Transistor (RBT) - A New Functional Device with high Current Gain,” *Jap. J. Appl. Phys.*, vol. 26, pp. L131-L133, 1987.

[18] K.Y. Liou, S. Chandrasekhar, A.G. Dentai, E.C. Burrows, G.J. Qua, C.H. Joyner, and C.A. Burrus, “A 5 Gb/s monolithically integrated lightwave transmitter with 1.5μm multiple quantum well laser and HBT driver circuit,” *IEEE Photon. Technol. Lett.*, vol. 3, pp. 928-930, 1991.

[19] X. Li, J.L. Jimenez, M.J. Jurkovic, and W.I. Wang, “Novel approach for integration of an AlGaAs/GaAs heterojunction bipolar transistor with an InGaAs quantum wel laser,” *Proc. SPIE*, vol. 3006, pp. 126-133, 1997.

[20] X. An, H. Temkin, A. Feygenson, R.A. Hamm, M.A. Cotta, R.A. Logan, D. Coblentz, and R.D. Yadvish, “Monolithic integration of InGaAsP/InP lasers and heterostructure bipolar transistors by selective area epitaxy,” *Electron. Lett.*, vol. 29, pp. 645-646, 1993.

[21] D.B. Slater Jr., P.M. Enquist, J.A. Hutchby, F.E. Reed, A.S. Morris, R.M. Koblas, R.J. Trew, A.S. Lujan, and J.W. Swart, “Monolithically integrated SQW laser and HBT laser driver via selective OMVPE regrowth,” *IEEE Photon. Technol. Lett.*, vol. 5, pp. 791-794, 1993.

[22] U. Eriksson, P. Evaldsson, and K. Streubel, “Fabrication of a 1.55-μm VCSEL and an InGaAsP-InP HBT from a common epitaxial structure,” *IEEE Photon. Technol. Lett.*, vol. 11, pp. 403-405, 1999.

[23] I. Grave, S.C. Kan, G. Griffel, S.W. Wu, A. Sa’ar, and A. Yariv, “Monolithic integration of a resonant tunneling diode and a quantum well semiconductor laser,” *Appl. Phys. Lett.*, vol. 58, pp. 110-112, 1991.

[24] F. Jain, C. Chung, R. LaComb, and M. Gokhale, “Resonant-tunneling transistor lasers: a new approach to obtain multi-state switching and bistable operation,” *Int. J. of Infrared and MM Waves*, vol. 14, pp. 1311-1322, 1993.

[25] T.R. Chen, K. Utaka, Y. Zhuang, Y. Liu, and A. Yariv, “A vertical monolithic combination of an InGaAsP/InP laser and a heterojunction bipolar transistor,” *IEEE J. Quantum Electron.*, vol. 23, pp. 919-924, 1987.

[26] U. Eriksson, P. Evaldsson, J. Wallin, B. Stalnacke, S. Lourdudoss, and B. Willen, “Vertical integration of an InGaAs/InP HBT and a 1.55μm strained MQW p-substrate laser,” *IEE Proceedings-Optoelectronics*, vol. 143, pp. 107-109, 1996.

Chapter 2

Carrier heating efficiency

THE HOT ELECTRON INJECTION LASER UTILIZES A STRONG ELECTRIC FIELD TO ACCELERATE THE ELECTRONS AND DISTRIBUTES THEIR ENERGY INSIDE THE ACTIVE LAYER. THERE THE ENERGY IS USED TO MODULATE THE MATERIAL GAIN AND TO CONTROL THE WAVELENGTH CHIRP. THE ELECTRONS ARE HEATED AND COOLED BY INCREASING OR DECREASING THE ENERGY OF THE INJECTED CARRIERS. BOTH THE EFFECTIVENESS OF THE LAUNCHER TO INCREASE THE TEMPERATURE OF THE ELECTRONS INSIDE THE ACTIVE LAYER AS WELL AS THE EFFECT OF HIGHER ELECTRON TEMPERATURES ON THE MATERIAL GAIN ARE INVESTIGATED HERE.

2.1 Heating and cooling of electrons

Hot electrons have an effective energy larger than the thermal Fermi energy kT_l with T_l the lattice temperature. A single volt across present-day submicron semiconductor devices introduces an electric field above 10^4 V/cm, which is generally enough to create hot electrons. This chapter will investigate the heating and cooling of these electrons and their effect on the optical gain as well as the wavelength chirp. Carrier heating occurs through an applied electric field, an externally applied photon field called optical pumping, multi-particle recombination processes like Auger recombination, and through stimulated emission. The same carriers cool down, i.e. dissipate energy, by emitting phonons, exciting other electrons through various scattering mechanisms, and also by emitting photons. The actual contribution of the emitted photons to the average energy of the electron ensemble thus depends on the emitted wavelength relative to the electron energy distribution function. Stimulated emission generally originates from around the bandgap and therefore results in a net heating of the remaining pool of electrons. Spontaneous emission on the other hand can lead to a net cooling of the electrons if it originates from the high energy band tail.

2.2 Carrier transport

The behavior of semiconductor devices can be described using any combination of the Hamiltonian equation for the classical mechanics, the Schrödinger equation for the quantum effects, the Boltzmann transport equation describing the carrier statistics and Maxwell's equations describing the electromagnetics [2]. The exact combination and the specific application will determine the deviation between the modelled behavior and the actual device results. The device behavior involving hot electrons requires a description of the gain and the relaxation of the carrier's momentum and energy. It can be approximated by the deterministic hydrodynamic model, also known as the energy relaxation model. This model is an extension of the standard drift-diffusion model and introduces the electron temperature T_e for which one additional differential equation is added to the set of coupled non-linear differential equations [5]. Within this approach the physics are still described using parameterized carrier and energy properties like mobilities, diffusion constants and lifetimes, which now also depend on the electron temperature T_e [3].

The drift-diffusion model will fail if the steady-state correlation between electric field and velocity $v(\boldsymbol{E})$ is not be reached due to high modulation frequencies or small device dimensions (<0.5µm) [5]. For example when describing the electron transport across the 140nm thin launcher under the influence of a high electric field. The electric field will accelerate the electrons in the same forward direction at first but different scattering mechanisms will randomize their wave vector $\boldsymbol{k}$ to a certain degree. The steady state $v(\boldsymbol{E})$ relationship will not be reached before they leave the launcher and enter the active layer.

More fundamental methods are needed to describe both the kinematics (the band structure properties) and the dynamics (the scattering mechanisms) of such quasi-ballistic carrier transport [3]. The most popular direct application of the physics involved is the stochastic approach called the ensemble Monte Carlo method (EMC), which combines the Boltzmann transport equation (BTE), numerous additional quantum effects and Poisson's equation for device simulations [6]. The ensemble of carriers is characterized by the distribution function $f(\boldsymbol{u}, \boldsymbol{r}, t)$ describing their statistical distribution across the velocity coordinates $\boldsymbol{u} = (u_x, u_y, u_z)$ and the space coordinates $\boldsymbol{r} = (r_x, r_y, r_z)$ since neither can be known exactly at a certain moment in time according to the Heisenberg uncertainty principle [5]. The Boltzmann transport equation is based on this distribution and its interaction with the outside world, i.e. acceleration through electric or magnetic fields and interactions with the lattice. Its higher moments n, $\boldsymbol{v}$, E, and $\boldsymbol{Q}$ are defined as [5]:

- the carrier density in real space

$$n(\boldsymbol{r}, t) = \iiint f(\boldsymbol{k}, \boldsymbol{r}, t) dk_x dk_y dk_z \qquad 2.1$$

- the average velocity

$$\boldsymbol{v}(\boldsymbol{r}, t) = \frac{1}{n}\iiint \boldsymbol{u}(\boldsymbol{k}) f(\boldsymbol{k}, \boldsymbol{r}, t) dk_x dk_y dk_z \qquad 2.2$$

- the average energy

$$E(\boldsymbol{r}, t) = \frac{1}{n}\iiint E(\boldsymbol{k}) f(\boldsymbol{k}, \boldsymbol{r}, t) dk_x dk_y dk_z \qquad 2.3$$

- the heat flow vector $\boldsymbol{Q}$

$$\boldsymbol{Q}(\boldsymbol{r}, t) = \frac{1}{n}\iiint \boldsymbol{u}(\boldsymbol{k}) E(\boldsymbol{k}) f(\boldsymbol{k}, \boldsymbol{r}, t) dk_x dk_y dk_z \qquad 2.4$$

where $\boldsymbol{Q}$ denotes the deviation from a Maxwellian distribution and is connected to the anisotropy of the distribution function. Multiplying the Boltzmann transport equation with $E(\boldsymbol{k})$, integrating it and assuming an isotropic parabolic energyband results in the transport equation for the average electron energy E [5]:

$$\frac{\partial E}{\partial t} + \boldsymbol{v} \cdot \nabla E - q\boldsymbol{v} \cdot \boldsymbol{E} + \frac{1}{n}\nabla \cdot (\boldsymbol{v}nkT_e + \boldsymbol{Q}) = \left(\frac{\partial E}{\partial t}\right)_c \qquad 2.5$$

which is directly related to the electron temperature T_e:

$$E = \frac{3}{2}kT_e + \frac{1}{2}mv^2 \qquad 2.6$$

Equation 2.5 contains both the gain term $q\boldsymbol{v} \cdot \boldsymbol{E}$ due to the applied electric field and the energy loss term $\left(\frac{\partial E}{\partial t}\right)_c$ due to the various scattering mechanisms, e.g. loss of energy to the lattice through collisions with phonons. The effectiveness of the launcher in heating the reservoir of electrons inside the active layer is directly linked to the balance between the energy gained through acceleration of the carriers within its electric field and the energy lost through various scattering mechanisms. From an application point of view, the various processes which decrease the carrier heating induced gain modulation include collisions with phonons that result in a transfer of energy and carrier-carrier interactions, which result in a spatial transfer of energy outside the optical mode. The carrier-phonon interactions are explained below; the spatial alignment between the hot electrons and the optical mode will be described in a subsequent chapter.

Hot carriers can emit both acoustic and optical phonons. Collisions involving long wavelength acoustic phonons with frequencies down to zero result in very little transfer of energy but do lead to a redistribution of the momentum. Polar optical phonons on the other hand, with a minimum energy of 36meV for the Γ-valley in GaAs, result in a redistribution of both energy and momentum, and therefore in the relaxation of both electron energy and momentum. Strong polar materials like GaAs, arising from the two types of atoms in the lattice, combined with the low effective mass of the electrons inside the Γ-valley, $m_e/m_0 = 0.067$, result in predominantly polar optical scattering. The L- and X-valleys show higher effective masses and higher density of states and acoustic scattering also becomes an important scattering mechanism [2].

The transfer of momentum and energy through carrier-carrier interactions takes place on timescales shorter than 300fs [16]. The cooling of the electron ensemble through carrier-phonon interactions takes place on slightly longer timescales and can be in the order of several picoseconds due to hot phonon effects [17][18]. Values of 3ps have been predicted and measured for pure GaAs at low electric fields, <1kV/cm, like in our active layer [10]. These values still predict carrier heating assisted gain switching to sustain modulation frequencies of at least 100GHz.

2.3 Electric field induced carrier heating

2.3.1 The ensemble Monte Carlo method

Equation 2.5 still poses two problems: the unknown higher order moment $\boldsymbol{Q}$ and the fact that AlGaAs has three energy valleys Γ, L and X, each with their own distribution $f(\boldsymbol{u}, \boldsymbol{r}, t)$. In fact, three similar equations have to be drawn up for each subband and an extra term is added to describe intervalley transfers [5]. These intervalley transfers involve a phonon and generally result in a substantial transfer of momentum but minimal transfer of energy. Intervalley transfers therefore do not result so much in a loss of energy but more in a delay within the carrier heating and cooling processes. Values of $\tau_{\Gamma\mathrm{L}} = 0.54 \pm 0.12\,\mathrm{ps}$ and $\tau_{\Gamma\mathrm{X}} = 0.18 \pm 0.04\,\mathrm{ps}$ are given in literature [10]. Furthermore, $\boldsymbol{Q}$ can be set to zero to ignore any anisotropy of the distribution function [5]. Several other simplifications should be made before any direct solution of the Boltzmann transport equation might come within reach.

A more practical approach towards a solution for the Boltzmann transport equation is the general mathematical procedure called the Monte Carlo method, actually named after the famous gambling city, originally developed by Fermi, von Neumann and Ulam for the Manhattan project but introduced for high-field transport in semiconductors by Kurosawa [11][1]. Jacoboni and Reggiani introduced the first simplified model for the band structure into the Monte Carlo method [7]. For additional references regarding the Monte Carlo method see [3][8][9].

Within the MC method, each electron is followed through its life cycle consisting of free flight influenced by external forces like electric or magnetic fields and interrupted by scattering events [5]. The course the carrier follows and thus the length of the free flight, the type of scattering mechanism and the outcome of the collision is chosen randomly according to their respective probability distributions [5]. An ensemble of at least 10^4 electrons should be included in the Monte Carlo simulation for this method to approximate the solution of the Boltzmann transport equation [5]. The main advantage of the Monte Carlo method is its ability to include complex band structures including non-parabolicity and multiple subvalleys, various scattering mechanisms and different quantum effects.

2.3.2 Electron heating versus hole heating

Both electrons and holes could be accelerated through the launcher to gain kinetic energy and subsequently distribute their excess energy within the active layer. Light holes also have a low effective mass, $m_l/m_0 = 0.083$, and are heated up substantially. The light hole band on the other hand overlaps with the heavy hole band inside the valence band and the light holes easily scatter to the heavy hole band. Heavy holes have a higher effective mass, $m_h/m_0 = 0.59$ and are therefore much slower in gaining speed through the launcher's electric field. Their transit time through the launcher is longer and chances of scattering increases. They also tend to loose their energy quicker through a shorter energy relaxation constant. This results in the fact that holes are generally less efficient in transferring energy to the reservoir of carriers inside the active layer.

2.3.3 The launcher's carrier heating efficiency

Section 2.2 showed us that the electrons gain energy ballistically in a mainly forward directed momentum. This means that the transfer and randomization of momentum is relatively slow compared to the gain of energy. It also means that the energy distribution of the electron ensemble inside the launcher cannot strictly be described by an average electron temperature [1]. Once inside the active layer, the electrons will stop gaining energy and start distributing their energy and momentum throughout the reservoir of electrons already present there through very fast carrier-carrier scattering. These interactions drive them towards a quasi-Fermi-Dirac distribution again and their energy distribution within the active layer can therefore be described using the electron temperature T_e [3]:

$$f_c(E, \boldsymbol{r}, t) = \frac{1}{1 + \exp\left(\frac{E - E_{fn}(\boldsymbol{r}, t)}{k_B T_e}\right)} \qquad 2.7$$

We are interested in the ability and the efficiency of the launcher-like structure to accelerate electrons which will heat up the electron energy distribution inside the active layer. A one-dimensional Monte Carlo routine is used to obtain estimates for the launcher's carrier heating efficiency. The base-launcher-active layer region is mimicked using a quasi-neutral base consisting of a high concentration of positively charged donor ions as an electron emitter suitable for Monte Carlo simulations. The launcher is basically a 140nm thin $Al_{0.3}Ga_{0.7}As$ layer either non-intentionally doped (NID) or with very low n-type doping. The active region itself is a NID 100nm GaAs bulk active layer. The electron scatter plot of figure 2.1 shows the distribution of the electrons throughout the three conduction band energy valleys Γ, L and X after applying an external voltage of one volt between the base and the collector or p-cladding and observing $4x10^4$ electrons during a timeframe of 2.5ns [4].

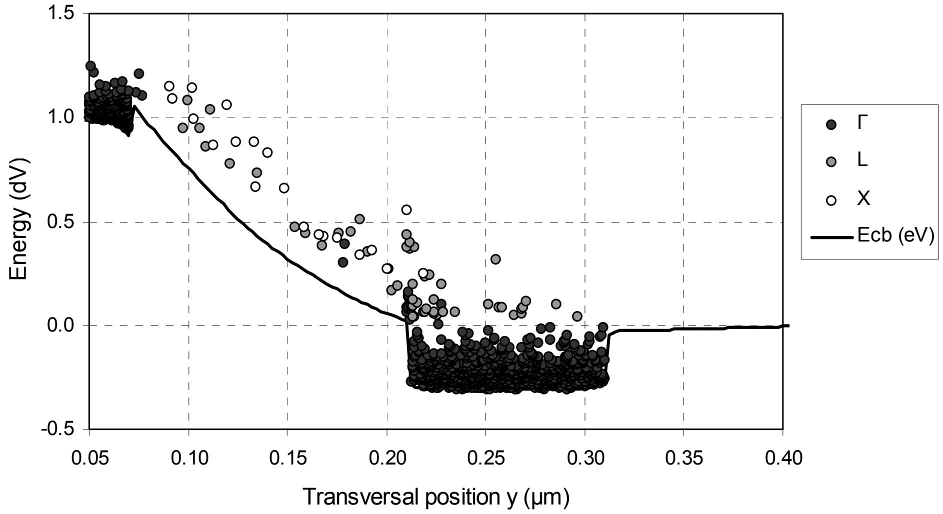

Figure 2.1: Simulated electron scatter diagram using the Monte Carlo method showing the energy distribution across the Γ, L *and* X *subbands within the launcher and active layer region for a standard* $Al_{0.30}Ga_{0.70}As$ *launcher (T.G. van de Roer, private communication)*

As soon as the electrons enter the launcher, the majority of them transfer into the upper valleys due to the energy they acquire, the much smaller energy separations between the Γ-L and Γ-X valleys in $Al_{0.3}Ga_{0.7}As$, as shown in table 2.1, and the higher density of states in the upper valleys.

Table 2.1: The energy separations between the Γ-L *and* Γ-X *valley minima for GaAs and* $Al_{0.3}Ga_{0.7}As$

Energy separation (eV)	GaAs	$Al_{0.3}Ga_{0.7}As$
$E_{\Gamma L}$	0.286	0.113
$E_{\Gamma X}$	0.476	0.146

Directly after entering the active layer, the electrons start distributing their energy between the existing reservoir of electrons and dissipating their energy through various electron-phonon interactions. These hot electrons start dissipating their energy and momentum and transfer back into the Γ-valley. These events increase the average energy of the ensemble, kT_e, and thus the electron temperature of the energy distribution function as shown in figure 2.2.

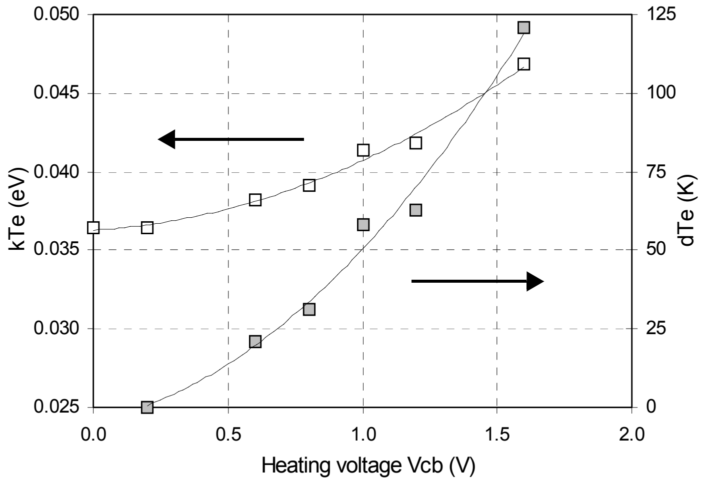

Figure 2.2: *Simulated carrier heating efficiency using the Monte Carlo method for a standard* $Al_{0.30}Ga_{0.70}As$ *launcher indicating the elevated Fermi energy* (kT_e) *and relative increase in electron temperature* (δT_e) *versus the heating voltage applied across the launcher (T.G. van de Roer, private communication)*

These results indicate that the current concept which uses a high electric field across a thin and lowly doped AlGaAs layer to launch the electrons can heat the electron ensemble within the quasi-neutral active layer by approximately 4.5meV or 50K per volt applied across the launcher. Using a GaAs launcher would minimize the transfers between the different conduction band energy valleys, making the heating and cooling of the electron ensemble more direct and thus faster but would at the same time be unsuitable for the optical application we intend to realize here due to the strong reduction in optical waveguiding as explained in the next chapters.

2.4 Carrier heating induced gain switching

From the application point of view, we also need to know the effect the previously estimated carrier heating has on the optical behavior. The plane-wave propagation constant β is related to the complex dielectric constant $\varepsilon = \varepsilon' + i\varepsilon''$ and the complex index of refraction μ like [12]:

$$\beta = k_0\sqrt{\varepsilon} = k_0\mu \qquad 2.8$$

with $k_0 = \omega/c$ the vacuum wave number and μ written as:

$$\mu = n + i\frac{\alpha}{2k_0} \qquad 2.9$$

where n is the refractive index and α the absorption coefficient. Combining both equations yields:

$$n = \sqrt{\varepsilon'} \qquad 2.10$$

$$\alpha = \frac{k_0\varepsilon''}{n} \qquad 2.11$$

The energy-dependent optical absorption coefficient $\alpha(E)$, or gain beyond population inversion, can be expressed as the product of the conduction and valence band Fermi-Dirac distribution functions $f_c(E)$ and $f_v(E)$, the density of states function $\rho(E)$ and the transition probability [12]:

$$\alpha(E, N_e, T_e) = \frac{\pi q^2 h |M_b|^2}{4\pi^2 \varepsilon_0 m_0^2 c \bar{n} E}\left(\frac{2m_r}{\bar{h}^2}\right)^{3/2}(E-E_g)^{1/2}[1-f_c(E_c)-f_v(E_v)] \qquad 2.12$$

where $E = \bar{h}\omega$ the photon energy. E_c and E_v are defined as:

$$E_c = \frac{m_r}{m_c}(E-E_g) \qquad 2.13$$

$$E_v = \frac{m_r}{m_{hh}}(E-E_g) \qquad 2.14$$

and the reduced mass m_r is given by:

$$m_r = \frac{m_c m_{hh}}{m_c + m_{hh}} \qquad 2.15$$

The square root of the summed energy offset $(E-E_g)^{1/2}$ in equation 2.12 originates from the density of states function. Important to us is the shape of the conduction band distribution function:

$$f_c(E, N_e, T_e) = \frac{1}{1 + \exp\left(\frac{E - E_{fn}(N_e)}{k_B T_e}\right)} \qquad 2.16$$

The total number of electrons inside the active layer is given by:

$$N_e = \int n(E)\partial E = \int \rho_c(E) f_c(E, N_e, T_e)\partial E \qquad 2.17$$

And unless otherwise stated, a quasi-neutral active layer is assumed meaning that for an undoped active layer the total number of electrons inside the conduction band equals the total number of holes inside the valence band. Figure 2.3 shows the shape of the carrier distribution versus energy as the product of the distribution function and the density of states function as well as how it varies with the carrier concentration and carrier temperature.

On the left-hand side, near the conduction band edge, the square root like density of state function is dominant at high carrier injection levels while the exponential distribution function dominates towards higher energies. If the carrier density is increased then the higher quasi-Fermi level will increase the peak value and shift it towards higher energies as shown in the second plot. Next the carrier density is kept at its high values and the carrier temperature is increased. The peak value decreases again and shifts slightly back towards lower energies. The carriers at lower energies near the band gap have been redistributed towards the high energy tail of the distribution. It is therefore expected that the carrier concentration N_e and carrier temperature T_e will have opposite effects on the optical gain at photon energies near the bandgap.

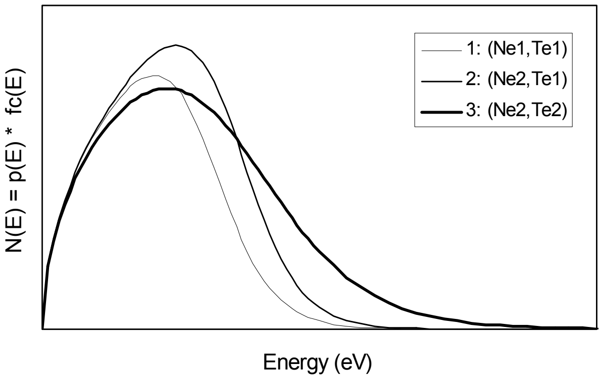

Figure 2.3: *Schematic plots for the product of the distribution function fc(E) and the density of states function ρ(E) at three different combinations of carrier concentration N_e and carrier temperature T_e ($N_{e2}>N_{e1}$, $T_{e2}>T_{e1}$)*

The calculated values for the optical absorption versus photon energy for different carrier concentrations and temperatures are given in figure 2.4. [16].

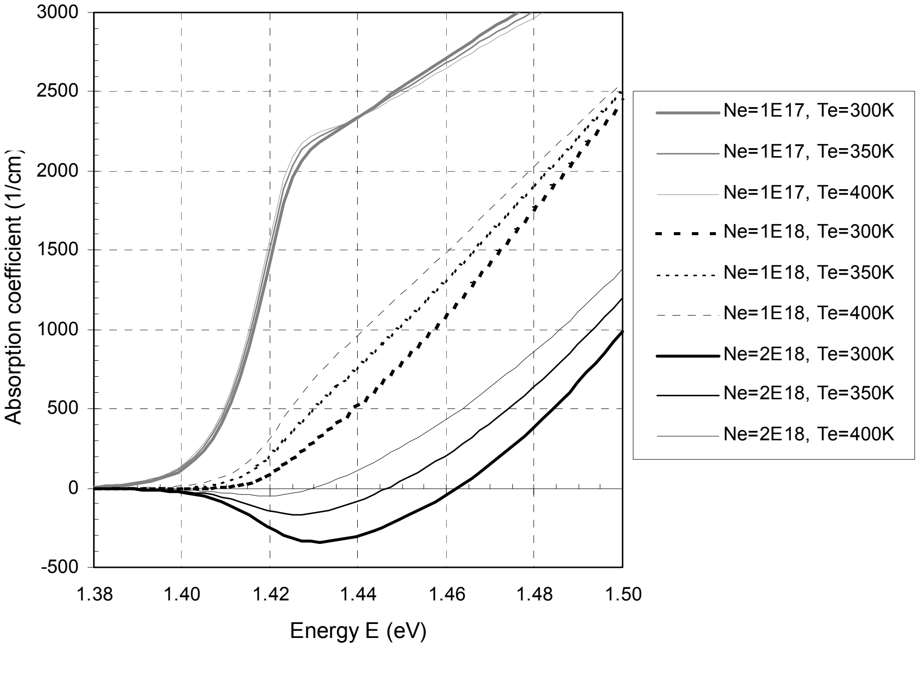

Figure 2.4: *Calculated absorption coefficient versus photon energy at different carrier concentrations and temperatures ($N_e=1x10^{17}cm^{-3}$ - $2x10^{18}cm^{-3}$, T_e=300K - 400K, after Tolstikhin [16])*

Here the carrier temperature is varied through both the electron and hole temperature: $T_e = T_h \neq T_l$. Within the hot electron injection laser we intend to vary only the electron temperature T_e. The actual photon energy is therefore expected to be slightly lower because the holes remain cold, $T_h=T_l$, and confined to the top of the valence band. The calculations go beyond one-electron effects and include the Banyai-Koch plasma screening effects [19]. The trends shown in figure 2.4 agree with the predictions of equation 2.16 and figure 2.3 in the sense that increasing the carrier density increases the gain as expected but also in the sense that increasing the carrier temperature decreases the gain again. The peak material gain for N_e=2x10^{18} cm^{-3} decreases from 340 cm^{-1} at T_e=300K to 170 cm^{-1} at T_e=350K or $\frac{\partial g}{\partial T_e} = -3.4\frac{1}{cmK}$. Both N_e and T_e also have a profound effect on the photon energy at which the peak gain value occurs as shown in figures 2.4 and 2.5.

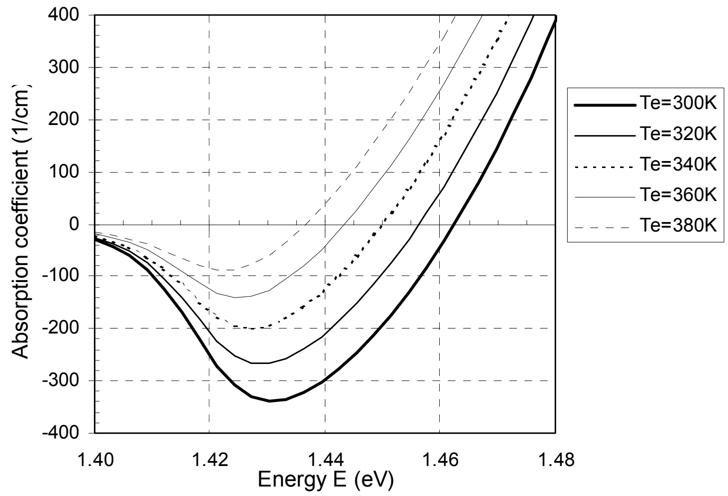

Figure 2.5: *Calculated absorption coefficient versus photon energy at different carrier temperatures (N_e=2x10^{18}cm^{-3}, T_e=300K - 380K, after Tolstikhin [16])*

This will result in the modulation of the longitudinal mode spectrum if the laser is directly modulated. And again, the effect is opposite: higher carrier densities shift the peak gain energy towards higher photon energies but higher carrier temperatures shift the peak gain energy back towards lower photon energies again. Figure 2.6 shows the full overview of the calculated material gain coefficient versus carrier concentration and carrier temperature at the fixed photon energy of 1.427eV. The gradient of $\partial g_p/\partial T_e$ is therefore slightly different as compared to the same gradient for the actual peak gain.

Actual values for the gradient $\partial g_p/\partial T_e$ decrease from -3.4 1/cmK at N_e=1.5x10^{18} cm^{-3} to -3.1 1/cmK at N_e=2.0x10^{18} cm^{-3}. Figure 2.6 predicts the required threshold carrier concentration and carrier temperature for lasing given the laser's internal losses, mirror losses and confinement factor.

2.5 Index modulation and frequency shift

The real and the imaginary parts of the susceptibility $\chi = \varepsilon/\varepsilon_0 - 1$, and thus of the complex dielectric constant ε, are coupled through the Kramers-Kronig relations [15][16]. Any variation in gain g or absorption α therefore induces a change in the refractive index n and vice versa. And since the gain depends on both the electron concentration N_e and the carrier temperature T_e, the refractive index will also depend on both carrier concentration and temperature

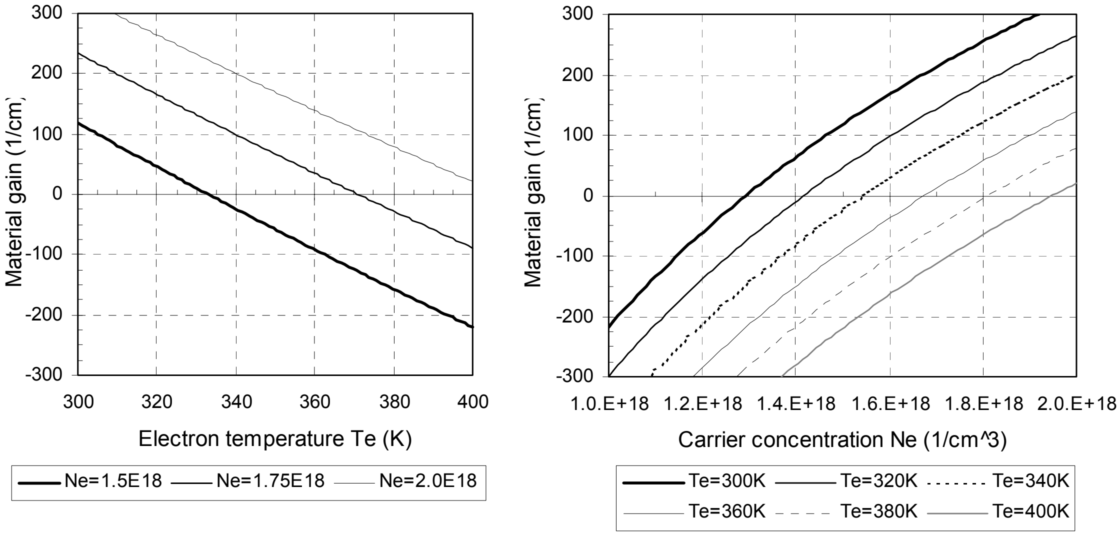

Figure 2.6: *Calculated material gain coefficient around population inversion versus carrier density at different carrier temperatures (left) and versus carrier temperature at different carrier densities (right) (at fixed photon energy E=1.427eV, after Tolstikhin [16])*

$n = n(N_e,T_e)$. The coupling between the carrier concentration induced changes in the real and the imaginary part of the susceptibility is given by the linewidth broadening factor α, which is traditionally defined as [15]:

$$\alpha = \frac{\partial\Re\{\chi(N_e,T_e)\}/\partial N_e}{\partial\Im\{\chi(N_e,T_e)\}/\partial N_e} \tag{2.18}$$

The numerator in this equation, i.e. the slope of the refractive index change due to variations in the carrier concentration, is negative around the gain peak due to the asymmetry in the gain function and the specific definition of the Kramers-Kronig relation. Practical absolute values for the α parameter for AlGaAs/GaAs lasers range between 2.5 and 6 for bulk active layers and between 1.5 and 2.0 for multiquantum well active layers [15]. The relative change in index is therefore larger than the relative change in gain. The actual longitudinal emission frequencies for Fabry-Perot type lasers are given by:

$$\upsilon = \frac{mc}{2Ln_{eff}} \tag{2.19}$$

with integer m, optical cavity length L and the effective refractive index n_{eff}. The actual emitted frequencies depend on the peak energy and the width of the material gain versus photon energy function. Combining equations 2.18, 2.19 and the rate equations, Petermann derived an expression for the optical emission frequency versus the injection current [22]:

$$\frac{\partial\upsilon}{\partial I} = \frac{\alpha}{8\pi}\left(\frac{hv}{q}\right)v_g\alpha_m\kappa \tag{2.20}$$

with I the injection current, α the linewidth broadening factor, $v_g = c/n_{eff}$, α_m the mirror losses and κ the gain compression factor due to the nonlinear optical gain. All diode lasers, even DFB lasers with single-mode emission, are therefore subject to significant broadening of their spectrum. In its current form, α only accounts for the carrier concentration induced changes and another form of the α-parameter has to be defined to correlate refractive index changes to the changes in the carrier-heating induced material gain [23][24]:

$$\alpha_T = \frac{\partial\Re\{\chi(N_e,T_e)\}/\partial T_e}{\partial\Im\{\chi(N_e,T_e)\}/\partial T_e} \tag{2.21}$$

The resulting change in the lasing wavelength due to the modulation of the carrier temperature is given by [23]:

$$\Delta\lambda = \frac{\lambda^2}{4\pi n_{eff}}(\alpha_T - \alpha)\frac{\partial g}{\partial T_e}\partial T_e \tag{2.22}$$

Here we see the opposite effect that α_T and α, and thus the carrier temperature and concentration, have on both the refractive index and the lasing wavelength: higher carrier concentrations decrease the material refractive index while higher carrier temperature increases the material refractive index. Relevant data regarding these steady-state parameters and effects, as published in literature, is given in table 2.2.

Table 2.2: *Overview of the values reported in literature for the carrier concentration and carrier heating induced index changes and both linewidth broadening factors*

Device and reference	$\partial n/\partial N_e$	$\partial n/\partial T_e$	α	α_T
CSP AlGaAs laser [24]	-1.7×10^{-4}	2.1×10^{-4}	5	2
InGaAsP/InP, MQW AL laser [23]			1.4	2.0-2.1
InGaAsP/InP, bulk AL laser [16]	-3×10^{-4}	$< 1\times10^{-4}$		

2.6 Frequency chirp and complementary modulation

The dynamic situation is different and applies when the electron concentration or temperature is modulated which triggers the electron-photon resonance. This feedback within the rate-equations results in substantial variations in both carrier and photon concentrations, the refractive index and ultimately in the lasing frequency. This dynamic variation of the lasing frequency is called frequency chirp. Chirp significantly influences the behavior of fiber telecommunication systems by limiting the bit rate, which can be transmitted across a minimum length l due to fiber dispersion. The time-bandwidth product $\Delta t\Delta\upsilon$, for example, for Gaussian shaped pulses with a FWHM pulse width equal to Δt and a spectral width $\Delta\upsilon$ is given by [22]:

$$\Delta t\Delta\upsilon = 0.44\sqrt{1+\alpha^2} \tag{2.23}$$

Pure energy injection based carrier temperature modulation can generate very short pulses with FWHM values of 3ps, only limited by the carrier energy relaxation time [26]. Such a scheme suffers from carrier burning, resulting in the requirement for additional time in between pulses to replenish the active layer with carriers, and carrier related chirp described in the previous section. The solution is to combine carrier and energy injection into a complementary modulation scheme, which injects additional carriers during the short optical pulse.

Gorfinkel took the complementary modulation to the next level by calculating the right shape and balance of the injection current and the energy injection such that the carrier-photon resonance is completely eliminated [25]. The suppression of the relaxation oscillations leads to a fast train of chirp-free optical pulses. Tolstikhin calculated the exact energy injection as to have a fully identical temporal shape of both the carrier concentration $N_e(t)$ and the carrier temperature $T_e(t)$ [26]. The difference in amplitude of both $N_e(t)$ and $T_e(t)$ should be chosen such that the difference between $\partial n/\partial N_e$ and $\partial n/\partial T_e$ is cancelled out (see table 2.2). Such a scheme will result in strongly reduced, or even zero, linewidth broadening factors. Tolstikhin described and calculated the required shapes for both carrier and energy injection signals and showed how a very fast train of 3ps FWHM pulses can be obtained without any carrier related frequency chirp [26].

References

[1] N, Balkan, *Hot Electrons in Semiconductors, Physics & Devices,* Oxford University Press, 1998.

[2] K, Hess, *Advanced theory of semiconductor devices*, Prentice-Hall, 1988.

[3] K, Hess, *Monte Carlo device simulation: full band and beyond*, Kluwer Academic Publishers, 1991.

[4] T.G. van de Roer, V.I. Tolstikhin, and R.C.P. Hoskens, “Monte Carlo simulation of electron transport in a hot-electron laser,” *Proc. URSI XXVI*, Toronto, Canada, 13-21 Aug 1999, p. 247.

[5] T.G. van de Roer, *Microwave electronic devices*, Chapman & Hall, 1994.

[6] J. Shah, *Hot carriers in semiconductor nanostructures*, Academic Press, 1992.

[7] C. Jacoboni and L. Reggianni, “The Monte Carlo method for the solution of charge transport in semiconductors with applications to covalent materials,” *Rev. Mod. Phys.*, vol. 55, pp. 645-705, 1983.

[8] K. Yokoyama and K. Hess, “Monte Carlo study of electronic transport in $Al_{1-x}Ga_xAs$/GaAs single-well heterostructures,” *Phys. Rev. B*, vol. 33, pp. 5595-5606, 1986.

[9] K. Yokoyama and K. Hess, “Calculation of warm electron transport in AlGaAs/GaAs single heterostructures using a Monte Carlo method,” *J. Appl. Phys.*, vol. 59, pp. 3798-3802, 1986.

[10] A. Dargys and J. Kundrotas, *Handbook on physical properties of Ge, Si, GaAs, and InP*, Science and Encyclopedia Publishers Vilnius, 1994.

[11] T. Kurosawa, “Monte Carlo calculation of hot-electron problems,” J. Phys. Soc. Jpn., vol. 21, pp. 424-426, 1966.

[12] G.P. Agrawal and N.K. Dutta, *Semiconductor lasers*, Kluwer Academic Publishers, 1993.

[13] H.C. Casey and M.B. Panish, *Heterostructure lasers, Part A: fundamental principles*. Academic Press, 1978.

[14] C.H. Henry, “Theory of the linewidth of semiconductor lasers,” *J. Quantum Electron.*, vol. 18, pp. 259-264, 1982.

[15] M. Osinski and J. Buus, “Linewidth broadening factor in semiconductor lasers-an overview,” *J. Quantum Electron.*, vol. 23, pp. 9-29, 1987.

[16] V.I. Tolstikhin and M. Willander, “Carrier heating effects in dynamic-single-frequency GaInAsP-InP laser diodes,” *J. Quantum Electron.*, vol. 31, pp. 814-833, 1995.

[17] D.J. Westland, J.F. Ryan, M.D. Scott, J.I. Davies, and J.R. Riffat, “Hot carrier energy loss rates in GaInAs/InP quantum wells,” *Sol. St. Electron.*, vol. 31, pp. 431-434, 1987.

[18] Y. Rosenwaks, M.C. Hanna, H. Levi, D.M. Szmyd, R.K. Ahrenkiel, and A.J. Nozik, “Hot-carrier cooling in GaAs: quantum wells versus bulk,” *Phys. Rev. B.*, vol. 48, pp. 675-678, 1993.

[19] L. Banyai and S.W. Koch, “A simple theory for the effects of plasma screening on the optical spectra of highly excited semiconductors,” *Z. Phys. B*, vol. 63, pp. 283-291, 1986.

[20] V.I. Tolstikhin and M. Mastrapasqua, “Three-terminal laser structure for high-speed modulation using dynamic carrier heating,” *Appl. Phys. Lett.*, vol. 67, pp. 3868-3870, 1995.

[21] V.I. Tolstikhin and M. Willander, “Competition between carrier concentration and temperature influences on gain as means for improving modulation repsonse of semiconductor lasers,” *J. Appl. Phys.*, vol. 77, pp. 488-493, 1995.

[22] K. Petermann, *Laser diode modulation and noise*, Kluwer Academic Publishers, 1988.

[23] G.E. Shtengel, R.F. Kazarinov, G.L. Belenky, and C.L. Reynold Jr, “Wavelength chirp and dependence of carrier temperature on current in MQW InGaAsP/InP lasers,” *J. Quantum Electron.*, vol. 33, pp. 1396-1402, 1997.

[24] C.T. Hultgren and E.P. Ippen, “Ultrafast refractive index dynamics in AlGaAs diode laser amplifiers,” *Appl. Phys. Lett.*, vol. 59, pp. 635–637, 1991.

[25] V.B. Gorfinkel and S. Luryi, “High-frequency modulation and suppression of chirp in semiconductor lasers,” *Appl. Phys. Lett.*, vol. 62, pp. 2923-2925, 1993.

[26] V.I. Tolstikhin and M. Willander, “Three terminal laser structures for high-speed modulation using variable carrier heating,” *Proc. SPIE*, vol. 2693, pp. 534-544, 1996.

Chapter 3

Device design

THE HOT ELECTRON INJECTION LASER DERIVES ITS PROPERTIES FROM THE VERTICAL INTEGRATION OF A DIODE LASER WITH A HETEROJUNCTION BIPOLAR TRANSISTOR. JOINING THE LAYER STACKS OF THESE DEVICES PUTS EXTRA EMPHASIS ON THE EPITAXIAL DESIGN TO ENSURE PROPER TRANSISTOR AND LASER BEHAVIOR AS WELL AS THE REQUIRED ELECTRON HEATING. THIS CHAPTER PRESENTS THE EPITAXIAL DESIGN RULES.

3.1 The purpose of vertically integrating a transistor and a laser

The purpose of integrating a bipolar transistor and a diode laser into a single structure is the ability to independently control the amount of carriers and the energy of the carriers flowing into the active region. This allows gain modulation through carrier heating and cooling under constant current or carrier flow. The schematic diagram of the vertically integrated transistor laser, as proposed by Tolstikhin and Mastrapasqua [1], is presented in figure 3.1.

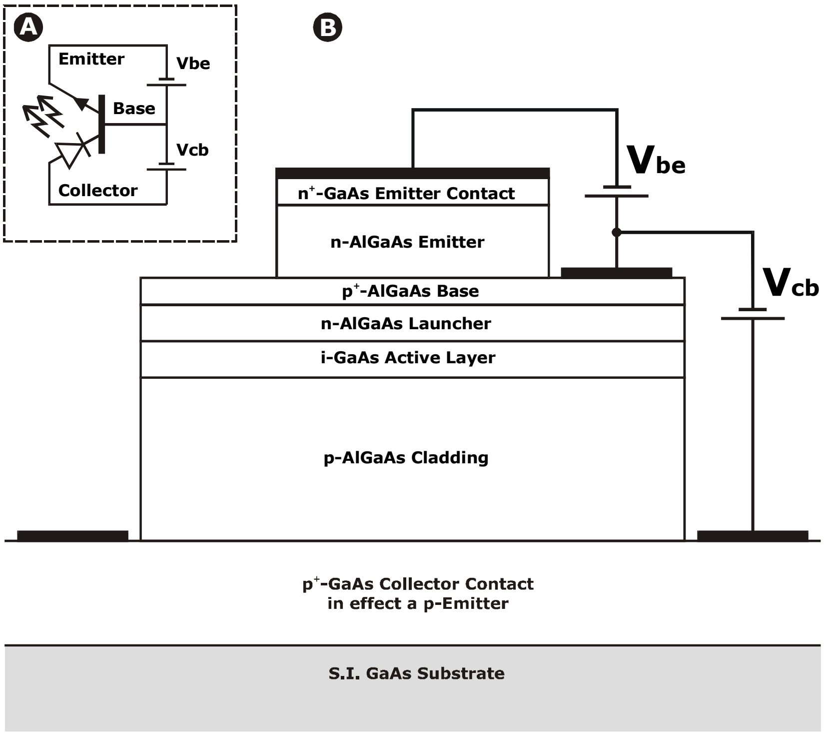

Figure 3.1: *(a) Electrical equivalent circuit and (b) schematic diagram for the vertically integrated transistor-laser*

The base-emitter junction of the transistor controls the current flowing through the device and hence the amount of carriers injected into the laser's active region. A lowly doped region inside the laser's cladding region, the so-called launcher, sustains a variable electric field depending on the voltage across the laser diode and is therefore capable of controlling the energy of the injected carriers. The present combination of a transistor and a laser will thus result in a complementary modulation scheme since the modal gain depends on both the concentration and the temperature of the carriers inside the active region. Two driving signals are now available as opposed to the single driving current in conventional lasers: the base-emitter voltage controls the current into the active region and the collector-base voltage across the low doped launcher controls the energy of the carriers flowing into the active region. The voltage across the launcher is used for ultra-fast modulation of the modal gain while the voltage across the emitter-base junction will compensate for other parasitic effects such as wavelength chirp.

3.2 Electro-optical device simulator

An electro-optical simulator is used to optimize the design for the hot electron injection laser. The simulator needs to be equipped with correct models for both carrier transport across abrupt PN-heterojunctions as well as correct optical models within such a complex epitaxial structure. The commercially available simulator Lastip, developed and sold by Crosslight Software Inc. fulfilled most of the requirements [2][3][4][5]. The only missing link is a hydrodynamic model to accurately describe effective carrier temperature and feeding this carrier temperature back into the optical model regarding material gain and losses and possibly even regarding the effective index to determine the chirp behavior. Hot carrier effects are therefore not included in these simulation results. The simulator assumes instantaneous redistribution of the carriers into a Fermi-Dirac distribution with a temperature T equal to the lattice temperature. The goal for the simulations performed with Lastip is therefore stable and constant optical behavior over a wide range of collector-base voltages. Any changes in the measured optical behavior versus the collector-base voltage are then more easily linked to possible carrier heating effects.

Lastip stands for LASer Technology Integrated Program. It is in effect a fully numerical program which solves the full set of coupled non-linear equations that govern the electro-optical behavior. The simulator tries to converge towards the solution in an iterative minimization routine using the Newton-Raphson method on a full 2D mesh in both lateral and transversal directions. The set of coupled non-linear equations includes:

A: the drift diffusion model describing the electrical behavior

- Poisson's equation which describes the electrostatic potential

$$-\nabla \cdot \left(\frac{\varepsilon_0 \varepsilon_{r_{lf}}}{q} \nabla V\right) = -n + p + N_d(1 - f_c) - N_a f_v + \sum_i N_{tj}(\delta_j - f_{tj}) \qquad 3.1$$

- the continuity equations for the electrons and holes

$$\nabla \cdot J_n - \sum_i R_n^{tj} - R_{sp} - R_{st} - R_{au} = \frac{\partial n}{\partial t} + N_d \frac{\partial f_c}{\partial t} \qquad 3.2$$

$$\nabla \cdot J_p + \sum_i R_p^{tj} + R_{sp} + R_{st} + R_{au} = -\frac{\partial p}{\partial t} + N_a \frac{\partial f_v}{\partial t} \qquad 3.3$$

where the electron and hole current densities J_n and J_p are written as functions of both the carrier densities n and p, electron and hole mobility μ_n and μ_p, and the quasi-Fermi levels E_{fn} and E_{fp}.

$$J_n = n\mu_n \nabla E_{fn} \qquad 3.4$$

$$J_p = p\mu_p \nabla E_{fp} \qquad 3.5$$

B: the optical model describing the optical mode profile and the photon density

- the complex scalar wave equation solving for the optical mode distribution

$$\nabla^2 \cdot \boldsymbol{E} + n^2 k_0^2 \boldsymbol{E} = 0 \qquad 3.6$$

with $k_0 = \omega / c = 2\pi / \lambda$ the vacuum wave number and $n = n(x, y, \lambda)$ the complex refractive index.

- the photon rate equation determining the photon density in the lasing mode

$$\frac{c}{n_g}(g - \alpha_{int} - \alpha_m)S + c_m \int R_{sp} dv = \frac{\partial S}{\partial t} \qquad 3.7$$

Coupling between the first three equations, describing the electrical behavior, and the last two equations, describing the optical behavior, is implemented through the stimulated emission rate R_{st}. Additional features included in the simulator are tunneling through abrupt heterojunctions, impact ionization, the effective index method as well as various features to include the effects of strained quantum wells. These strained quantum well features won't be used here since the design incorporates bulk active layers to obtain more direct carrier heating effects within the active layer. Unless stated otherwise, the following device dimensions are assumed:

- emitter ridge width W_e equal to 8µm,
- base and active layer ridge width W_b equal to 32µm,
- device cavity length L equal to 500µm, and
- only the right half of the device is simulated.

The other half, symmetric across the central axis through the middle of the emitter ridge, is included in the absolute results like light intensity and total currents flowing through the emitter, base and collector.

Additional programs are used to calculate the transverse optical mode distribution and the lateral step in effective index using the effective index method [9]. The effective index method simplifies equation 3.6 by first solving for the transverse optical field distribution $\phi(y, x)$ at different fixed lateral positions x [12]:

$$\frac{\partial^2 \phi}{\partial y^2} + [n^2 k_0^2 - \beta_{eff}^2(x)]\phi = 0 \qquad 3.8$$

with $\beta_{eff}^2(x)$ the effective propagation constant at those fixed lateral positions x. Subsequently, the lateral optical mode distribution $\psi(x)$ is obtained using:

$$\frac{\partial^2 \psi}{\partial x^2} + [\beta_{eff}^2(x) - \beta^2]\psi = 0 \qquad 3.9$$

The complex effective index of refraction is defined as:

$$\mu_{eff}(x) = \beta_{eff}(x)/k_0 \qquad 3.10$$

The complex index of refraction incorporates both the index of refraction n and the absorption coefficient α:

$$\mu = n + i\frac{\alpha}{2k_0} \qquad 3.11$$

3.3 Optimizing the transistor

Normally the current through and the voltage across the diode laser are directly coupled through the well known diode current-voltage equation. Here they are decoupled by inserting the active region of the diode laser into the collector of the heterojunction bipolar transistor. The transistor's sole purpose is to provide a set current into the active region regardless of the voltage across the launcher. The current into the active region is now controlled by the voltage across the transistor's emitter-base junction instead of the voltage across the laser region itself. The general flow of electrons and holes is given below in figure 3.2.

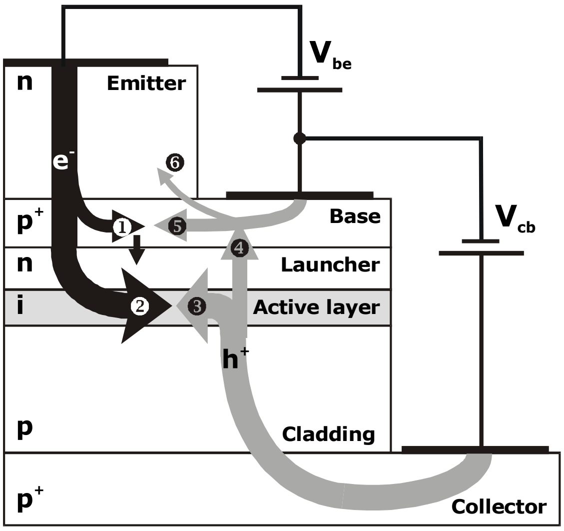

Figure 3.2: *Overview of the electron and hole currents flowing through the hot electron injection laser under normal forward biasing*

The transistor-laser is operated in a common-base configuration as shown in figure 3.1 under normal biasing. This means the emitter-base junction will be forward biased and the collector-base junction reverse biased. The first design criterion for the transistor is a maximum current transfer from the emitter into the collector region (comprised of the launcher, active layer, cladding and collector contact layers as shown in figure 3.1) and thus a common-base current gain α_0 close to unity [6]:

$$\alpha_0 = \frac{\partial I_C}{\partial I_E} = \frac{\partial I_{nE}}{\partial I_E}\frac{\partial I_{nC}}{\partial I_{nE}}\frac{\partial I_C}{\partial I_{nC}} \qquad 3.12$$

Here I_{nE} is defined as the electron component of the emitter current injected into the base and the first ratio is defined as the emitter injection efficiency $\gamma = \partial I_{nE}/\partial I_E$. Similarly, I_{nC} is defined as the electron component of the collector current. The second ratio is defined as the base transport factor $\alpha_T = \partial I_{nC}/\partial I_{nE}$ and describes the number of electrons reaching the collector over the total number of electrons injected from the emitter into the base. I_{nC} is defined as the electron component of the collector current (electron current 2 in figure 3.2) and the third ratio is defined as the multiplication factor M. In short, the common base current gain becomes:

$$\alpha_0 = \gamma\alpha_T M \qquad 3.13$$

3.3.1 High emitter injection efficiency

The first parameter to be optimized is the emitter injection efficiency γ and involves the emitter-base junction design. The emitter injection efficiency is limited by the fact that holes can flow from the base into the emitter region (hole current 6 in figure 3.2). An emitter injection efficiency close to unity for our npn transistor means that a relatively large amount of electrons are being injected into and across the base (electron currents 1 and 2 in figure 3.2) as opposed to holes going from the base into the emitter. The basic current-voltage relationships, considering the ideal diode equation for the junction, yield [6]:

$$\gamma = \left[1 + \frac{p_E D_E L_B}{n_B D_B L_E}\tanh\left(\frac{W_B}{L_B}\right)\right]^{-1} \sim \left[1 + \frac{N_b D_E W_B}{N_e D_B L_E}\right]^{-1} \qquad 3.14$$

where p_E and n_B are the minority carrier concentrations, D_E and D_B the minority-carrier diffusion coefficients inside the respective regions, L_E and L_B the minority carrier diffusion lengths, and W_B the thickness of the base. Equation 3.14 indicates that for traditional bipolar transistors, where the emitter and base are composed of the same material, controlling the relative amount of the carriers travelling in both directions across the junction means increasing the emitter doping and decreasing the base doping. Reducing the doping level inside the base will result in a high base resistance, especially in thin base layers like ours. This extra voltage drop across the base would also limit our control over the electric field inside the launcher. An extra mechanism is thus required to control the relative amount of carriers flowing in both directions across the junction.

The flow of carriers across the junction also depends exponentially on the barriers inside the conduction and valence band. These barriers are of equal height in homojunction transistors. In heterojunction bipolar devices however, these barriers can be designed to be unequal in height and hence control the flow of carriers, thus relaxing the stringent doping restrictions [8]:

$$\frac{I_{nE}}{I_{pE}} \propto \frac{N_e}{N_b} e^{\frac{\Delta E_g}{kT}} \qquad 3.15$$

The first term N_E/N_B is the stringent doping condition as seen for homojunction devices. The second term is the additional term for heterojunction devices, which depends exponentially on the difference in bandgap between the base and the emitter. A wide bandgap n-type emitter and a narrower bandgap p-type base will result in a larger valence band barrier qV_p for the holes and a decrease in the amount of holes flowing from the base into the emitter, as shown in figure 3.3.

By increasing the second term we can decrease the first term by increasing the base doping. This will decrease the base resistance, increase our control over the electric field inside the launcher and decrease the chances of base punch-through. For example, an $Al_{0.3}Ga_{0.7}As$ (E_g=1.798eV) emitter and a $Al_{0.1}Ga_{0.9}As$ (E_g=1.549eV) base already decrease the ratio of equation 3.15 by 1.6×10^{-5}. Realistic differences in doping levels between the base and the emitter only decrease this ratio by 1×10^{-1}-1×10^{-2}. This means we can increase the base doping again to levels suitable for ohmic contacts on p-type AlGaAs material (>4×10^{18} cm^{-3}). The wide bandgap emitter also serves as part of the n-type cladding to confine the mode inside the active region because the narrower bandgap base works against confining the optical mode. The base layer design will be taken into account when designing the transverse optical mode in section 3.5.3.

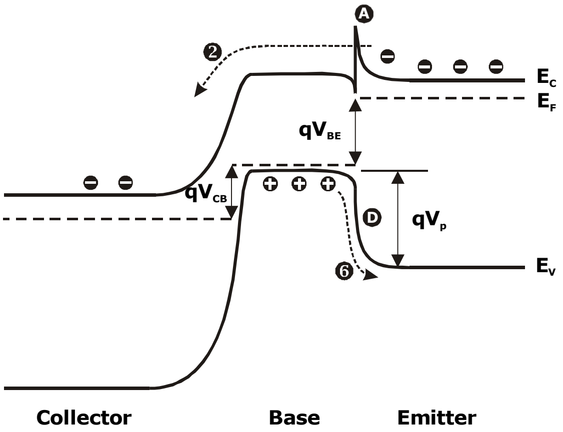

Figure 3.3: *Band diagram of an NPN heterojunction bipolar transistor under normal forward bias*

3.3.2 Electron transport across the base

The second term of equation 3.12 involves the base transport factor α_T and describes the transport of the electrons across the base and into the collector. Some electrons will recombine with holes inside the base after being injected into the base as denoted by electron current 1 in figure 3.2. Most of the electrons will traverse the base and the base-collector junction (electron current 2 in figure 3.2) and continue through the launcher of the collector region. The base transport factor itself can be given as [6]:

$$\alpha_T = \frac{1}{\cosh\left(\frac{W}{L_B}\right)} \approx 1 - \frac{W_{Beff}^2}{2L_B^2} \qquad 3.16$$

where W_{Beff} denotes the effective base thickness. Equation 3.16 indicates that in order to maximize the electron injection current into the collector region, the thickness of the base should be thin and the electron diffusion length inside the base should be long.

$$L_B = \sqrt{D_B \tau_B} \qquad 3.17$$

Another important effect that influences the electron transport across the base is the base-width modulation effect of bipolar transistors under normal forward bias. Both the base-emitter voltage V_{be} and the collector-base voltage V_{cb} modulate the effective base width through the varying thickness of their respective space-charge regions. The collector-base space-charge region is most important to us due to the modulation of this voltage, which is used to vary the optical output of the device. The width of the base and collector side depletion regions are approximated by ($N_A \gg N_D$):

$$\Delta W_{BCn} = \frac{W_B N_a}{N_a + N_d} = \left(\frac{2\varepsilon V_{cb}}{q}\frac{1}{N_d}\right)^{1/2} \qquad 3.18$$

$$\Delta W_{BCp} = \frac{W_B N_d}{N_a + N_d} = \left(\frac{2\varepsilon V_{cb}}{q}\frac{N_d}{N_a^2}\right)^{1/2} \qquad 3.19$$

where V_{bc} denotes the reverse bias on the base-collector PN-junction. This base-narrowing effect $W_{Beff} = W_B - \Delta W_{BCp}$ is called the Early effect, the result of which is a decrease in the effect base width W_{Beff} and an increase in both the base transport factor α_T and the common-emitter current gain α_0. As a result, the collector current increases with V_{ce} (common-emitter) or V_{cb} (common-base) and the slope of this increase leads to the Early voltage, which has a high temperature dependence [13]:

$$V_A = I_c\frac{\partial V_{ce}}{\partial I_c} - V_{ce} \approx I_c\frac{\partial V_{cb}}{\partial I_c} \qquad 3.20$$

Increasing the reverse bias V_{cb} pushes the space charge region further into the collector but at the same time slightly further into the base. A strong reverse bias, a thin base, a slightly lower doping ratio N_a/N_d or a combination of these can all push the space region across the full thickness of the base W_B and cause the onset of the effect known as base punch-through. Electrons are swept straight from the emitter into the collector and all transistor action disappears. The best solution to minimize the base width modulation effect and to prevent base punch-through is to maintain a high base to collector doping ratio N_a/N_d. This ratio has its practical limits and additional restrictions are put on it due to free carrier absorption inside the base and specific design rules for the launcher, as explained in section 3.5.

The shape of the base-emitter junction conduction band profile also influences the electron transport across the base. The conduction band spike, indicated as *A* in figure 3.3, is due to the abrupt base-emitter heterojunction. It results in the requirement for thermionic emission and tunneling for the electrons to be transported into the base. These carriers enter the base with a small excess energy and a momentum that is directed mainly perpendicular to the plane of the base layer. This helps them traverse the base. Both energy and momentum are then redistributed through elastic impurity scattering and inelastic collisions [13]. The initial energy and directional momentum increase the probability of transmission of these electrons across the base-collector conduction band barrier at the end of the base. Quasi ballistic transport helps to increase the base transport factor α_T and the increase is determined by the initial excess energy and the base thickness. Fully ballistic transport in, for example, unipolar hot electron transistors is limited to a base thinner than 10nm. Both the base transport factor and the unscattered electron fraction drop rapidly with the base thickness until almost all electrons will have scattered at least once at a base thickness equal to 100nm [14].

The electron transport across the base also influences the high frequency behavior. The intrinsic cutoff frequency of the transistor is mainly determined by the transit time from the emitter to the collector and given by [13]:

$$f_T = \frac{1}{2\pi\tau_{ec}} = \frac{1}{2\pi\left[\frac{kT}{qI_c}(C_{je} + C_{jc}) + \tau_b + \tau_c + R_c C_{jc}\right]} \qquad 3.21$$

where C_{je} and C_{jc} are the junction capacitances as the sum of the depletion capacitance and the free carrier capacitance, R_c the collector resistance and τ_{ec}, τ_b and τ_c the emitter to collector, base and collector transit times respectively. The cutoff frequency reaches its peak value at moderate current densities and the peak value depends mainly on the base and collector transit times τ_b and τ_c [6]. The base transit time within a uniform base is predominantly determined by the width of the base and the diffusion coefficient:

$$\tau_b = \frac{W_B^2}{2D_n} \tag{3.22}$$

Equation 3.22 again pleads for a thinner base and to a lesser extent for a high minority carrier diffusion constant inside the base. The maximum frequency of oscillation of the intrinsic device is approximated by the well-known equation [15]:

$$f_{max} \approx \sqrt{\frac{f_T}{8\pi R_b C_{jc}}} \tag{3.23}$$

Here we see the importance of a small base resistance and collector capacitance. Care has to be taken to minimize these values when designing the epitaxial layer stack and the mask set. Delta doping and wider base contact pads, for example, can be used to reduce the base series resistance.

3.3.3 Breakdown of the collector

Breakdown mechanisms within the collector and in our case the launcher can be divided into breakdown through avalanche multiplication and Zener breakdown. Both have to be taken into account since the electric field inside the launcher reaches values of at least $1\text{x}10^5$ V/cm and also because the doping levels within the n-type launcher are in the range of $5\text{x}10^{16}$-$2\text{x}10^{18}$ cm^{-3}. Avalanche breakdown is electric field driven that causes the electrons to gain kinetic energy. Upon reaching a certain level, the kinetic energy is sufficient to transfer another electron from the valence band to the conduction band through an elastic collision. This effect, called avalanche multiplication or impact-ionization, is usually initiated from the higher Γ or L subbands where the electrons have sufficient kinetic energy to generate the extra electron-hole pair. Impact-ionization can also occur at abrupt band barriers, in case of a discontinuity larger than the bandgap, for example in small bandgap materials. The excess energy obtained through thermionic emission or tunneling can be sufficient for impact ionization to occur. This effect is known as Auger generation [13]. The amount of impact ionization is expressed through the parameter α_n called the impact-ionization coefficient, which indicates the relative increase in electron density per unit length these carriers travel. According to Kyuregyan and Yurkov α_n for GaAs can be approximated by [16]:

$$\alpha_n = \alpha_0 \exp\left(\delta - \sqrt{\delta^2 + \left(\frac{F_0}{F}\right)^2}\right) \tag{3.24}$$

where α_0=$2.45\text{x}10^6\text{cm}^{-1}$, δ=57.6, and F_0=$6.65\text{x}10^6$V/cm. Within the expected range of electric fields of $5\text{x}10^4$ to $2.5\text{x}10^5$ V/cm or 0.5 to 2.5 volt per 100µm, equation 3.24 predicts α_n to remain below 800 cm^{-1}. The relative increase in carrier concentration therefore remains below $8\text{x}10^{-3}$ or 0.8% per 100µm. These values increase rapidly above the mentioned electric field strengths and limit the design window since such relative increases in active layer carrier concentration do influence the optical performance. Such collector-base voltage dependent impact-ionization can counteract the effect that carrier heating has on the optical gain but should be visible as a positive slope in the $I_c(V_{cb})$ curve under normal forward bias. It should be noted here that an individual electron needs to traverse a potential difference of at least the bandgap in the launcher, which is equal to 1.8eV. For an ensemble of electrons, most of which are scattered at least once, an even greater potential difference is needed. So if the total potential drop in the launcher is kept below 2V, significant impact ionization is not possible regardless of the local field strength.

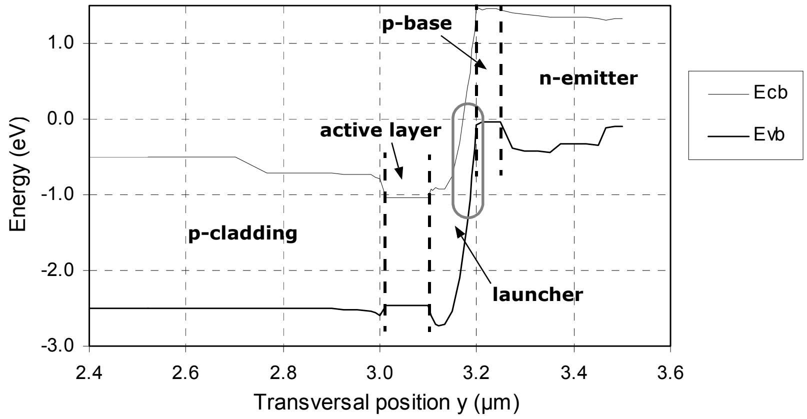

Figure 3.4: *Simulated energy band diagram of the hot electron injection laser under normal forward bias indicating the conduction and valence bands adjacent to each other inside the first part of the collector or launcher due to increased doping levels at that location and higher collector-base voltages* ($W_e=3\mu m$, $W_b=7\mu m$, $I_e=50mA$, $V_{cb}=2.5V$, *active layer: 3.0µm-3.1µm, launcher: 3.1µm-3.2µm, base: 3.2µm-3.25µm, emitter: 3.25µm-3.5µm)*

Zener breakdown occurs when extreme band tilting of both the conduction and valence band brings the bands within tunneling distance of each other. That situation depends on both the doping level and the applied reverse voltage. This situation can occur, for example, when applying a strong reverse voltage across the base-collector P^+N-junction and in case of relative strong donor levels within the first part of the collector, or launcher in our case. Figure 3.4 shows the conduction and valence bands adjacent to each other within the first part of the collector or launcher but still outside tunneling distance. Increasing both the reverse voltage and the doping level in this section will bring them within tunneling distance from each other and Zener breakdown will happen. Tunneling breakdown is a relatively abrupt phenomenon resulting in a sudden very strong increase in collector current I_c. For n-type GaAs, the tunneling based Zener breakdown will dominate over impact ionization above doping levels of $N_d=4x10^{17}cm^{-3}$ due to the strong bending of the conduction and valence band. The resulting breakdown voltages will be smaller than 7V [6].

The best solution to the posed dilemma, a high electric field and strong carrier heating versus the risk of breakdown, is to spread the electric field evenly across the full thickness of the launcher. Figure 3.5 indicates the ideal triangular shape for the conduction band profile within the launcher. This particular profile results in a constant electric field and thus maximizes the carrier heating efficiency as discussed in section 3.5. At the same time it minimizes the risk of breakdown. Electrical measurements of the collector-base junction for the design presented in section 3.5.1 indicate the reverse breakdown voltage to be within the expected range at 6V to 8V or $6x10^5$ to $8x10^5$ V/cm for an effective launcher thickness of 100nm.

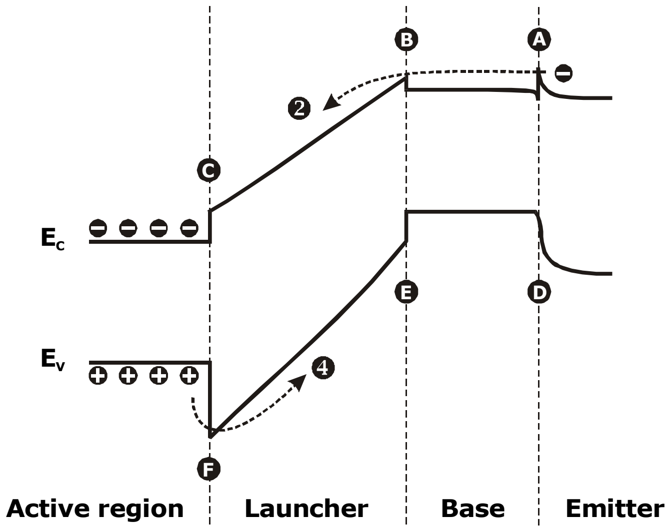

Figure 3.5: *Ideal triangular shape of the launcher's energy band profile*

3.3.4 The internal base potential

Ohmic contacts with low series resistances are required, not only to minimize the voltage drop across these resistances and thus the laser's joule heating, but also to maintain independent control over both the injection current and the electric field across the launcher. Any variations in the base or collector currents will after all be reflected in the electric field across the launcher due to voltage drops across the base and collector sheet and contact resistances. Operating the laser in collector current controlled and collector-base voltage controlled mode reduces the sensitivity of the laser to the collector resistance. However, unwanted modulation of the launcher's electric field due to the base resistance remains.

Another side effect from a relatively high base sheet resistance and a non-zero base current is an inhomogeneous lateral voltage drop across the width of the base layer W_b. Not only will the internal base potential be substantially different from the external base potential, but it will also have a strong lateral variation [7]. This means the injected current density and with it the optical gain as well as the launcher's electric field and thus the carrier heating efficiency will show similar lateral variations. Whether or not the effective electron temperature inside the active layer will show similar lateral variations depends on the level of very fast carrier-carrier interactions of the highly mobile electrons which are expected to level out these lateral variations to a certain extent depending on the lateral width of the active layer.

The most stable operating mode of this laser is therefore both collector current and collector-base voltage controlled and at minimum base current. Controlling the collector current is performed indirectly through a feedback loop to the emitter current. Minimum base current is usually reached for collector-base currents V_{cb} greater than 0.5V. The first 0.5V is required to reduce the conduction band barrier from the base into the launcher (barrier B in figure 3.5) and to use the launcher's electric field to stop electrons from diffusing from the active layer back into the base.

3.4 Optimizing the diode laser

Standard Fabry-Perot (FP) diode lasers consist of a lasing cavity supporting optical modes which traverse the cavity between two semi-transparent facets. During lasing the net round-trip gain of the optical mode is zero, meaning the gain due to stimulated emission is equal to the total losses it encounters. The stimulated recombination originates inside the active region. In order to simplify the design as much as possible and to obtain more direct carrier heating effects, both a bulk active layer, as opposed to quantum wells, and a cleaved-facet Fabry-Perot cavity will be used. This section gives an overview of the relevant physics behind such diode lasers. It also indicates how the design can influence the threshold current density and the external quantum efficiency to obtain efficient and stable lasing.

3.4.1 Optical performance

At threshold, when the stimulated emission equals the spontaneous emission, the net gain is zero:

$$\Gamma g - \alpha_i - \alpha_m = 0 \qquad 3.25$$

with g the material gain inside the active layer, Γ the relative confinement of the optical mode within the active layer, α_i the internal losses and α_m the mirror losses. The mirror losses account for the radiation exiting through the semi-transparent facets at both ends of the cavity:

$$\alpha_m = \frac{1}{2L}\ln\left(\frac{1}{R_1 R_2}\right) \qquad 3.26$$

where R_1 and R_2 indicate the front and rear facet reflectivity and L the cavity length. For the interface GaAs-air, R_1=R_2=0.32 and the mirror losses are equal to:

$$\alpha_m = \frac{1}{L}\ln\left(\frac{1}{R}\right) = \frac{1.14}{L} \qquad 3.27$$

Below threshold the device behaves like any light emitting diode (LED) emitting mainly spontaneous emission. Additional carriers are needed within the active layer to overcome the net losses. When the current is increased, upon reaching threshold, the stimulated emission overcomes both the losses and the spontaneous emission. The external or differential quantum efficiency (EQE) is defined as [12]:

$$\eta_e = \eta_i \frac{\text{photon escape rate}}{\text{photon generation rate}} = \eta_i \frac{v_g \alpha_m}{1/\tau_p} = \eta_i \frac{\alpha_m}{\alpha_m + \alpha_i} \qquad 3.28$$

with η_i the internal quantum efficiency defined as the fraction of electrons that is converted into photons, $v_g = c/\mu_g$ the group velocity and $\tau_p^{-1} = v_g(\alpha_m + \alpha_i)$ the photon lifetime within the cavity. η_e will be high for short lasers with low internal losses and relatively low for long lasers with high internal losses. The internal quantum efficiency is expressed as [12]:

$$\eta_i = \frac{Bn^2 + R_{st}S}{A_{nr}n + Bn^2 + Cn^3 + R_{st}S} \qquad 3.29$$

in which the linear term $A_{nr}n$ is due to non-radiative recombination, the quadratic term Bn^2 is due to spontaneous radiative recombination, the cubic term Cn^3 is due to multiple particle Auger recombination, S the photon density and $R_{st} = v_g g$ the rate of stimulated emission. The optical power emitted by each facet is given by [12]:

$$P_{out} = \frac{h\nu}{2q}\eta_i\frac{\alpha_m}{\alpha_m + \alpha_i}(I - I_{th}) \qquad 3.30$$

with P_{out} the optical power emitted by each facet, I the injection current and I_{th} the threshold current, which also includes any leakage currents flowing outside the active layer. Equation 3.30 tells us that the external quantum efficiency is related to the slope of the emitted optical power versus injection curve (L-I curve) as follows:

$$\eta_e = \frac{2q}{h\nu}\frac{\partial P_{out}}{\partial I}\bigg|_{I > I_{th}} \qquad 3.31$$

The external quantum efficiency η_e shows a strong abrupt increase at threshold indicating the higher efficiency of stimulated emission as compared to spontaneous emission. Any variations in η_e beyond threshold indicate changes in the internal losses α_{int} or the internal quantum efficiency η_i and thus the ratio of radiative recombination over the total recombination.

3.4.2 Threshold current density

Part of the goal of this design is to minimize the threshold current density J_{th}:

$$J_{th} = \frac{qdn_{th}}{\tau_e(n_{th})} \qquad 3.32$$

where d is the thickness of the active layer and τ_e the carrier recombination time. Using a linear gain versus carrier density approximation:

$$g(n) = a(n - n_0) \qquad 3.33$$

with a the gain coefficient and n_0 the carrier concentration to achieve population inversion (i.e. the transition between gain and absorption), the threshold carrier concentration can be expressed as [12]:

$$n_{th} = n_0 + \frac{(\alpha_m + \alpha_i)}{a\Gamma} \qquad 3.34$$

with Γ the confinement of the optical mode inside the active layer. Equations 3.26, 3.32 and 3.34 tell us that the threshold current density can be decreased by increasing L, R and Γ, and by decreasing d and α_i. A range of cavity lengths L can be included when designing the mask set as discussed in section 3.7. Increasing R means putting high-reflective coatings on the mirror facets. These coatings are wavelength specific and outside the scope of this thesis. Γ can be varied by changing the $Al_xGa_{1-x}As$ composition of the pre-cladding and the launcher. α_i is minimized by careful design of the transversal and lateral optical mode profile. The confinement inside the highly p-doped base is reduced for example to decrease free carrier absorption. The thickness of the bulk active layer is also reduced untill an optimum value of

100nm. Reducing the thickness even further causes an increase in the threshold current density again due to a reduced confinement of the transverse optical mode within the active layer [12].

3.4.3 Mismatch between the optical profile and gain profile

The confinement factor Γ denotes the overlap between the optical mode profile and the gain profile in both transverse and lateral directions. In case of a strong mismatch, radiative recombination outside the optical mode strongly increases the threshold current density. In equation 3.32, the carrier recombination time $\tau_e(n)$ is defined as:

$$\tau_e(n) = (A_{nr}n + Bn^2 + Cn^3)^{-1} \tag{3.35}$$

Such an increase in radiative and non-radiative recombination results in a higher threshold current density. Such an effect can occur in the hot electron injection laser due to a very obvious difference with conventional FP diode lasers. These lasers inject the holes from the top through the narrow top ridge. That significantly narrows the lateral gain profile since the hole mobility is many times lower than the electron mobility. The current design of the hot electron injection laser injects the holes from underneath the active layer and the electron from the top through the narrow emitter ridge. The electrons diffuse very easily in the plane of the active layer. The lateral hole distribution in the active layer depends very much upon the specific location of the p-type collector contacts, as shown in the simulated intensity plots of figure 3.6.

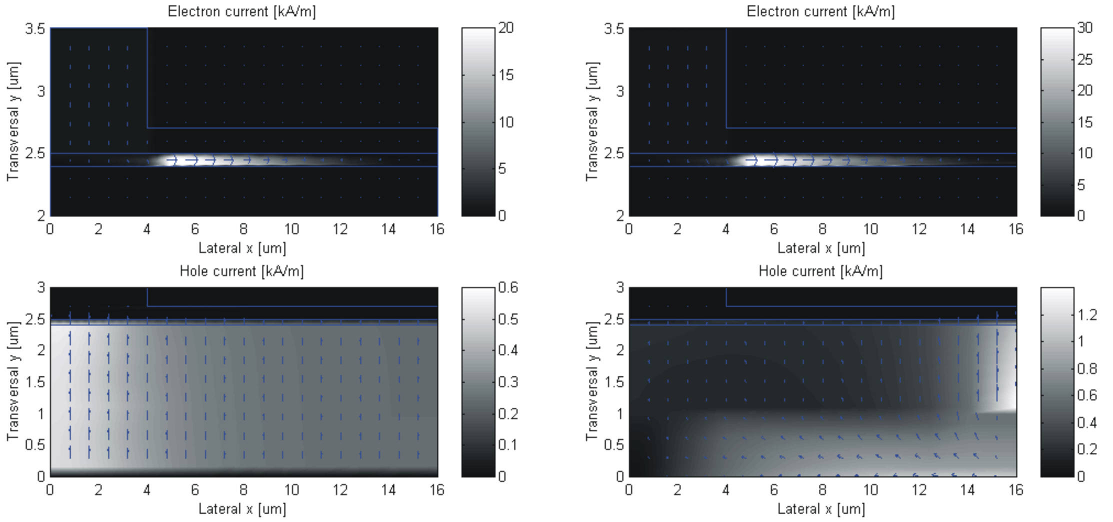

Figure 3.6: *Overview of the simulated electron and hole current paths in the case of a bottom (left) or side (right) collector contact metal (normal forward biasing, I_e=50mA, V_{cb}=2.5V)*

It shows the absolute value of both the electron current (top) and hole current (bottom) for two very different orientations of the collector contact. On the left, the collector contact is located at the bottom of the device between (x,y) = (-16,0) to (16,0). On the right, the collector contact is located at the right edge of the collector layer between (x,y) = (16,0) to (16,1). In both cases the emitter contact is between x = -4µm and x = 4µm. In case of a bottom contact the holes are redistributed evenly with a clear concentration underneath the emitter ridge. The side contact results in a completely different picture in which most of the holes travel directly along the edge of the p-cladding into the active layer due to their low mobility. There they are met with many electrons, which easily traversed the full width of the base resulting in substantial recombination losses. The corresponding gain curves are shown in figure 3.7.

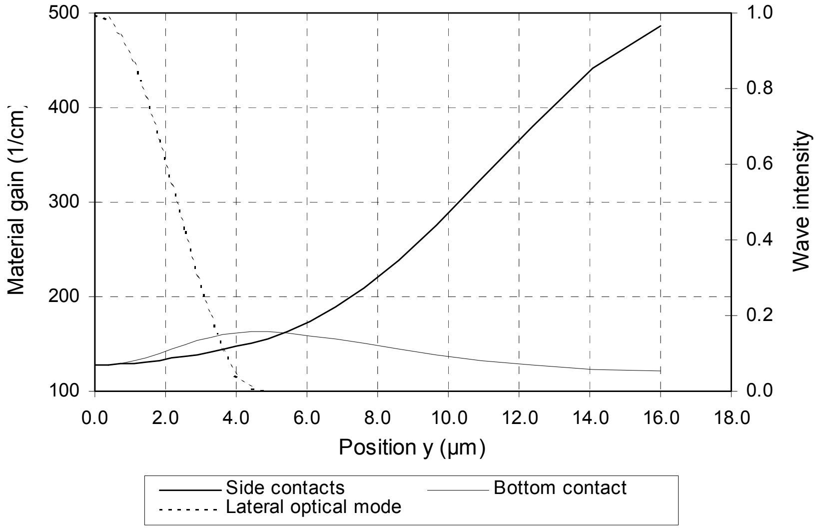

Figure 3.7: *Simulated lateral optical gain profile within the active layer versus the positioning of the collector contact (I_e=50mA, V_{cb}=1.0V)*

Contacting the collector from the bottom is clearly optimal from an optical performance point of view but also degrades the high frequency behavior due to the large substrate capacitance. To improve the high frequency behavior while maintaining proper optical performance requires a highly conductive layer to be included in the collector or p-type cladding layer outside the reach of the transverse optical mode. Epitaxy will be performed on both semi-insulating (S.I.) GaAs and p^+-GaAs substrates to obtain a wide range of results. The S.I. GaAs substrate requires collector contacts on both sides of the base-active layer ridge and will therefore experience the effect as shown in figure 3.7 to a certain degree. To decrease the threshold current density various ratios of W_e/W_b will be included on the mask set as discussed in section 3.7.

3.5 Combining the transistor & the laser

The transistor and the laser have to be combined into a single epitaxial layer stack with the laser's non-intentionally doped (NID) active region located directly underneath the transistor's highly doped p^+-base with a newly defined n-type launcher layer in between. This vertical integration puts additional strain on the existing design rules of the separate devices and a trade-off has to be made. The new design rules are divided into the following two categories: electrical and optical behavior. Optimizing the electrical behavior includes modifying the launcher to obtain a trade-off between leakage currents and carrier heating efficiency, in addition to optimizing the transistor behavior. Optimizing the optical behavior includes modifying the waveguiding to reduce optical absorption inside the base, as well as optimizing the design to increase the external quantum efficiency (EQE).

3.5.1 Band engineering of the launcher

The launcher merges the transistor and the laser together and facilitates the independent control over both carrier and energy injection into the active layer. It serves too many conflicting purposes however to apply uniform composition and doping across this layer. It needs to be n-type to retain the holes inside the active layer with a sufficiently high barrier in the valence band to block them from leaking through the launcher and into the base (hole current 4 and valence band barrier F in figures 3.2 and 3.5). On the other hand, it needs to be lowly doped, or even non-intentionally doped (n.i.d.) to sustain the electric field and spread it evenly throughout the full thickness of the launcher. Launcher compositions with lower indices of refraction will improve the confinement of the transverse optical mode inside the active layer. But the valence band barrier from the base into the launcher needs to be reduced in order to decrease the probability of electrons reflecting from the base-launcher interface and recombining within the base to form an additional loss current. This would require compositions closer to GaAs with higher indices of refraction.

This short discussion of the various effects and correlations directly clarifies the need for a tailor-made launcher in which various material compositions and doping levels are used to engineer the correct conduction and valence band profiles. The launcher is divided into the following three regions, each with its own specific goal:

- the *pre-launcher* with a bandgap close to that of the base lowers the conduction band barrier from the base into the launcher in order to increase the base transport factor α_T,
- the *main launcher* having a higher AlAs fraction for better confinement of the transverse optical mode distributes the electric field evenly across this main part of the launcher, and
- the *post-launcher* having a specific doping profile creates a valence band barrier to stop the holes from leaking through the launcher and into the base.

The main purpose of the launcher is still to provide an electric field which accelerates the passing electrons and increases their momentum and wave vector ***k***. The heating voltage V_{cb} applied between the collector and the base falls mainly across the launcher. The difference being the lateral voltage drop within the base layer, the transverse voltage drop across the base space charge region and the voltage required to align the valence bands within the collector, cladding and pre-cladding to get the holes inside the active layers. Using the space charge approximation, which ignores the presence of carriers within the transition region, the net charge on the n-type launcher side is equal to the uncompensated donor ions:

$$Q = qN_d \qquad 3.36$$

According to Gauss's law the electric field gradient is equal to the local space charge:

$$\frac{\partial E}{\partial x} = \frac{q}{\varepsilon}N_d \qquad 3.37$$

Equation 3.37 tells us that the electric field strength decreases linearly from the base-collector interface towards zero across the width of the transition region ΔW_{BCn}, as defined by equation 3.18. The maximum electric field strength at the interface is equal to:

$$E_0 = \frac{q}{\varepsilon}N_d\Delta W_{BCn} \qquad 3.38$$

The electric field can be distributed more evenly throughout the launcher by decreasing the concentration of donor ions inside the pre-launcher and slowly increasing the concentration of donor ions further into the launcher. Decreased doping levels within the pre-launcher near the launcher-base interface also helps to push the majority of the transition region into the launcher and to decrease the effect of base width modulation and the risk of base punch-through [6]. Figure 3.8 shows the unwanted onset of base punch-through at a collector-base voltage of only 1.0V due to the strong penetration of the space charge region into the p-type base for that particular and quite exceptional ratio of doping levels.

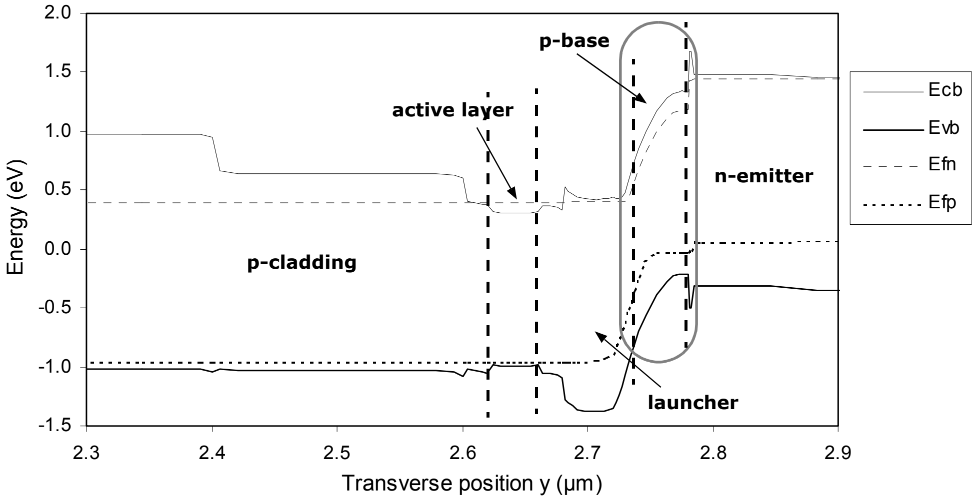

Figure 3.8: Simulated energy band diagram for the hot electron injection laser under normal forward bias indicating the unwanted situation in which the launcher's electric field penetrates into the base layer and the onset of base punch-through (I_e=30mA, V_{cb}=1.0V, base: N_a=6x10^{17}cm^{-3}, pre-launcher: N_d=3x10^{18}cm^{-3}, launcher: N_d=1x10^{18}cm^{-3})

In such a situation, the electrons will be swept directly from the emitter into the collector and all transistor action will be lost. The result is that the base-emitter voltage required to keep the emitter current constant decreases 1:1 with the increasing collector-base voltage as shown in figure 3.9.

The pre-launcher is also used to lower the conduction band barrier at the base-launcher interface (barrier B in figure 3.5) to reduce the possibility of the electrons reflecting from the interface and recombining inside the base. The best method is to match the material composition between the base and first part of the pre-launcher and include a gradual or step-like increase in material composition to the $Al_{0.3}Ga_{0.7}As$ material used inside the main launcher to confine the transverse optical mode. The post-launcher finally has to block the holes from escaping out of the active layer and leaking through the launcher into the base. The number of holes escaping is directly related to both the applied collector-base voltage and the valence band barrier between the active layer and the post-launcher (barrier F in figure 3.5). At first, the effect of a n.i.-doped heterojunction barrier at the GaAs-$Al_xGa_{1-x}As$ active layer to post-launcher interface is investigated (shaded points in figure 3.10) under the assumption that 40% of the difference in bandgaps falls across the valence band.

The barrier heights attainable using a simple heterojunction are limited to 200meV. Increased barrier heights are required since the image force, which results from the collector-base voltage, decreases this barrier even further. The solution for the hole leakage current is to introduce an

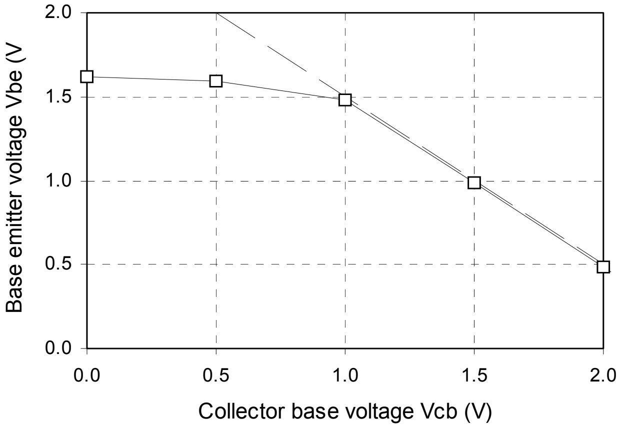

Figure 3.9: *Required base-emitter voltage V_{be} to keep the emitter current I_e constant at 30mA versus collector-base voltage V_{cb}; the onset of base punch-through occurs at V_{cb}=1.0V and V_{be} decreases equally with V_{cb} afterwards indicating all transistor action to be lost (I_e=30mA, base: N_a=6x10^{17}cm^{-3}, pre-launcher: N_d=3x10^{18}cm^{-3}, launcher: N_d=1x10^{18}cm^{-3})*

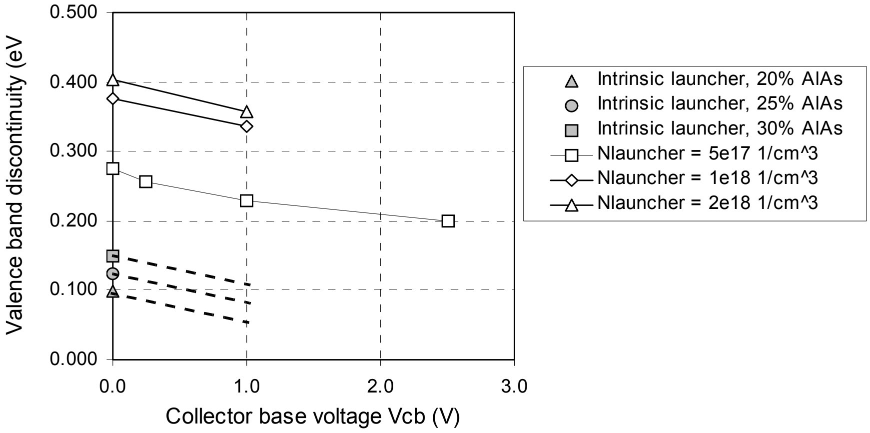

Figure 3.10: *Calculated and simulated values for the valence band discontinuity between the active layer and launcher versus the collector base voltage V_{cb} for different AlGaAs compositions of the launcher and different heights of the n-type doping spike inside the post-launcher (I_e=50mA)*

extra dip inside the valence band by introducing an n-type doping spike inside the post-launcher. The barrier height which can now be reached increases substantially, as shown in figure 3.10, and a barrier height of 400meV is obtained using a doping spike of N_d=2x10^{18}cm^{-3}. The difference in the simulated 2-terminal collector-base current-voltage (IV) curves between a doping spike of N_d=5x10^{17}cm^{-3} and N_d=2x10^{18}cm^{-3} is shown in figure 3.11. Whereas the doping spike of N_d=5x10^{17}cm^{-3} is unable to keep the leakage current below 100mA at V_{cb}=2.0V, the doping spike of N_d=2x10^{18}cm^{-3} is able to maintain the leakage current below 1mA at the same collector-base voltage. These numbers were confirmed by previous designs of the hot electron injection laser, having no doping spike in the launcher, showing high leakage currents and the present design showing low leakage currents as plotted in figure 3.12.

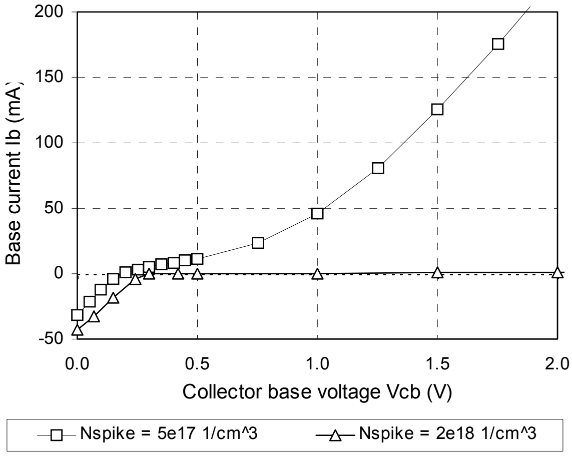

Figure 3.11: Simulated base current I_b versus collector base voltage V_{cb} for a lowly and highly doped n-type doping spike inside the post-launcher indicating, for positive values, the holes leaking across the active layer-to-launcher valence band barrier (I_e=50mA)

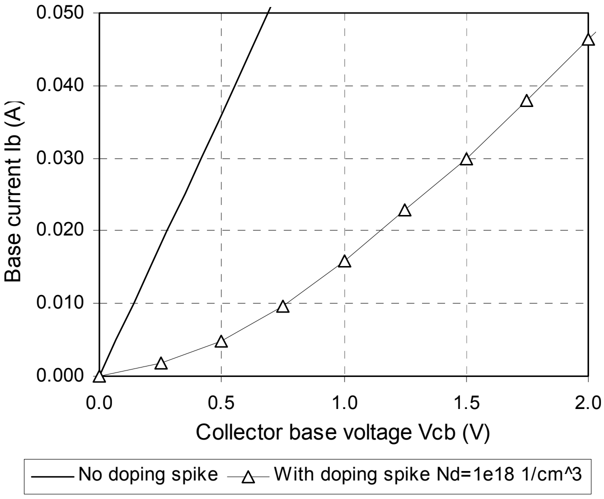

Figure 3.12: Measured base current I_b versus collector base voltage V_{cb} indicating the hole leakage current for previous generations of the hot electron injection lasers with a launcher without doping spike and a launcher with doping spike ($N_{d,spike}=1x10^{18}$ cm^{-3})

3.5.2 Effects on carrier heating efficiency

The introduction of the n-type doping spike does have a drawback on the conduction band profile and the transverse electric field profile across the launcher. The extra dip in the valence band is accompanied by a dip in the conduction band and a decreased electric field close to the end of the launcher as shown in figure 3.13. The n-type doping spike is actually capable of reversing the electric field which will slow down and cool the electrons again to some degree while going through the post-launcher. The height of the n-type doping spike is therefore a careful balance between the hole leakage current and the carrier heating efficiency of the

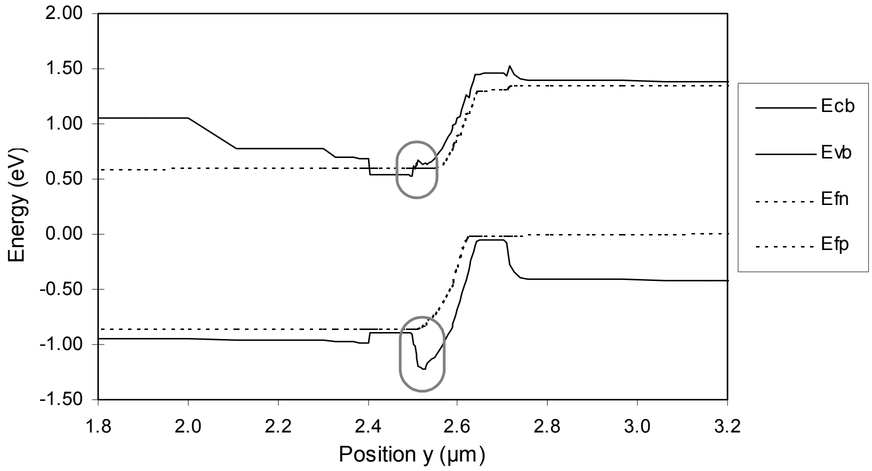

Figure 3.13: Simulated energy band diagram indicating both the dip inside the valence band and the reduced electric field inside the post-launcher caused by the n-type doping spike (I_e=50mA, V_{cb}=1V, post-launcher: N_d=1x10^{18}cm^{-3})

launcher design. Figure 3.14 shows the transverse electric field corresponding to the launcher's energy band diagram as shown in figure 3.13.

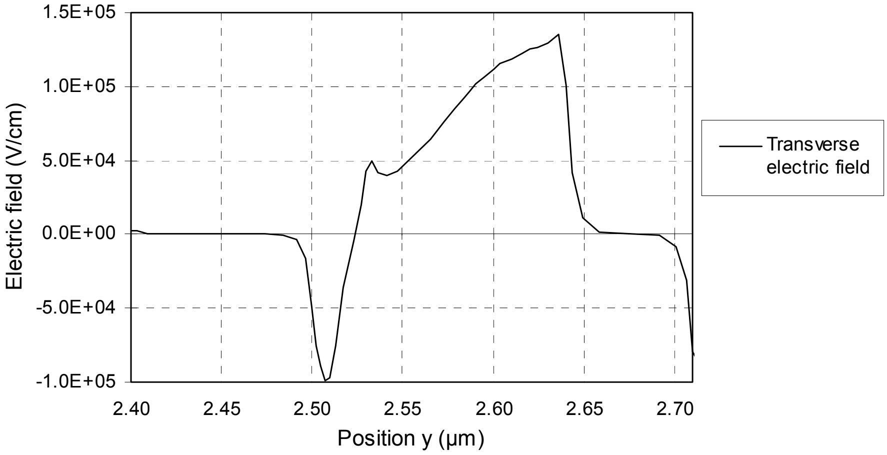

Figure 3.14: Simulated transverse electric field across the launcher through the center of the device indicating the negative electric field caused by the n-type doping spike inside the post-launcher (I_e=50mA, V_{cb}=1V)

The actual effect of the n-type doping spike on the carrier heating efficiency can be simulated using the same Monte Carlo routine as described in section 2.3. The electron scatter plot for such a launcher design at a heating voltage V_{cb} equal to 1.0V is shown in figure 3.15. It indicates that the negative electric field does decelerate and cool the electrons before they enter the active layer. Clearly visible is the accumulation of electrons inside the post-launcher across all three subvalleys, even inside the Γ-valley again. The net effect on the carrier heating efficiency as well as the difference in carrier heating efficiency as compared to the undoped launcher is shown in figure 3.16.

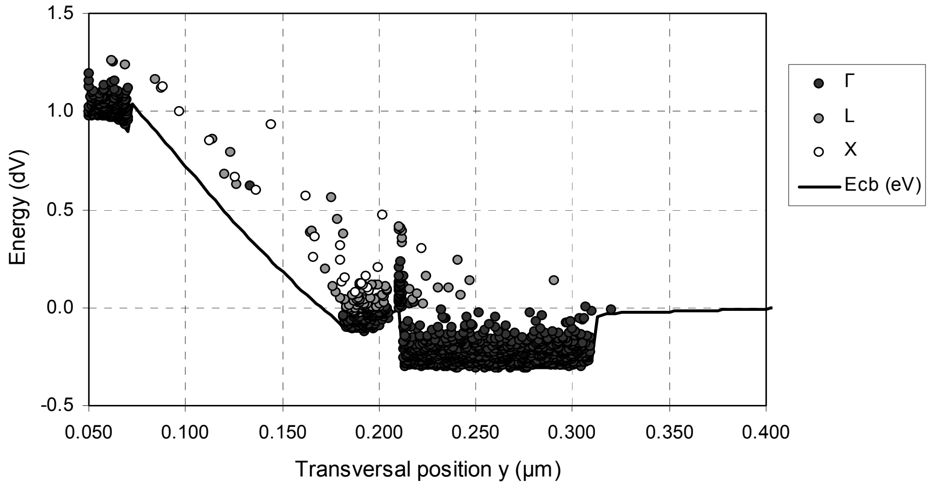

Figure 3.15: *Simulated electron scatter diagram using the Monte Carlo method showing the energy distribution across the* Γ, L *and* X *subbands within the launcher and active layer region for the* $Al_{0.30}Ga_{0.70}As$ *launcher with n-type doping spike inside the post-launcher:* $N_{d,spike}=1x10^{18}cm^{-3}$ *(T.G. van de Roer, private communication)*

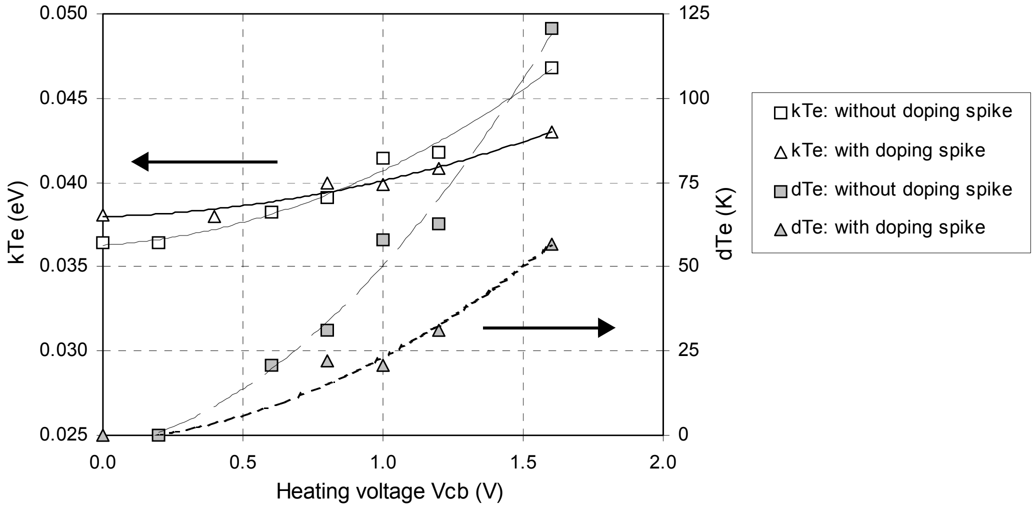

Figure 3.16: *Simulated carrier heating efficiency using the Monte Carlo method for both the standard* $Al_{0.30}Ga_{0.70}As$ *launcher and the* $Al_{0.30}Ga_{0.70}As$ *launcher with n-type doping spike inside the post-launcher indicating the elevated Fermi energy* (kT_e) *and relative increase in electron temperature* (δT_e) *versus the heating voltage applied across the launcher,* $N_{d,spike}=1x10^{18}cm^{-3}$ *(T.G. van de Roer, private communication)*

These simulations indicate that the carrier heating efficiency of the launcher with the n-type doping spike is about half the efficiency of the standard launcher. The n-type doping spike is required nonetheless to stop the holes from leaking out of the active layer and into the base, which would ruin the transistor behavior as shown in figure 3.12. The height of the doping spike can be reduced slightly to fit the required operating range in heating voltage V_{cb} more tightly.

Above this range, the hole leakage current is then allowed to increase rapidly. The current design has a safety margin for V_{cb} of around 4V at an operating range of 0V to 2.0V.

The length of the launcher is also a variable influencing the carrier heating efficiency. The launcher shouldn't be too long since the energy loss by phonon emission increases as well. Also more and more carriers will be transferred into the higher L and X valleys of the conduction band as shown in chapter 2. Those electrons will have to decay back into the Γ-valley first before they can take part in a photon-generating process. Besides, the carrier heating process becomes more indirect and the electrons gain sufficient energy to initiate other, possibly non-radiative, decay or recombination processes.

3.5.3 Optimizing the optical performance

Optimizing the optical performance involves optimizing the transverse optical mode profile, the lateral effective index step and the lateral gain profile. Optimizing the transverse optical mode profile means increasing its confinement within the active layer and decreasing its confinement inside the base layer. The base layer will have a material composition very close to the GaAs of the active layer due to improved transistor properties for a small bandgap base inside heterojunction bipolar transistors. It will also be highly p-type doped, again for improved transistor behavior as explained in section 3.3. Optical absorption and free carrier absorption within the base layer become an issue and the confinement of the optical mode has to be minimized. The optical mode profile is influenced by the material composition and doping levels of all layers surrounding the active layer. Both the base and the launcher are located above it and are fairly limited in their design window. The pre-cladding and cladding layers below the active layer have more degrees of freedom. The doping of the pre-cladding should remain limited to prevent free carrier absorption, typically on the order of $10^{17}cm^{-3}$ with a 25nm n.i.d. setback layer in between. The AlAs content of the main cladding should be relatively high to block any modal overlap with lossy substrate modes, typically 50% AlAs. What remains is the material composition and the thickness of the pre-cladding layer. Figure 3.17 shows the transverse optical mode profile through the center of the device versus the $Al_xGa_{1-x}As$ material composition in the p-type pre-cladding layer. The targets are to reduce the confinement factor of the base, increase the confinement in the active layer and to make the transverse mode as symmetric as possible in order to improve the far field distribution. The actual confinement factors for these three material compositions of the pre-cladding are given in table 3.1. Higher percentages of AlAs inside the pre-cladding push the optical mode further away from the pre-cladding due to the lower refractive indices of these material compositions. As a result, the overlap of the transverse optical mode with the base layer also increases which will result in higher optical losses in this narrow bandgap material. The confinement factor of the active layer is also affected but doesn't increase substantially anymore above 20% aluminum. The optimum composition for the pre-cladding layer is therefore $Al_{0.2}Ga_{0.8}As$.

Waveguiding in the lateral direction is determined first of all by the lateral step in the transverse effective index of refraction as determined above and secondly by the lateral optical gain profile. Strongly index-guided lasers have special lateral designs mainly for current blocking purposes, which also result in high lateral effective index steps. This effect stabilizes the lateral waveguiding by rendering it independent of the varying gain profile along the junction plane. The lateral gain profile of figure 3.7 will result in some level of anti-guiding. Gain-guided lasers on the other hand depend mainly on the distribution of the optical gain and the carrier-induced variations in the effective index are in the order of $5x10^{-3}$ [12]. The intermediate solution, called

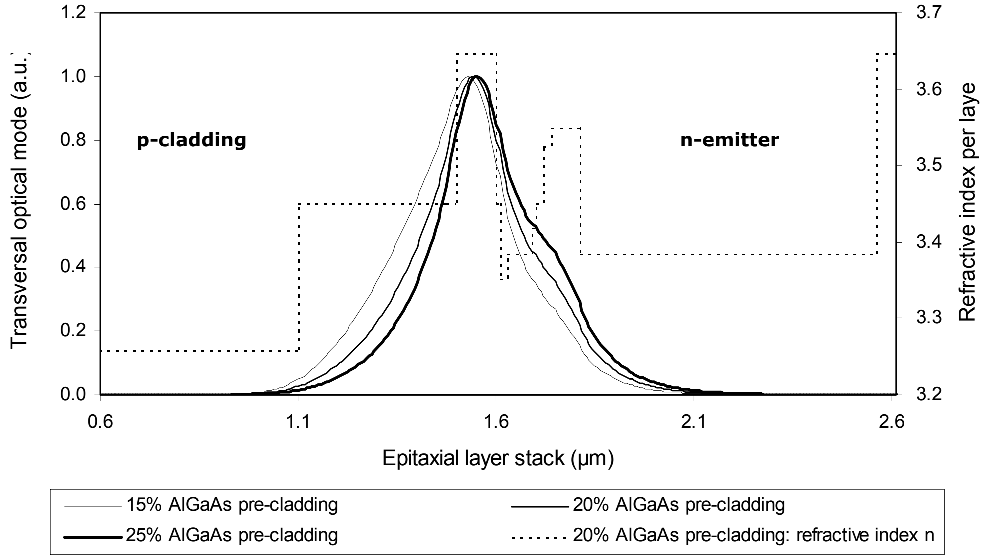

Figure 3.17: *Simulated transverse optical mode profiles versus AlGaAs composition of the p-type pre-cladding region*

Table 3.1: *Actual confinement factors of the transverse optical mode within both the active region and base layer versus AlGaAs material composition inside the p-type pre-cladding*

x $Al_xGa_{1-x}As$ pre-cladding	Γ_{act} **active region**	Γ_{base} **base layer**
0.15	0.267	0.043
0.20	0.284	0.062
0.25	0.288	0.081

weakly index-guided lasers, uses ridge and channel like structures to induce an effective index step in the order of $1x10^{-2}$, just above the carrier-induced variations [12]. Only in the case of very strong variations in the active layer's lateral carrier distribution does the gain-guiding become dominant again. The effective indices of the transverse optical modes within and outside the emitter ridge are given in table 3.2. The resulting effective index step equal to $1.2x10^{-2}$ means that the hot electron injection laser is weakly index-guided with stable lateral waveguiding.

Table 3.2: *Effective indices for the transverse optical modes within and outside the emitter ridge and the resulting step in effective index of refraction determining the lateral waveguiding*

Effective refractive index	n_{eff}
transverse through the emitter ridge	3.471
transverse through the base contact	3.459
lateral step in effective index	0.012

The transverse optical mode profiles, both through the middle and just outside of the emitter ridge, are shown in figure 3.18.

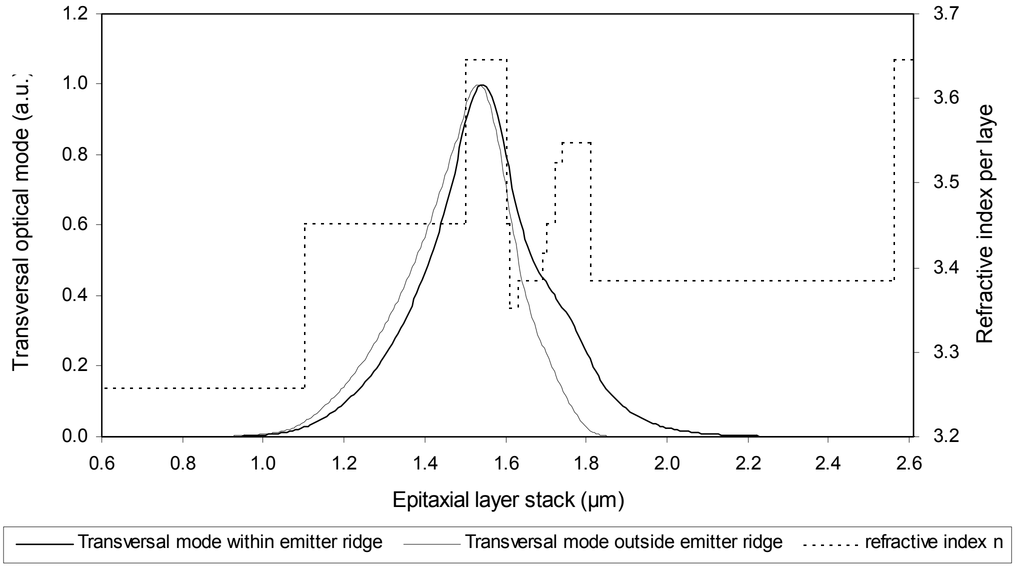

Figure 3.18: *Simulated transverse optical mode profiles within and outside the emitter ridge*

Both inhomogeneous injection of carriers into the active region and strong carrier diffusion within the active layer increase the carrier-induced antiguiding. Both effects are amplified in the case of the hot electron injection laser because electrons are injected through the top emitter contact as opposed to conventional lasers, which inject the electrons from the substrate side. The highly mobile electrons are injected here through the narrow emitter contact and diffuse outward inside the launcher and more strongly inside the active layer. There they recombine with the holes which show, at best, an evenly distributed injection from the p-type cladding region underneath, as shown in figure 3.6. In case the collector contacts are positioned on the sides of the main ridge for improved high frequency modulation, the injection of the less mobile holes is mainly along the outside of the ridge. The direct results of this are strong variations in the lateral optical gain profile, high levels of spontaneous emission and reduced differential external quantum efficiency (EQE), as shown in figures 3.7 and 3.19.

Purely for efficiency, the backside collector contact or a thick highly doped p^+-collector distribution layer are optimum. Note that a collector-up structure, injecting the holes from above, should also be considered since such a design would confine the radiative recombination processes again to the width of the narrow top ridge. The device would still be an NPN transistor in which the electrons are accelerated before entering the active layer but in this case with the launcher located underneath the active layer and above the transistor's base and emitter.

Even though the present design with side contacts to the collector does lead to strong spatial variations in the lateral gain profiles, it is crucial to emphasize that the current simulations, which do not take any carrier heating effects into account, show those gain profiles and indeed the lasing to be stable and constant during modulation of the heating voltage V_{cb}.

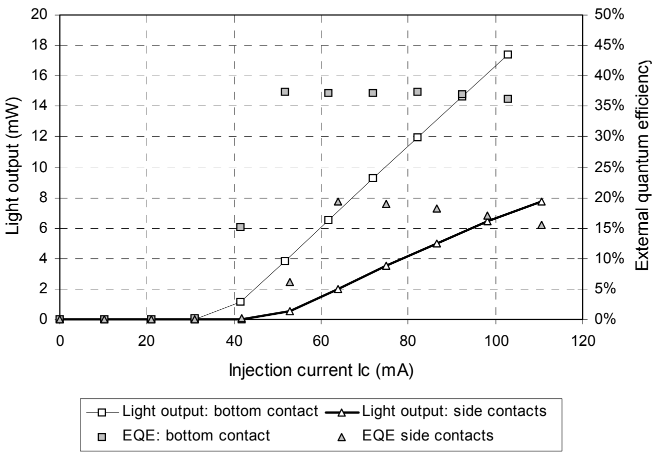

Figure 3.19: *Simulated light output versus injection current and external quantum efficiency for both cases of contacting the collector and injecting the holes: from the bottom side of the substrate and from both sides of the collector contact layer (V_{cb}=2.5V)*

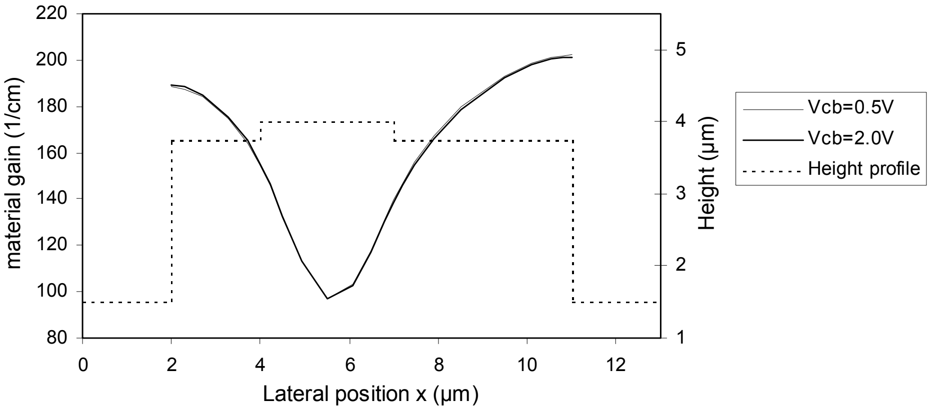

Figure 3.20: *Simulated lateral optical gain profile within the active layer versus the collector-base voltage V_{cb} (W_e=3µm, W_b=7µm, I_e=50mA)*

Figure 3.20 shows the spatial variation in the active layer's lateral gain profile for both low and high heating voltages V_{cb}. The strongest variations in material gain actually take place at both ends of the active region and thus outside the optical mode. The relative difference in material gain is +0.4% on the left and -0.4% on the right.

Since in these simulations no carrier heating and the associated gain reduction is included, the results of figure 3.21 show a constant and stable light output versus the heating voltage V_{cb}. The initial increase in P_{out} is due to the increase in the collector current I_c injecting more electrons into the active layer. The increase in injection current I_c at heating voltages greater than 1.0V is due to the hole leakage current from the active layer, through the launcher, and into the base. The light output P_{out} remains constant here.

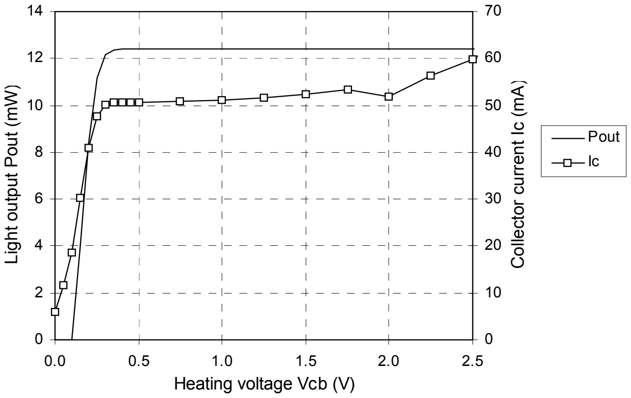

Figure 3.21: *Simulated light output P_{out} and collector current I_c versus the collector-base voltage V_{cb} (W_e=3µm, W_b=7µm, I_e=50mA)*

3.6 The actual design in the AlGaAs/GaAs material system

The current Hot Electron Injection Laser is implemented in the AlGaAs/GaAs material system due to the available design and processing experience at the start of this project. The thin layers, the various abrupt changes in material composition and sharp doping profiles require very precise epitaxial growth. Metal organic vapor phase epitaxy (MOVPE) at the Australian National University did provide such control over the growth process and provided us with the required epitaxial material. The epitaxial design has therefore been developed in collaboration with their Electronic Materials Engineering department, especially transforming the theoretical epitaxial design into the realistic and feasible epitaxial design as presented in table 3.3.

3.6.1 The epitaxial layer stack

The epitaxial layer stack of table 3.3 is the accumulation of all the design rules presented in this chapter and the experience gathered over several less fruitful iteration cycles of design, epitaxy, processing, and characterization. Critical doping levels have been reduced or the doping element (Zn) replaced by another element (C) with a lower diffusion constant, especially within the p^+-base layer. The emitter thickness has been increased from 250nm to 850nm to avoid possible resonances due to coupling of the mode with the high refractive index and lossy contact layers [9]. The thickness of the base layer has been increased and the n-type doping of the pre-launcher decreased to minimize base width modulation and to avoid punch-through of the base. Setback layers were introduced around the active layer to reduce dopant diffusion into the active layer and to reduce free carrier absorption. Doping levels within the pre-cladding and cladding layers were reduced, also to reduce free carrier absorption. The thickness and material composition of the pre-cladding was used to control the transverse optical mode. But most importantly, the launcher was tailor-made to fulfil all its requirements: low reflection of electrons at its base-launcher interface, evenly distributed transverse electric field and high valence band barrier to avoid hole leakage from the active layer.

3.6.2 Energy band diagram

The simulated energy band diagram of the actual design under normal forward bias is presented in figure 3.22 for two different heating voltages V_{cb} equal to 0V and 1.0V. Also included in figure 3.22 is the transverse optical mode, whose maximum is correctly centered within the

Table 3.3: Actual epitaxial design within the AlGaAs/GaAs material system

HEL	Thickness	Al [%]	Ga [%]	In [%]	As	P/N	Element	Doping [cm^{-3}]	Remark
Emitter contact	50 nm		100		x	N	Si	2.0E+18	Emitter contact layer
Emitter II	400 nm	30	70		x	N	Si	6.0E+17	
Emitter I	350 nm	30	70		x	N	Si	3.0E+17	
Etch stop	2.5 nm	100			x			i	AlAs etch stop layer 25A
Base & contact	**70 nm**	**7**	**93**		**x**	**P**	**C-delta**	**8.0E+18**	**Base contact layer**
	20 nm	10	90		x	N	Si	5.0E+16	
	20 nm	20	80		x	N	Si	5.0E+16	
	10 nm	25	75		x	N	Si	8.0E+16	
Launcher	60 nm	30	70		x	N	Si	1.0E+17	
	20 nm	35	65		x	N	Si	2.5E+18	
	5 nm	25	75		x	N	Si	1.0E+17	
n-Setback	5 nm	15	85		x			i	
Active Layer	**100 nm**		**100**		**x**			**i**	**100nm GaAs active layer**
p-Setback	25 nm	20	80		x			i	
Pre-Cladding	375 nm	20	80		x	P	C	1.0E+17	
Cladding	1000 nm	50	50		x	P	C	2.0E+17	
Collector buffer	100 nm		100		x	P	Zn	1.0E+18	buffer layer for Zn diffusion
Collector contact	900 nm		100		x	P	Zn	4.0E+18	Collector contact layer
Supperlattice/buffer			100		x	P		[Zn]	
Substrate			100		x	P		[Zn]~6-8e18	GaAs substrates, both p-type and S.I.

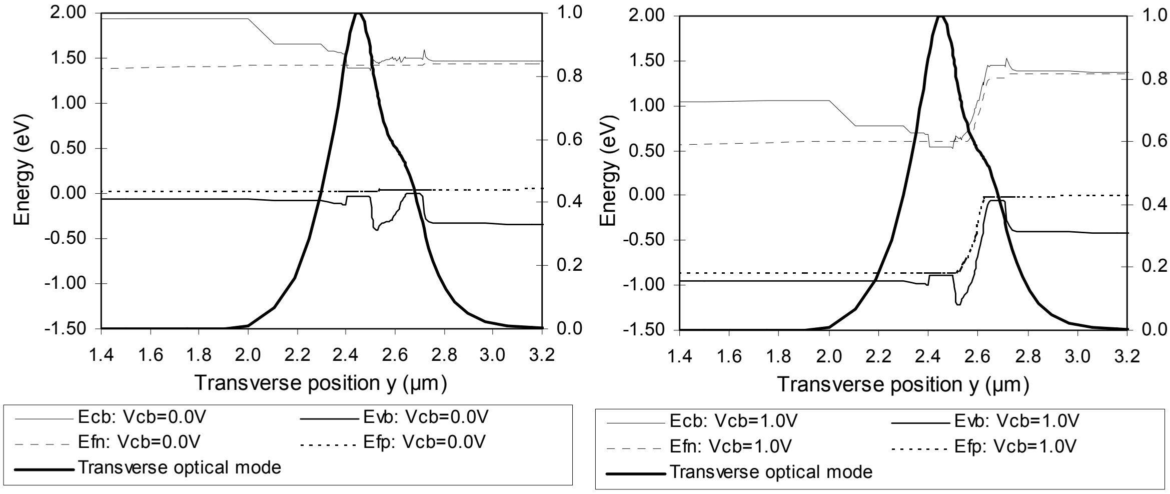

Figure 3.22: *Simulated energy band diagrams for the AlGaAs/GaAs design under normal forward biasing: I_e=50mA, V_{cb}=0V (thin), V_{cb}=1.0V (thick) (E_{cb}: conduction band energy level, E_{vb}: valence band energy level, E_{fn}: electron quasi-Fermi level, E_{fp}: hole quasi-Fermi level)*

active layer. The optical mode distribution is slightly asymmetric with a side lobe near the base. The simulated energy band diagrams agree with the expected profiles for the conduction and valence band, both at 0V and 1.0V. Thermionic emission and tunneling gets the electrons across and through the spike-like conduction band barrier from the emitter to the base. Hardly any barrier is visible inside the conduction band from the base into the launcher indicating proper design of the pre-launcher. The launcher's electric field is evenly divided across the pre-launcher and the main launcher, and the resulting electric field is expected to be fairly constant there. The n-type doping spike has introduced the dip inside the valence band of the post-launcher, which is still substantially deep at a heating voltage of 1.0V. The corresponding conduction band barrier, small but present, inside the post-launcher is also visible and will slow and cool the electrons down at the end of the launcher before entering the active layer. The band profiles within the active layer properly indicate the neutral flatband situation and the quasi-Fermi levels are already indicating inversion.

3.6.3 Electrical behavior

The simulated electrical behavior of the final design is presented in figures 3.23 and 3.24.

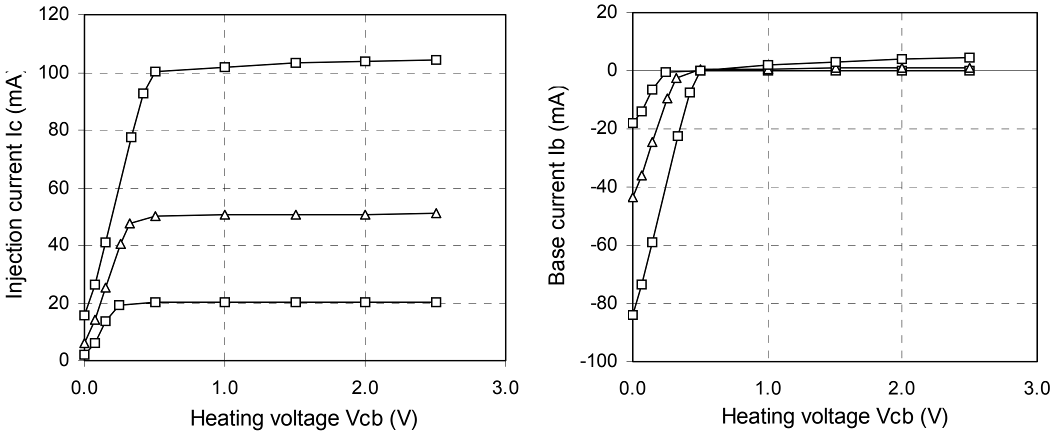

Figure 3.23: *Simulated common base current-voltage curves for the actual AlGaAs/GaAs design indicating the collector current I_c (left) and base current I_b (right) versus the collector-base voltage V_{cb} at constant emitter currents I_e equal to 20, 50, and 100mA*

The plots show proper electrical behavior with a stable and fairly constant operating range for the heating voltage V_{cb} between 0.5V and 2.5V. No degradation or breakdown is visible in this range. The transition region for $0V<V_{cb}<0.5V$ is necessary for the base transport factor to increase. More importantly, the simulations now indicate that the initial increase in V_{cb} is required to put an electric field in place, which prevents the electrons from flowing out of the active layer back into the base. This is the same electric field that accelerates them through the launcher. The required base-emitter voltage to keep the emitter current constant is given on the left-hand side of figure 3.24. These plots indicate a fairly constant base-emitter voltage and certainly not a strong influence from the heating voltage V_{cb} indicating that no strong base width modulation or base punch-through is present.

3.6.4 Simulated electro-optical performance

The optical performance is given in figure 3.24 as the light output power versus the injection current I_c and in figure 3.25 as the light output power versus the heating voltage V_{cb}.

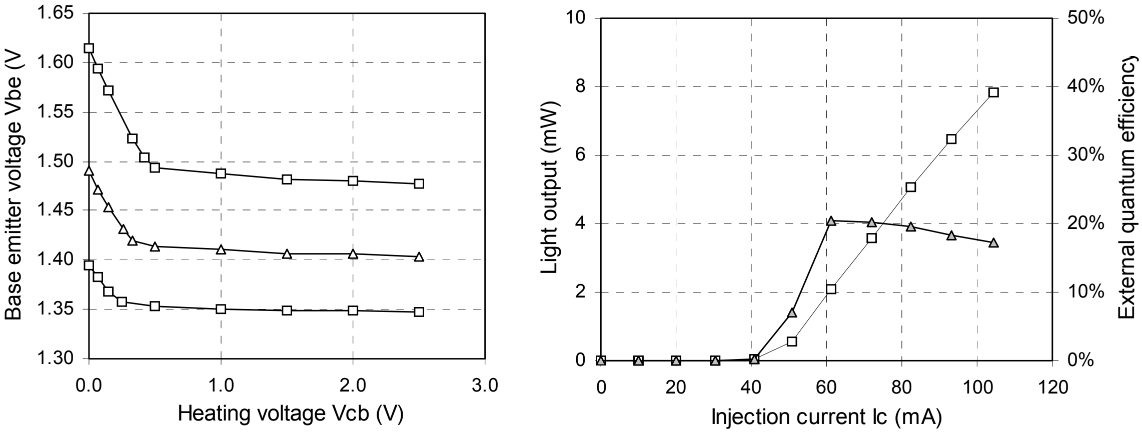

Figure 3.24: *Simulated common base light-current-voltage curves for the actual AlGaAs/GaAs design indicating the required base-emitter voltage* V_{be} *(left) and both the light output and external quantum efficiency (right) versus the collector-base voltage* V_{cb} *at constant emitter currents* I_e *equal to 20, 50, and 100mA*

These plots indicate stable optical behavior and output levels as expected when using collector contacts on both sides of the collector contact layer. And even though a strong spatial variation in the lateral gain profile is to be expected, the optical output power versus the heating voltage is fairly constant as shown in figure 3.25 (no carrier heating effects included in the simulation).

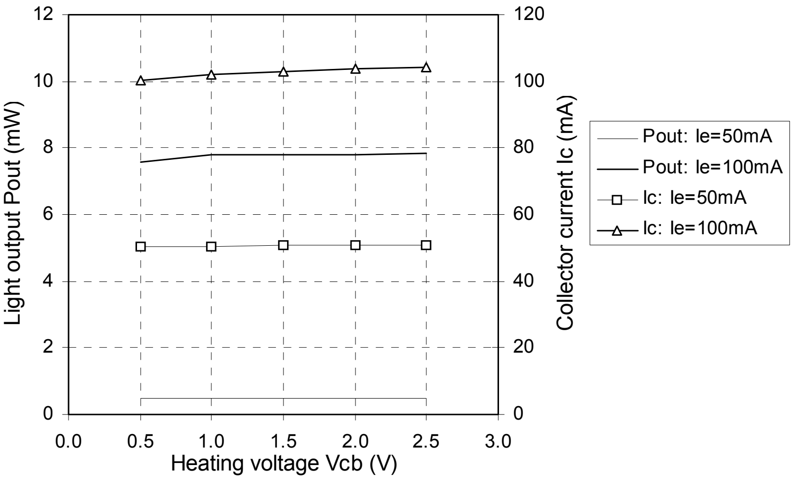

Figure 3.25: *Simulated common base light-current-voltage curves for the actual AlGaAs/GaAs design indicating the light output* P_{out} *and collector current* I_c *versus the heating voltage* V_{cb} *at different constant emitter currents* I_e *equal to 50 and 100mA*

3.7 The mask design

The previous sections within this chapter have already highlighted various critical aspects for the design in lateral direction. Most of them are implemented in the epitaxial design but the remaining design rules have to be implemented during the processing of the device. This chapter has also assumed a 2D design up untill now in both the transversal and lateral directions. The third, longitudinal direction was assumed uniform in composition and behavior across the fictitious cavity length of 500µm. Special care has to be taken during processing to ensure both uniform carrier injection and uniform carrier heating along the longitudinal axis of the device. Both measures will prevent dark spots and instabilities along that axis. Note that uniform carrier heating basically means a constant internal base potential in both lateral and longitudinal directions. These processing steps start with photographic lithography to transfer a pattern into the photoresist layer on the wafer surface. The actual patterns to be transferred are first etched into a chromium covered glass plate called the mask. The full set of masks is then used to process the full device step-by-step. The basic shape of the device is similar for the different designs since the optical waveguide runs vertically (longitudinal) and the contacting of the emitter, base and collector is performed from both horizontal (lateral) directions.

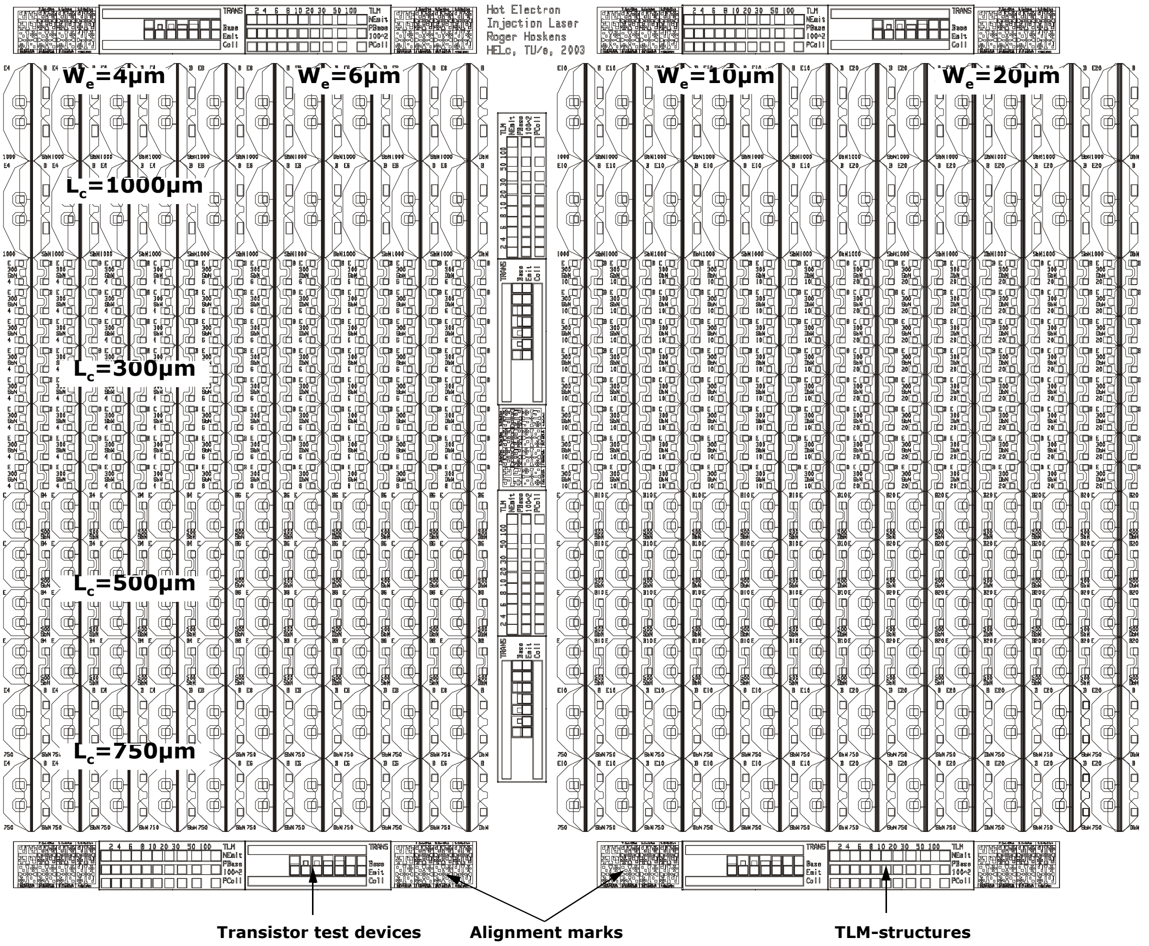

Figure 3.26: *Complete mask layout including various device designs, cavity lengths, alignment marks, test transistors, TLM structures*

3.7.1 The emitter and base-active layer ridges

Various emitter ridge widths are included on the mask layout to investigate the influence of the lateral optical mode profile on the threshold current density of this innovative vertically integrated transistor-laser. For each width of the emitter ridge at least 2 different widths were included for the base-active layer ridge to investigate the effect of the strong non-uniform lateral gain distribution as shown previously in figure 3.7. The narrowest base ridge is the single-sided base (S.B.) contact, which contacts the base using a single p-type ohmic contact on top of the base layer on the right-hand side of the emitter ridge. The wider base ridge is the double-sided base (D.B.) contact, which contacts the base using base contacts on both sides of the emitter. The single-sided base contact is expected to result in the lowest threshold-current density due to less spontaneous emission losses in the active layer outside the emitter ridge. The summary of the different ridge widths, including the ratio of emitter ridge width over base-active layer ridge width, is given in table 3.4. The effective width of the emitter after etching its ridge is approximately 1µm narrower: 3, 5, 9 and 19µm. The widest emitter ridge of 20µm indeed has the highest ratio W_e/W_b=58.8% (S.B.) and the narrowest emitter ridge of 4µm has the lowest ratio W_e/W_b=21.4% (D.B.). These differences are expected to result in substantial differences in the threshold current density for devices with strong non-uniform lateral gain profiles. These are the devices processed on the S.I. GaAs substrate with collector contacts on both sides of the base-active layer ridge. These ridges and thus the longitudinal waveguide run along the vertical axis in figure 3.26. The separate bars are obtained by cleaving the wafer along the correct crystallographic plane to obtain the front and rear mirror facets. These cleave planes run along the horizontal axis in figure 3.26.

Table 3.4: *Width of the base-active layer ridge as defined on the mask plate versus the designed width of the emitter ridge and the type of base contact*

	Emitter ridge width (µm)			
Type of base contact	***4***	***6***	***10***	***20***
	Base-active layer ridge width			
Single-sided (*SB*)	18	20	24	34
Double-sided (*DB*)	n/a	28	32	42
	Ratio W_e/W_b (%)			
Single-sided (*SB*)	22.2%	30.0%	41.7%	58.8%
Double-sided (*DB*)	n/a	21.4%	31.3%	47.6%

3.7.2 Basic device layout for different cavity lengths

The basic designs for the different cavity lengths L_c of 300, 500, 750, and 1000µm are shown in figure 3.27. The contact pads are laid out in such a way that coplanar microwave probes can be used for on-chip characterization. The central tip of the left probe contacts the emitter with both common tips on the collector interconnect pad. The right probe on the other hand contacts the base interconnect pad and again both outer tips contact the collector pads. When using the microwave probes for on-chip measurements, the common-collector configuration is the best choice to maintain pulse shape integrity.

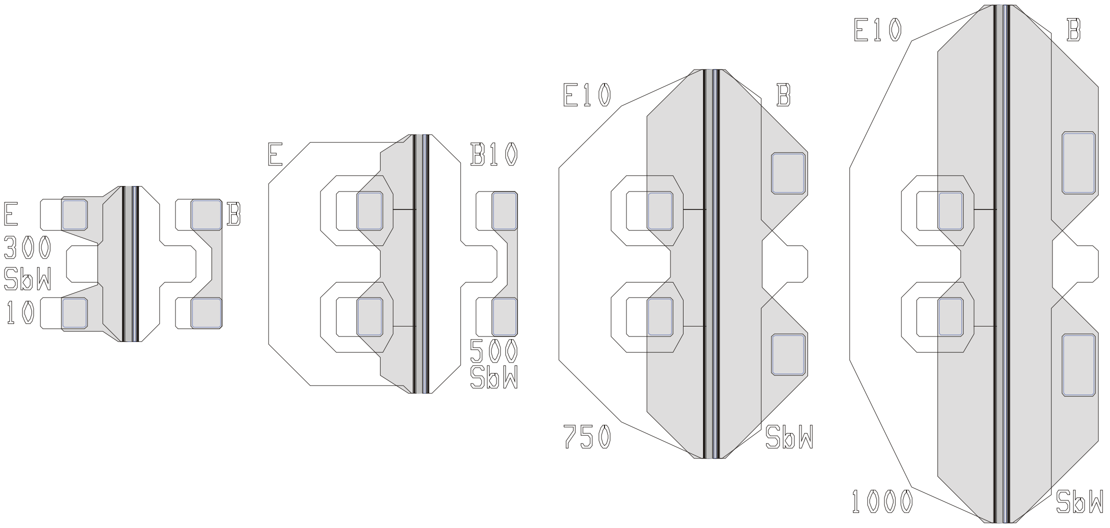

Figure 3.27: *Mask layout of the basic device design for the different cavity lengths L_c=300, 500, 750, and 1000µm (gray areas: TiPtAu base and collector ohmic contacts, white areas: TiAu interconnect pads, contact pad layout: middle-left=emitter, middle-right=base, outer pads=collector)*

3.7.3 Metallization

The current design of the device layout is purely optimized for longitudinal uniformity, low hole leakage currents and proper D.C. transistor and lasing behavior. Wide overlapping metal pads are used to reduce series resistances, longitudinal voltage drops causing inhomogeneous longitudinal carrier injection and heating. These large overlapping pad surfaces, with a thin layer of dielectric SiN_x in between, result in substantial parasitic parallel capacitances C_{eb} and C_{bc} which means this design is definitely not optimized for high frequency performance.

3.7.4 Test structures and alignment marks

Also visible in figure 3.26 are the additional structures, which are included for process alignment and on-wafer testing. The alignment marks are added to aid the alignment of the current mask plate to previous processing steps during device fabrication as discussed in the next chapter. A reference mark is evaporated in metal onto the wafer surface during a previous processing step and the current mask plate is accurately aligned using optical lithography. Here it is crucial to avoid continuously increasing misalignment due to a repeated use of reference mark, alignment, reference mark, alignment etc. The best option is to place all reference marks during the first processing step and to align all subsequent steps to those. A hybrid solution was chosen here in which new reference marks were placed, during the e-beam evaporation of the TiPtAu metal stack for the base and collector ohmic contacts, halfway through the processing of the device. This solution was implemented because the exact location of the base and collector contacts is crucial for the subsequent alignment of the openings in the dielectric SiN_x and the TiAu metal interconnect pads.

Additional structures were added to the mask set to allow tracking of the fabrication process, initial current-voltage testing and basic parameter measurements for subsequent modelling as shown in the following chapters. Structures were included to allow the use of the linear transfer length method (TLM) to test for ohmic contact behavior and to obtain values for the contact and sheet resistances as shown in chapter 5. Test transistors were also added for on-wafer measurements of the basic 2-terminal and 3-terminal current-voltage behavior even during device fabrication. These small rectangular transistors facilitated quick evaluation of the epitaxial design, growth and the preceding processing steps. Improper transistor behavior resulted in direct termination of that run and initiated another cycle of characterization (Polaron, IV, SEM, etc.), design, epitaxial growth and device fabrication.

References

[1] V.I. Tolstikhin and M. Mastrapasqua, “Three-terminal laser structure for high-speed modulation using dynamic carrier heating,” *Appl. Phys. Lett.*, vol. 67, pp. 3868-3870, 1995.

[2] Z.M. Li, S.P. McAlister, and C.M. Hurd, “Use of Fermi statistics in two-dimensional numerical simulation of heterojunction devices,” *Semicond. Sci. Technol.*, vol. 5, pp. 408-413, 1990.

[3] Z.M. Li and J. Piprek, “Simulation software gives laser designers insight,” *Laser Focus World*, Jan. 2000, p. 225.

[4] Z.M. Li, “*Physical models and numerical simulation of modern semiconductor lasers,*” Proc. SPIE, vol. 2994, pp. 698-708, 1997.

[5] Z.M. Li, Y. Wu, and R. Rambaran, “Simulation software tackles diode laser design,” *Laser Focus World*, Nov. 1996. pp. 233-234.

[6] S.M. Sze, *Physics of Semiconductor Devices*, John Wiley & Sons, 1981.

[7] R.C.P. Hoskens, T.G. van de Roer, and G.A. Acket, “Hot Electron Injection Laser: The Internal Base Potential,” *Proc. of the 25th Workshop on Compound Semiconductor Devices and Integrated Circuits*, WOCSDICE 2001, May 27-30 2001, Cagliari, Sardinia.

[8] B.G. Streetman, *Solid State Electronic Devices*, Prentice Hall, 1990.

[9] M. Buda, *Low-confinement high-power semiconductor lasers,* Thesis, Technische Universiteit Eindhoven, 1999.

[10] J.L. Liou, *Principles and Analysis of AlGaAs/GaAs Heterojunction Bipolar Transistors*, Artech House, 1996.

[11] N. Balkan, *Hot Electrons in Semiconductors, Physics & Devices*, Oxford University Press, 1998.

[12] G.P. Agrawal and N.K. Dutta, *Semiconductor lasers*, Kluwer Academic Publishers, 1993.

[13] J.S. Yuan, *SiGe, GaAs, and InP heterojunction bipolar transistors*, John Wiley & Sons Inc., 1999.

[14] S. Imanaga, H. Kawai, K. Kaneko, and N. Watanebe, “Monte Carlo simulation of AlGaAs/GaAs hot-electron transistors,” *J. Appl. Phys.*, vol. 59, pp. 3281-3288, 1986.

[15] B. Jalali and S.J. Pearton, *InP HBTs growth, processing, and applications*, Artech House Inc., 1995.

[16] A.S. Kyuregyan and S. N. Yurkov, “ Room-temperature avalanche breakdown voltages of p-n junctions made of Si, Ge, SiC, GaAs, GaP, and InP.,” *Sov. Phys. Semicond.*, vol. 23, pp. 1126-1132, 1989.

Chapter 4

Device fabrication

FABRICATING THE HOT ELECTRON INJECTION LASER INVOLVES THE ACTUAL EPITAXIAL GROWTH OF THE DESIGNED LAYER STACK AND THE SUBSEQUENT CHARACTERIZATION OF THESE LAYERS. IT ALSO INVOLVES TRANSFERRING THE SHAPES WITHIN THE MASK DESIGN ONTO THE GROWN WAFER. THE THREE-TERMINAL HOT ELECTRON INJECTION LASER DIFFERS STRONGLY FROM ANY CONVENTIONAL TWO-TERMINAL DIODE LASER IN THAT IT PUTS STRONGER REQUIREMENTS ON THE EPITAXIAL LAYERS AND THAT IT REQUIRES THE ADDITIONAL BASE CONTACT TO CONTROL THE BASE POTENTIAL AND THUS THE ELECTRIC FIELD ACROSS THE LAUNCHER. AND IN SPITE OF ITS NARROW ELONGATED DESIGN, THE PROCESSING SHOULD STILL RESULT IN HOMOGENEOUS CARRIER INJECTION AND IN A CONSTANT BASE POTENTIAL ALONG THE CAVITY OF THE LASER.

4.1 From design to device

Fabricating the Hot Electron Injection Laser involves putting the design into reality, in all three dimensions. Realizing the transverse design, i.e. the epitaxial layer stack, means careful epitaxial growth of the different layer compositions, thicknesses and doping levels. The epitaxial growth and the subsequent characterization of the grown layers are described in section 4.2. Implementing the other two dimensions, namely the lateral and longitudinal directions, means transferring the shapes of the different layers of the mask design onto the grown wafer. This processing of the epitaxial layers is described step-by-step in section 4.3.

4.2 Epitaxial growth

The current Hot Electron Injection Laser is implemented in the AlGaAs/GaAs material system due to the available design and processing experience at the start of this project. The thin layers, the various abrupt changes in material composition and sharp doping profiles require very precise epitaxial growth. Metal organic vapour phase epitaxy (MOVPE) at the Electronic Materials Engineering department of the Australian National University did provide such control over the growth process and provided us with the required epitaxial material. Subsequent characterization of this material using electrochemical capacitance-voltage profiling showed that the special techniques they applied resulted in well defined material composition, layer thickness and sharp doping profiles.

4.2.1 AlGaAs/GaAs based implementation

The vertical integration of the laser and the transistor yields, in effect, a completely novel type of semiconductor device. Along with the device came its own set of rules and complexities. To be able to tackle these, the choice was made to stay within the available experience, the AlGaAs/ GaAs semiconductor material system. Device properties are clearly targeted towards fiber communication which implies using the InGaAsP/InP material system. The current AlGaAs/ GaAs based implementation already revealed the importance of strict control over the material composition within the base, the multi-heterojunction launcher and the importance of strongly reduced p-type dopant diffusion within the base-launcher-active layer region. This knowledge can then be used to implement an InGaAsP/InP based hot electron injection laser.

4.2.2 AlGaAs material composition

Clearly visible in table 3.3 is the multilayer design of the launcher region. All of these thin layers, each with its own AlGaAs composition and doping level, have their own specific contribution to the correct behavior of the launcher as described in section 3.5.1. Precise control over the AlGaAs composition within such very short growth cycles is therefore required to implement the correct current-voltage and carrier heating behavior into the launcher.

The bandgap of the base is kept relatively small to increase the current injection efficiency as described in section 3.3.1. In fact its bandgap is a careful balance between carrier injection efficiency and optical absorption due to the active layer having only a slightly smaller bandgap and being at close proximity to the base. A small decrease in the AlAs content of the base will immediately result in higher optical waveguide losses. Precise control over the AlGaAs composition, even with the high p-type doping of the base, is therefore required to implement the correct optical behavior into the transistor-laser.

4.2.3 Dopant diffusion

Besides correct material composition, correct dopant levels and minimal dopant diffusion are at least equally important to the performance of the Hot Electron Injection Laser. This device, as opposed to a conventional NPN heterojunction bipolar transistor or PIN diode laser, is in fact a PINPN structure (collector-active layer-launcher-base-emitter). Sharp and stable doping profiles inside the epitaxially grown material are crucial for correct device behavior. Relatively small amounts of p-type dopant diffusion into the n-type launcher can ruin the transistor behavior as described in section 3.5.1. Diffusion of dopants into the active layer is also known to increase the threshold current density through a decrease in carrier lifetime and therefore increase in internal losses [1].

In AlGaAs grown using metalorganic vapor phase epitaxy (MOVPE), Silicon (Si) is the most common n-type dopant and Zinc (Zn) the most common bulk p-type dopant. Zn however suffers from fast diffusion throughout the structure with enhanced Zn diffusion in the presence of high n-type doping levels [2]. Previous implementations of the Hot Electron Injection Laser using only Zn as p-type doping did show strong Zn diffusion, which rendered the launcher p-type and resulted in a non-transistor like PIPPN (≈PN) structure. Carbon (C) is a well known alternative for Zn thanks to its lower diffusion coefficient [7]. To overcome the limitations of Zn doping, the technique of using background Carbon incorporation from the trimethylaluminum (TMAl) precursor was developed at the Electronic Materials Engineering Department of the Australian National University in Canberra, Australia [7][8]. It involves the incomplete decomposition of the TMAl at the growth surface resulting in the co-incorporation of the methyl radicals bound to Al [8]. This technique is used to grow:

- highly p^+ Carbon δ-doped AlGaAs layers, e.g. the base layer, and
- Carbon doped bulk AlGaAs layers of much lower doping levels, e.g. the p-type cladding layers.

δ-Doping is the technique of doping incorporation during a growth stop to confine the dopants to one atomic layer [8]. The benefits are higher average doping levels while maintaining sharp dopant diffusion profiles and generally lower sheet resistances in the plane of growth. Zn, on the other hand, is still used for doping those bulk AlGaAs layers requiring high levels of doping such as needed inside the collector layer. The onset of and the Zn diffusion process itself therefore still need to be understood. Hobson [2] reported the redistribution of Zn inside AlGaAs heterojunction bipolar transistors to be a predominantly native defects involved diffusion process. The predominant species involved are Ga vacancies [V_{Ga}] and Ga interstitial atoms (Ga_i) through the kick-out mechanism.

$$Ga_{Ga} + Zn_i^+ \Leftrightarrow Zn_{Ga}^- + Ga_i + 2h^+ \qquad 4.1$$

According to Deppe, the Ga interstitial atom concentration [Ga_i] in n^+ layers is one order larger than in i-GaAs layers [5]. As a result, the highest level of Si n-type doping was restricted to $2x10^{18}$ cm^{-3} in order to inhibit the onset of long distance interstitial or substitutional Zn diffusion within the layer stack. Carbon doping suffers much less from these effects due to the fact that carbon occupies the Arsenic instead of the Gallium sublattice [9].

4.2.4 Epitaxial growth

The epitaxial growth was performed on both semi-insulating (SI) and Zn-doped p^+ epi-ready ⟨100⟩ GaAs substrates using metalorganic chemical vapor deposition (MOCVD) at the Electronic Materials Engineering Department of the Australian National University, Canberra, Australia. The epitaxy started by growing the 900 nm thick Zn-doped GaAs collector contact layer, which was followed by the 100 nm thin GaAs collector buffer layer using a lower Zn doping level of $1x10^{18}$ cm^{-3}. Decreasing the Zn-doping level from $4x10^{18}$ to $1x10^{18}$ cm^{-3} in this final part of the collector contact layer contributed to the decreased amounts of Zn diffusion into the rest of the layer stack. The most important contribution to the strongly reduced Zn diffusion was relying on the background carbon incorporation from the aluminum source TMAl when growing the subsequent 1000 nm thick $Al_{0.5}Ga_{0.5}As$ cladding layer and 375 nm thick $Al_{0.2}Ga_{0.8}As$ pre-cladding layer. These layers had targets for the p-type doping of $2x10^{17}$ and $1x10^{17}$ cm^{-3} respectively.

Epitaxy continued by growing the unintentionally doped (UID) 100 nm thin GaAs active layer, surrounded by a 25 nm UID $Al_{0.2}Ga_{0.8}As$ setback layer on the p-cladding side and a 5 nm UID $Al_{0.15}Ga_{0.85}As$ setback layer on the launcher side. Next in line was the 135 nm thin n-type launcher region composed of the 20 nm $Al_{0.35}Ga_{0.65}As$ n-type Si doping spike of $2.5x10^{18}$ cm^{-3} near the active layer followed by various layers with compositions ranging from $Al_{0.3}Ga_{0.7}As$ to $Al_{0.1}Ga_{0.9}As$ and Si-doping levels ranging from $1x10^{17}$ to $5x10^{16}$ cm^{-3} to evenly distribute the applied electric field across the full launcher region and to minimize the potential barrier in the conduction band from the base into the launcher. The next epitaxial step involved the growth of the 70 nm thin p-type $Al_{0.07}Ga_{0.93}As$ base using carbon δ-doping to reach the required average doping level of $8x10^{18}$ cm^{-3} while maintaining very sharp diffusion profiles on either side of the base. A 2.5nm AlAs etch-stop layer was inserted next for processing purposes. The three-step emitter region completed the layer stack. This emitter region is composed of a 350nm $Al_{0.3}Ga_{0.7}As$ layer with a Si-doping level of $3x10^{17}$ cm^{-3}, a 400nm $Al_{0.3}Ga_{0.7}As$ layer with a slightly higher Si-doping level of $6x10^{17}$ cm^{-3} and finally the 50nm GaAs emitter contact layer using a Si doping level of $2x10^{18}$ cm^{-3}.

4.2.5 Electrochemical dopant profiling

Section 3.5 clearly shows that the actual, electrically active, doping levels directly determine the electro-optical device properties. A Bio-Rad Polaron PN4200 profile plotter was therefore used to perform electrochemical dopant profiling of the grown layer stack. The electrochemical cell used to contact the semiconductor surface and perform the capacitance-voltage measurement is shown in figure 4.1.

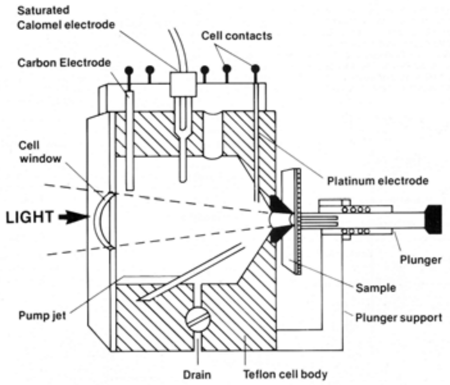

Figure 4.1: *Schematic diagram of the electrochemical cell used in the Polaron PN4200 profiler indicating the teflon cell body containing the electrolyte, the position of the sample, the platinum electrode, the carbon counter electrode and the saturated calomel reference electrode (source: Bio-rad Polaron PN4200 manual)*

The semiconductor sample is placed behind the opening on the right-hand side of the cell and contacted using the working electrode on either its front side (insulating substrates) or its backside (conducting substrates). The cell is filled with the electrolyte, 1M NaOH, and the three electrodes are inserted to contact the electrolyte. The platinum electrode, together with the electrolyte, is used for the actual capacitance-voltage measurement. The carbon counter electrode can be used for etching the semiconductor and facilitate the depth profiling. The saturated calomel electrode is used as a reference against which the potential is measured. The potential drop across the electrolyte can be neglected in the case of a concentrated electrolyte (> 0.1M). The result is a standard Schottky junction at the interface. The standard expression for the voltage-dependent width of the depletion region *d(V)* penetrating into the semiconductor yields the expression for the junction capacitance C_j:

$$C_j(V) = \frac{\varepsilon A}{d(V)} = \varepsilon A\left[\frac{q}{2\varepsilon(V_0 - V)}N\right]^{1/2} \qquad 4.2$$

Here A denotes the area of the contact between semiconductor and electrolyte, V_0 the dark rest potential (analogous to build-in potential), V the applied potential and N the majority carrier concentration inside the semiconductor. Rewriting equation 4.2 shows that this doping level can be calculated using the slope of the inverse square of the junction capacitance versus voltage plot.

$$\frac{1}{C_j^2(V)} = \frac{2}{q\varepsilon A^2}\frac{(V_0 - V)}{N} \Rightarrow N = -\frac{2}{q\varepsilon A^2}\left[\frac{d}{dV}\left(\frac{1}{C^2}\right)\right]^{-1} \qquad 4.3$$

The actual capacitance versus voltage measurement is now performed using ac signals measured with respect to the platinum electrode. Equation 4.3 yields the quantitative doping level and the sign of the slope of the $C_j(V)$ plot yields the doping type. N-type material will show a negative slope; the capacitance decreases with increasing potential. P-type material will show a positive slope; the capacitance increases with increasing potential above its rest potential.

The electrolyte can also be used to etch through the semiconductor to create a depth profile of the doping level but the depth resolution is degraded by non-uniformity across the etch pit, especially in the case of strong varying material compositions as present here [10]. Repetitive anodic oxidation under constant voltage and the subsequent removal of the formed oxides was used here to etch through the semiconductor layers in a very controlled manner in order to improve the depth resolution [17]. The electrolyte used for the anodic oxidation contained 1 unit of the solution containing 3 grams citric acid monohydrate in 100 ml D.I.-H_2O and 2 units Ethylene Glycol. Ammonia (28%) was used to bring its pH value to 6. The oxides themselves were removed in a 1 unit HCl (32%) and 10 units D.I. H_2O solution [11]. Table 4.1 gives an overview of the anodic oxidation process parameters for both GaAs and $Al_{0.5}Ga_{0.5}As$.

Table 4.1: *Various parameters of the anodic oxidation process for both GaAs and* $Al_{0.5}Ga_{0.5}As$ *under constant voltage condition* (V_{DC}=120V)

	V_{DC}=120V	
Material	***GaAs***	***$Al_{0.5}Ga_{0.5}As$***
Oxide color	Red	Blue-violet
Thickness	1.3 nm/V	1.1 nm/V
Total thickness	~ 0.15µm	~ 0.13µm
Rest current	< 0.5 mA/cm^2	< 0.5 mA/cm^2
Dissolution time in 10% solution of HCl (38%)	~ 1 min	~ 3 to 4 min

Even though capacitance-voltage measurements are less accurate close to p-n junctions and heterojunctions, these measurements still give an indication of the type of doping as well as estimates of the doping levels. Figure 4.2 shows both the type and level of the targeted (*_target*) and measured (*_cv*) doping levels on the S.I. GaAs wafer.

These results indicate that the actual doping levels and profiles agree very well with their target values. The base layer has a high average p-type doping level around 1x10^{19} cm^{-3} with very sharp profiles on both sides. The first, low-doped, part of the launcher is very important for device behavior by extending the applied electrical field across the full launcher but its doping level is difficult to distinguish in figure 4.2 since the depletion region extends directly into the n-type doping spike at the end of the launcher. The active layer didn't suffer from dopant indiffusion and has indeed very low doping levels (<1x10^{16}cm^{-3}). The pre-launcher has actually a slightly lower C-doping level, which will only result in a small voltage offset due to its limited thickness. Both the emitter and the thicker cladding layers reached their targeted doping levels

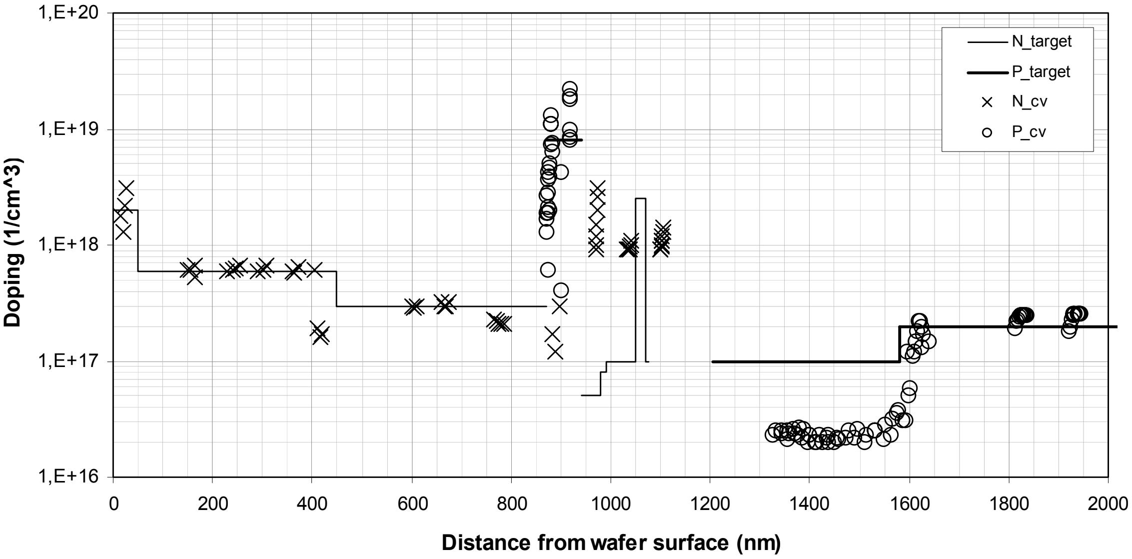

Figure 4.2: *Active dopant concentrations measured using Polaron C-V profiling (x: n-type, +: p-type) versus designed dopant levels according to table 3.3 (dashed lines: n-type, full lines: p-type). Left side denotes the n-type emitter contact layer at the surface of the wafer. Right side denotes the p-type collector contact layer grown directly on top of the S.I. GaAs substrate.*

4.3 The process-flow

The primary goal of the process-flow used to fabricate the Hot Electron Injection Laser is to obtain the long narrow optical waveguide for the diode laser and to provide electrical contact to the three contact layers of the elongated transistor. This process-flow, as shown in figure 4.3, consists of three wet-chemical etching steps to define the ridges, SiN_x deposition to isolate various metallic contact and interconnect layers, two ohmic metal evaporation steps and one metal interconnect evaporation step. The complete process overview is described in full detail in appendix A.

4.3.1 Emitter ridge etch

Etching through the 800nm thick emitter and stopping on top of the 70nm thin base requires a highly selective etchant in order to ensure homogeneous electrical and waveguiding properties along the ridge, i.e. the longitudinal direction. Any variations in etch depth will result in different and inhomogeneous refractive index steps along the sides of the emitter which directly degrade the waveguiding. The emitter also requires smooth sidewalls with positive slopes for direct interconnects to the emitter contact metal without requiring airbridges.

The combined requirements of high selectivity and smooth positive slopes within the AlGaAs-GaAs material system can be solved using wet chemical etchants. Citric acid (50% by weight) - hydrogen peroxide (30%) solutions ($C_6H_8O_7 : H_2O_2$ at ratio r:1) show higher etch rates through GaAs layers and lower etch rates through AlGaAs layers as shown in figure 4.4. The etchant utilizes the oxidation-reduction of the AlGaAs surface using hydrogen peroxide and the subsequent dissolution of the formed oxide using citric acid [12]. For ratios r greater than 2, the etch is reaction rate limited indicating a linear relationship between etch depth and etching time, and etched facets along crystallograhic planes [16]. For (100) oriented GaAs substrates, the

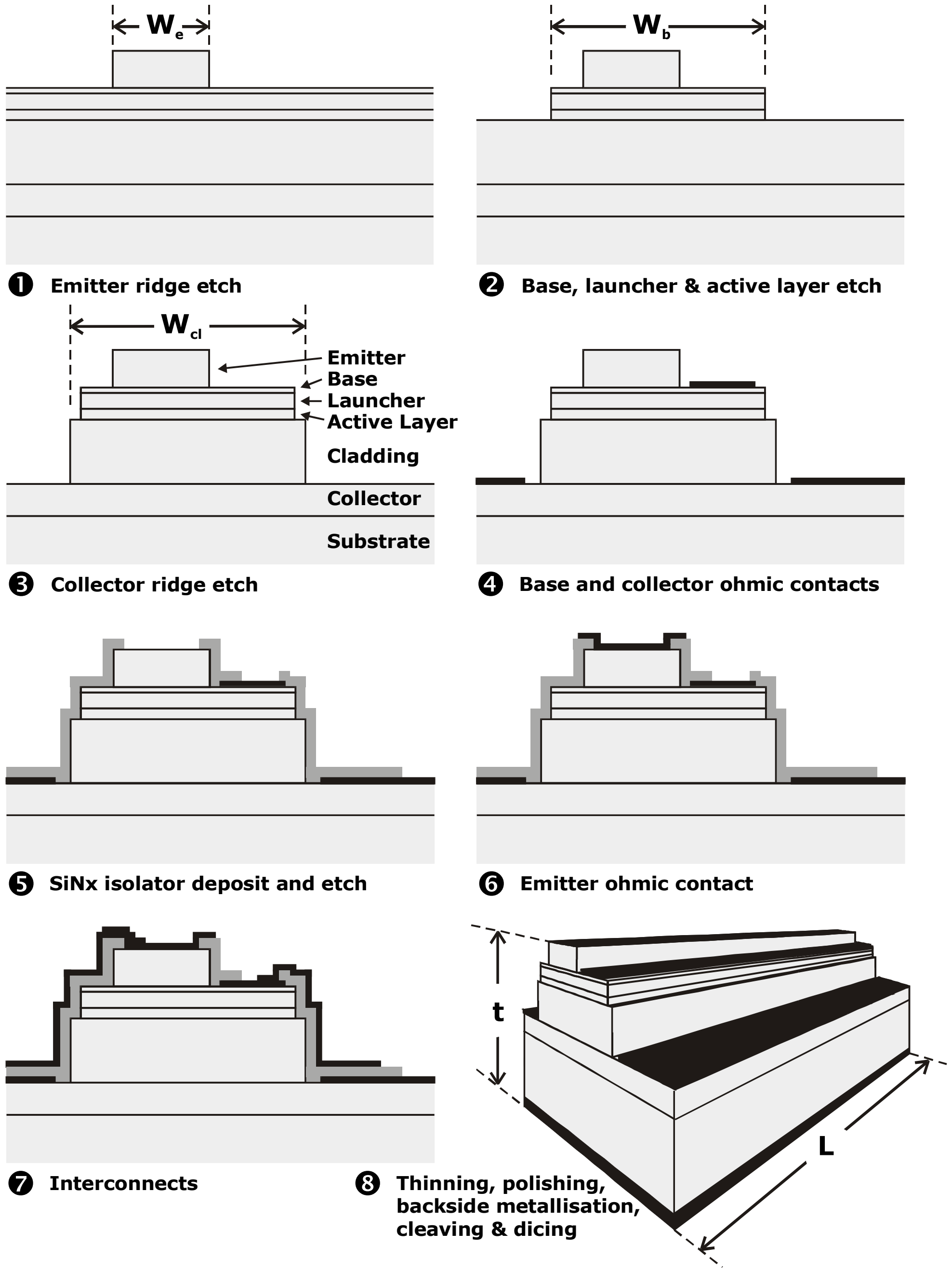

❶ Emitter ridge etch

❷ Base, launcher & active layer etch

❸ Collector ridge etch

❹ Base and collector ohmic contacts

❺ SiNx isolator deposit and etch

❻ Emitter ohmic contact

❼ Interconnects

❽ Thinning, polishing, backside metallisation, cleaving & dicing

Figure 4.3: *Schematic step-by-step diagram of the process-flow used to fabricate the Hot Electron Injection Laser*

actual etched facets along the [011] direction will be V-grooves at a 42° angle with the vertical and dovetails along the $[0\bar{1}1]$ direction [12]. Figure 4.4 shows that the selectivity of AlGaAs over GaAs depends on both the ratio *r* and the aluminum concentration due to a higher concentration of H_2O_2 oxidizing the semiconductor surface more rapidly and the resulting Al_xO_y dissolving much slower in citric acid [13]. The etching process in AlAs actually comes close to a full stop and periods of over 10 minutes have been reported necessary to etch through only a 30Å-thick AlAs layer (<0.30 nm/min) for a ratio *r* equal to 4 at 20ºC [13] and 9 minutes to etch through 10Å of AlAs (0.01 nm/min) for a ratio *r* equal to 4 at 0ºC [15]. These numbers yield a

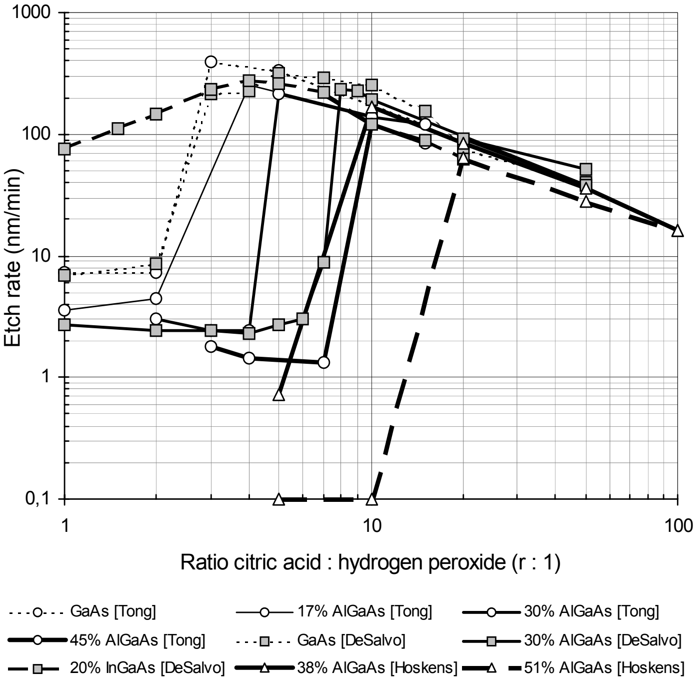

Figure 4.4: *Etch rates of various citric acid - hydrogen peroxide solutions versus AlGaAs material composition at 20°C*

selectivity of at least 1000 for GaAs over AlAs. This selectivity is still opposite to the one required to etch through the $Al_{0.30}Ga_{0.70}As$ emitter region onto the thin $Al_{0.07}Ga_{0.93}As$ base layer.

Adding a thin AlAs etch stop layer corrects the direction of the selectivity again. It also increases the attainable selectivity substantially. AlAs etch stop layers can be etched themselves using hydrogen chloride (HCl) solutions, which exhibit high selectivities of InAlAs over InGaAs [23] or hydrogen fluoride (HF 48%) solutions, which have been reported numerous times to show very high selectivities of AlGaAs over GaAs [20][21][22]. HF shows a strong selectivity for $Al_xGa_{1-x}As$ ($x > 0.40$) over GaAs and the etch rate versus aluminum concentration increases very rapidly between 40 and 50% aluminum. Etch rates as high as 16µm/min with a selectivity greater than 10^7 for AlAs over GaAs [22] have been reported by others. Strong lateral etching, as shown in figure 4.5, due to these high etch rates has to be minimized by using only a short dip in a strongly diluted HF solution (few drops of HF 48% into 200ml D.I. H_2O) to selectively stop on top of the thin $Al_{0.07}Ga_{0.93}As$ base layer. The surface of AlAs is very unstable because it oxidizes rapidly. These oxides are very resistant to a wide range of etchants and result in incomplete and inhomogeneous etching of the AlAs etch stop layer using the strongly diluted HF (48%). Part of the solution is to transfer the sample upside down between etchants with a drop of the citric acid - hydrogen peroxide etch solution clinging to the surface. This prevents additional oxidation of the AlAs layer to the air and continues the dissolving of the Al_xO_y by the citric acid. The other part of the solution is to keep the etchant rich in citric acid using a ratio $r > 5$ to avoid excessive oxidation of AlGaAs with higher aluminum concentrations. At high ratios $r > 50$, the etch solution becomes non-selective for $Al_xGa_{1-x}As$ ($x \leq 0.50$) and possible trenching starts to occur into the etched surface along the edge of the resist.

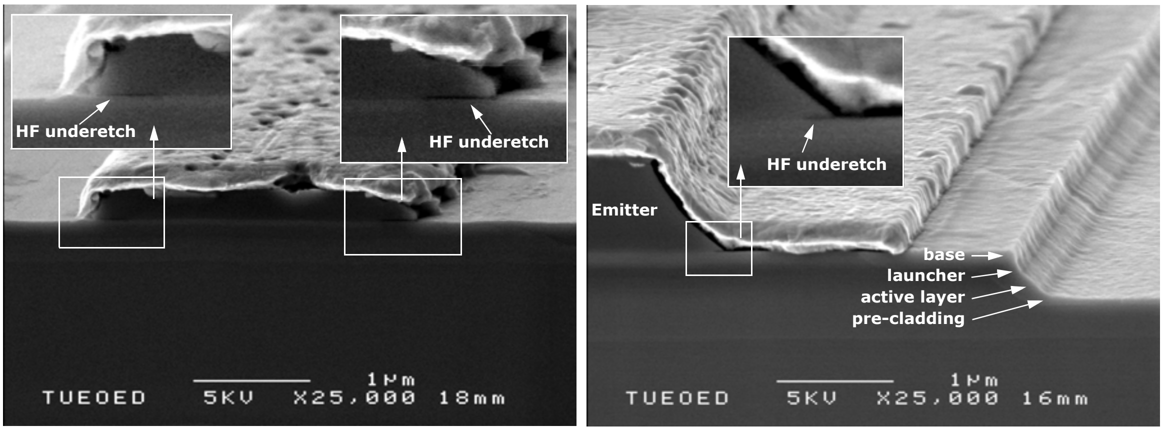

Figure 4.5: *SEM image showing the lateral undercut of the AlAs etch stop layer after a short dip in the strongly diluted HF (48%) solution*

A citric acid - hydrogen peroxide solution of ratio *r* equal to 10 is the perfect balance to selectively etch through the emitter (see appendix A for the process details). The actual etch rate at 20ºC is equal to 195nm/min for a sample etched upside down and without stirring. Direct wet transfer into a strongly diluted HF solution will selectively remove the AlAs layer itself. The width of the resulting emitter ridge varied from 3.8μm at the top to 4.9μm at the bottom when using a 6μm light field mask line and Microposit® S1805 positive resist. The full width series on the mask set is 4, 6, 10, and 20μm. The resulting shape and surface morphology of the emitter ridge is shown in figure 4.6.

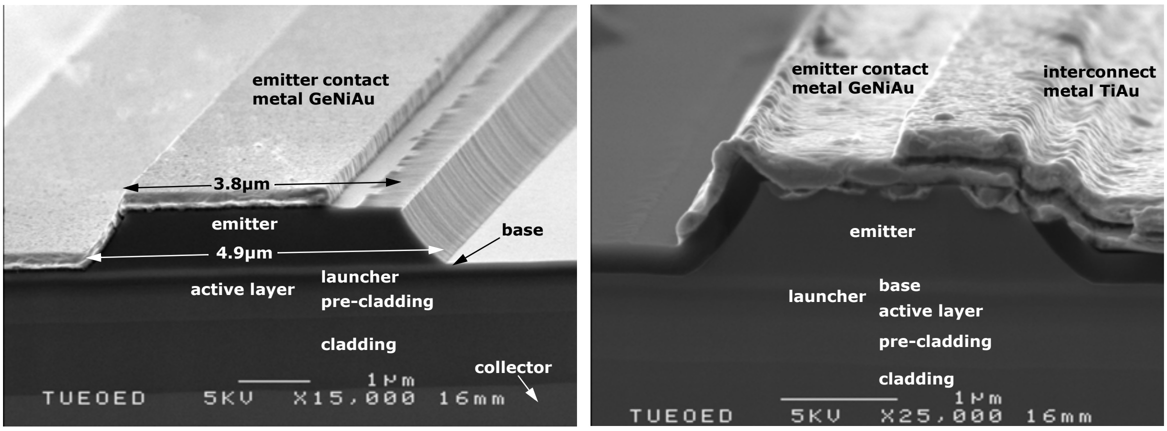

Figure 4.6: *SEM image showing both the shape (left & right) and the surface morphology (left) of the emitter ridge after etching it using the citric acid: hydrogen peroxide solution (r=10)*

4.3.2 Base, launcher and active layer etch

This extra base-width defining etch is required to obtain the narrowest possible width for the active layer while maintaining a decent width for the actual base contact metal and thus a decent level for the base series resistance. Besides etching through the base layer, this step also etches through the launcher and active layer, and ends halfway through the $Al_{0.20}Ga_{0.80}As$ pre-cladding layer. It minimizes the width of the active layer and therefore the recombination losses on both sides of the lasing mode. After all, this laser injects highly mobile electrons which, once inside the active layer, will strongly diffuse away from the emitter ridge. Conventional lasers utilize an automatic confinement of the lateral conversion level inside the active layer through the topside injection of holes which are far less mobile than electrons. The different widths of the rectangular patterns on the light-field mask plate are given in table 4.2. They are determined by the width of the emitter ridge and by the choice between a single base contact on the right side of the emitter or two base contacts on opposite sides of the emitter ridge.

Table 4.2: *Width of the base-launcher-active layer ridge as defined on the mask plate versus the designed width of the emitter and the type of base contact*

Base contact	**Emitter ridge width (µm)**			
	4	***6***	***10***	***20***
Single base (*SB*)	18	20	24	34
Double base (*DB*)	n/a	28	32	42

This step uses the same etchant as for the emitter ridge: the citric acid - hydrogen peroxide solution of ratio r equal to 10 at 20ºC. The sample is also etched upside down and without stirring. The actual shape of the slope after etching is shown in the right-hand side picture of figure 4.5. The etch shows its typical profile and underetch. Also visible are the gray tones of the various layers it etched through.

4.3.3 Collector etch

The widths of the top two ridges are very critical because they directly influence the device performance in various ways. These critical widths were defined in the previous two etching steps. The only etching step remaining is defining the collector ridge. Its sole purpose is to be able to evaporate a contact metal on top of the collector contact layer. A non-selective etchant can be used due to the 1µm thickness of the collector layers. It does have to etch through the first 100nm of the collector in order to reach the higher doped part of the collector ($4x10^{18}$ instead of $1x10^{18}$ cm^{-3}, see table 3.3). The higher p-type doping of the collector will improve the electrical properties of the ohmic contact.

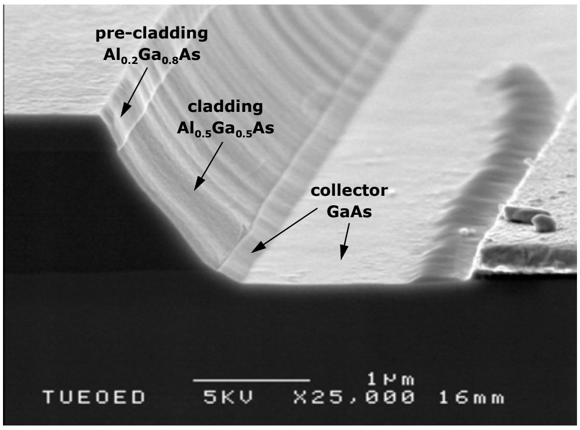

Figure 4.7: *SEM image showing both the shape and the surface morphology of the collector ridge after etching it using the $H_3PO_4 : H_2O_2 : CH_3OH$ (1:1:3) solution*

The other requirement for the collector ridge is yielding sidewalls with positive slopes for improved coverage of the interconnect metal. The etchant that suits these requirements is the phosphoric acid : hydrogen peroxide : methanol solution at a ratio of 1:1:3 at 0ºC as shown in figure 4.7. It shows how the solution etched through the remaining part of the pre-cladding, the cladding itself and approximately the first 200nm of the collector. The collector ridge itself extends about 2µm outwards from both sides of the base-launcher-active layer ridge.

4.3.4 Base and collector contact metal

Next in line is contacting the 70nm thin p-type base layer and the much thicker collector region which is also p-type (see A.2.5). Evaporating the base contact metals before depositing the SiN_x isolation layer yields a maximum distance of 2µm between the right side of the emitter ridge and the left side of the base contact, thereby minimizing the crucial base series resistance. Covering the base contact metal with the SiN_x isolator also minimizes the risk of creating a short circuit when evaporating the emitter contact metal afterwards. Furthermore, no surface treatment is used before evaporating the metal stack to avoid any risk of removing part of 70nm thin base layer. Rapid thermal annealing (RTA) of a TiPtAu metal stack on AlGaAs has also been reported to have caused up to one micrometer deep spikes into the semiconductor material. Such intermetallic spikes would bridge across the n-type launcher into the p-type cladding and effectively short circuit the base to the collector. Initial measurement on the ohmic test structures will reveal the extent of these RTA side effects.

The potential barrier between the metal and semiconductor surface ϕ_b, according to the Schottky-Mott model for p-type semiconductor-metal interfaces, is given by:

$$\phi_b = (\chi_s + E_g) - \phi_m \tag{4.4}$$

where χ_s is the electron affinity of the p-type semiconductor layer, E_g the semiconductor bandgap, and ϕ_m the metal work function, provided there is no Fermi level pinning at the metal-semiconductor interface due to, for example, interface states. Equation 4.4 tells us that the smallest potential barrier can be obtained using the metal with the highest work function. Platinum (Pt) is the metal having the highest work function of all commonly used metals, as shown in the shortened list of table 4.3. After deposition, Pt forms an inert interface with the semiconductor surface and a very thin depletion layer appears between Pt and the semiconductor. Pt also serves as a buffer layer against interdiffusion of the Ga and As on one side and the Au from the top metal layer on the other side. Pt does however suffer from poor adhesion to various semiconductor surfaces. A thin layer of Titanium (Ti) is therefore introduced between the semiconductor surface and the Pt layer to improve adhesion with the added benefit of serving as a getter for various contaminants, including oxides.

Table 4.3: *Different metals and their work functions*

Metal	Work function (eV)
Al	4.28
Ti	4.33
Ge	5.00
Au	5.10
Ni	5.15

Table 4.3: *Different metals and their work functions*

Metal	Work function (eV)
Pt	5.65

The metal stack was evaporated using an Airco Temescal E-beam evaporator at a base pressure of $2x10^{-6}$ Torr and consists of the following three layers: 50nm Titanium (Ti), 20nm Platinum (Pt) and 200nm Gold (Au). Subsequent rapid thermal annealing of the TiPtAu contact will result in interdiffusion of the Ti, the group III, and group V elements and the diffusion front will reach the Pt barrier whose sizable work function will reduce the potential barrier even further. This RTA step is only performed once on both p-type and n-type contacts, after the n-type emitter contact has been evaporated as well, as described in section 4.3.6. The results for the p-type base and collector contacts are already described here. The RTA step consists of a temperature ramp from 100ºC to 400ºC during 10 seconds and a stable part at 400ºC for 60 seconds in a Nitrogen (N_2) ambient. The effects of this temperature-time profile on the base and collector contacts were measured on the ohmic test structures using the linear transfer length method (TLM). The results for the base contacts after various process runs are shown in table 4.4. The base contact resistance of 15.6 Ω (1.56 Ωmm) is substantially higher than comparable values on bulk p-type GaAs layers of approximately 0.4 Ωmm. Possible causes are the limited thickness of the 70nm thin base and the δ-doping nature of this layer.

Table 4.4: *TLM measurement results for the p-type base contact for different process runs using 100x100 μm^2 contact pads and projections based on these results and the designed layer stack as given in table 3.3*

Process run	**TLM measurement results**						
	R_c (Ω)	R_c (Ωmm)	R_{sp} (Ωcm²)	R_{sh} (Ω/□)	L_t (µm)	μ_p (cm²/Vs)	r (Ωcm)
HELh1 SI-GaAs	14.7	1.47	3.0e-5	727	2.0	154	5.1e-3
HELh2 p-GaAs	16.4	1.64	3.6e-5	746	2.2	150	5.2e-3

Given the average doping level for the δ-doped base layer of $8x10^{18}$ cm^{-3}, the predicted values for the resistivity $r = 8x10^{-3}$ Ωcm and the mobility $\mu_p = 75$ cm^2/Vs [24] agree well with the values shown in table 4.4. The fact that the actual resistivity is lower and the actual mobility within the base layer is higher can be explained by the δ-doped nature of this base layer.

The collector layer itself has not been etched through due to the depth of the epitaxial layer stack, 2.74µm emitter to collector ridge, which already reduced the resist coverage across the top ridges. Etching through the collector layer (+0.8µm) would also have resulted in a decreased accuracy during subsequent steps like etching windows in the SiN_x isolation layer and the evaporation of the narrow emitter contact metal stack. Keeping the collector layer intact resulted in the absence of electrical isolation between adjacent devices and the absence of the mesa for the TLM method, thereby rendering the use of this method for the collector contact invalid. The resistance values obtained from measuring the collector ohmic test structures still give us an estimate for the total collector-to-collector resistance R_{cc}, laterally across the collector ridge as shown in table 4.5.

Table 4.5: *Estimates for the total collector-to-collector resistance R_{cc} after different process runs based on the resistance values measured using the collector ohmic test structures*

Process run	**Resistance value versus spacing**			**Rcc (Ω) L=500µm W_e=4-6µm**
	R (Ω) s=4µm	**R (Ω) s=20µm**	**R (Ω) s=100µm**	
HELh1 SI-GaAs	7.2	10.1	16.3	2.2
HELh2 p-GaAs	1.9	2.1	1.9	0.5

4.3.5 Silicon Nitride isolation layer

A dielectric film is deposited next across the whole sample, which serves the following two purposes: (a) as an isolation layer between metal layers to avoid creating a short between the emitter, base and collector, and (b) to passivate the exposed semiconductor surface. AlGaAs devices suffer from relatively high surface-state densities and high surface recombination velocities [25]. Regions of the device in which minority carrier transport is crucial, e.g. the extrinsic base region, should therefore get additional surface treatment.

The 250nm Silicon Nitride (SiN_x) film is deposited by plasma enhanced chemical vapor deposition (PECVD) using a System100 from Oxford Instruments at 300ºC (see A.2.6). The gas mixture and partial pressures of the Silane (SiH_4) and Ammonia (NH_3) sources are calibrated towards a fixed index of refraction between 1.93 and 1.94. The deposited SiN_x layer is subsequently etched to allow access to the emitter, base and collector contact layers. The etching is performed by reactive ion etching (RIE) using a System100 from Oxford Instruments. The use of only Sulfur Hexafluoride (SF6) ensures purely chemical etching with minimum physical damage to the exposed GaAs emitter contact layer (see A.2.6 for details). The process therefore allows overetching to ensure a complete etch across the sample. The deposited SiN_x film and the results of the RIE process to etch the openings through this layer are visible in figure 4.8.

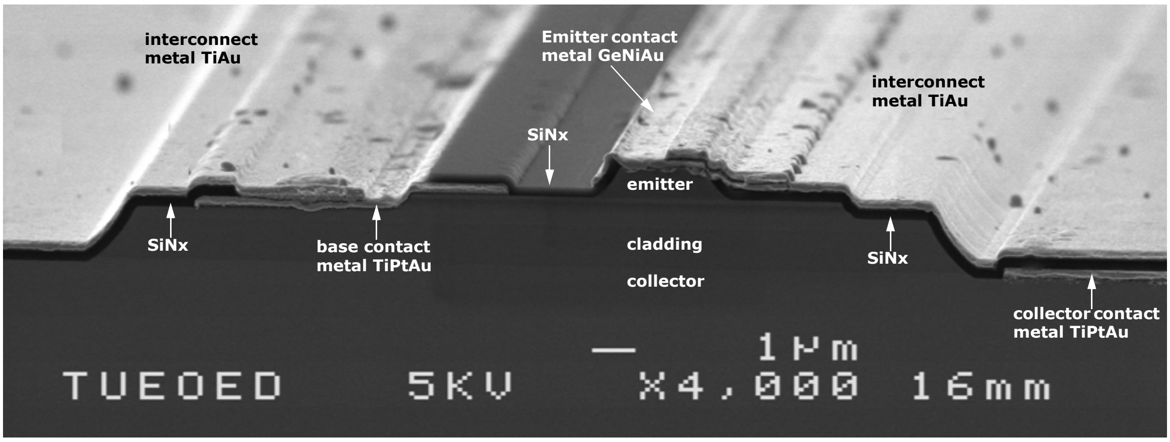

Figure 4.8: *SEM image showing a frontal overview of the etched ridges, contact metals and interconnects*

4.3.6 Emitter contact metal

With the opening through the SiN_x in place for the ohmic contact on top of the emitter ridge, the emitter contact metal stack is evaporated next and consists of the following three layers: 20nm Germanium (Ge), 15nm Nickel (Ni), and 200nm Gold (Au). Both Ni and Ge interact with the GaAs during the previously mentioned rapid thermal annealing (RTA) step. The actual purpose of this metal stack is for Ge to create a highly doped n^{++} top layer to further reduce the width of the depletion region and form a tunneling type ohmic contact. During the first part of the temperature ramp, Ni reacts with GaAs to form [26]:

$$xNi + GaAs \rightarrow Ni_xGaAs \qquad 4.5$$

A small portion of Ge is believed to be incorporated into the Ni_xGaAs and as the temperature ramp up continues, Ge interacts with the above ternary compounds in a process called *epitaxial regrowth* to form *x*NiGe and GaAs [26]:

$$xGe + Ni_xGaAs \rightarrow xNiGe + GaAs \qquad 4.6$$

Some of the Ge will be co-incorporated into the regrown GaAs, building up the n^{++}-GaAs layer between the GaAs semiconductor layer and the newly formed *x*NiGe layer. The results of the TLM measurements on the emitter ohmic test structures are given in table 4.6. The emitter contact resistance of 1.8 Ω (0.18 Ωmm) is in good agreement with published values for this type of metal-semiconductor interface [26][27].

Table 4.6: *TLM measurement results for the n-type emitter contact after different process runs using 100x100 μm^2 contact pads and projections based on these results and the designed layer stack as given in table 3.3*

Process run	**TLM measurement results**						
	R_c (Ω)	**R_c (Ωmm)**	**R_{sp} (Ωcm^2)**	**R_{sh} (Ω/□)**	**L_t (µm)**	**μ_n (cm^2/Vs)**	**r (Ωcm)**
HELh1 SI-GaAs	1.8	0.18	2.8e-6	116	1.6	5394	5.8e-4
HELhT p-GaAs	1.7	0.17	2.3e-6	120	1.4	5213	6.0e-4

Given the average doping level for the emitter contact layer of $2x10^{18}$ cm^{-3}, the predicted values for the resistivity $r = 1.2x10^{-3}$ Ωcm and the mobility $\mu_n = 2800$ cm^2/Vs [24] are worse than the actual values of table 4.4. These actual values are based on a single 50nm conductive layer with a doping level of $2x10^{18}$ cm^{-3}. The 750nm thick n-type region underneath, even though it has lower doping levels, also contributes to the total conductance, which improves again the values for the resistivity and mobility.

4.3.7 Interconnects

The interconnect metal connects the contact pads to the bonding pads. These bonding pads have a surface area of at least 90x60μm^2 to provide sufficient space for a wedge bond using thin Au wire. The Au layer is used as the conductor and bonding surface, and the Ti layer for improved adhesion, especially on top of the SiN_x dielectric film. This interconnect metal stack is also evaporated using the Airco Temescal E-beam evaporator at a base pressure of $2x10^{-6}$ Torr and consists of the following two layers: 50nm Ti and 200nm Au (see A.2.8 for details).

4.3.8 Post-processing fabrication steps

The post-processing steps consist of thinning and polishing the sample, placing the p-type ohmic contact on the backside of the sample if required, slicing the sample into laser bars and dicing these bars into separate lasers. These dices can then be placed on a TO5 header (see A.2.9 for specific details). In effect, the samples were thinned and polished to 100µm thickness and cleaved into bars of the following lengths: 300, 500, 750, and 1000µm (see figure 4.9). Some bars were also cleaved into separate dices and placed on a Cu-block, which on its turn was placed on a TO5 header using EPO-TEK H20E epoxy.

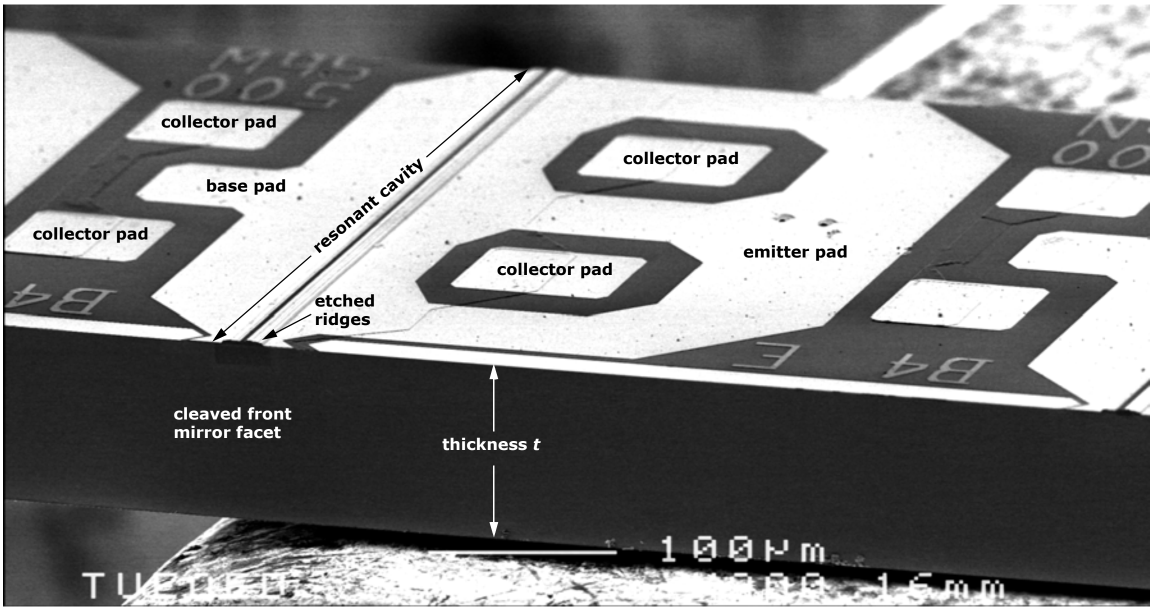

Figure 4.9: *SEM image of the laser bar after fabrication showing the front mirror facet, the resonant cavity (L=300µm) perpendicular to the front facet, the multi-layer interconnects, and the contact pads*

References

[1] J. Arias, I. Esquivias, J.D. Ralston, E.C. Larkins, S.Weisser, J. Rosenzweig, A.Schönfelder, and M. Maier, "Carrier profile for $In_{0.35}Ga_{0.65}As/GaAs$ multiquantum well lasers from capacitance-voltage measurements," *Appl. Phys. Lett.*, vol. 68, pp. 1138-1140, 1996.

[2] W.S. Hobson, S.J. Pearton, and A.S. Jordan, "Redistribution of Zn in GaAs-AlGaAs heterojunction bipolar transistor structures," *Appl. Phys. Lett.*, vol. 56, pp. 1251-1253, 1990.

[3] W.S. Hobson, S.J. Pearton, and E.F. Schubert, "Zinc delta doping of GaAs by organometallic vapor phase epitaxy," *Appl. Phys. Lett.*, vol. 55, pp. 1546-1548, 1989.

[4] R.K. Ball, P.W. Hutchinson, and P.S. Dobson, "Formation of gallium interstitials during zinc diffusion into gallium arsenide," *Phil. Mag. A*, vol. 43, pp. 1299-1314, 1981.

[5] D.G. Deppe, "Thermodynamic explanation to the enhanced diffusion of base dopant in AlGaAs-GaAs npn bipolar transistors," *Appl. Phys. Lett.*, vol. 56, pp. 370-372, 1990.

[6] P. Enquist and J.A. Hutchby, "Growth and diffusion of abrupt zinc profiles in gallium arsenide and heterojunction bipolar transistor structures grown by organometallic vapor phase epitaxy," *J. Appl. Phys.*, vol. 63, pp. 4485-4493, 1988.

[7] G. Li, S. Yuan, H.H. Tan, X.Q. Liu, S.J. Chua, and C. Jagadish, "$In_{0.2}Ga_{0.8}As$/GaAs quantum well lasers with C doped cladding and ohmic contact layers," *Journal of Electronic Materials*, vol. 27, p. 61, 1998.

[8] G. Li, M.B. Johnston, A. Babinski, S. Yuan, M. Gal, S.J. Chua, and C. Jagadish, "Si and C δ-doping for device applications," *Journal of Crystal Growth*, vol. 195, pp. 54-57, 1998.

[9] M. Borgarino, R. Plana, J. Graffeuil, L. Cattani, and F. Fantini, "The reliability of III-V semiconductor heterojunction bipolar transistors," *Proc. IEEE IEDM*, vol. 45, pp. 203-206, 1996.

[10] P. Blood, "Capacitance-voltage profiling and the characterisation of III-V semiconductors using electrolyte barriers," *Semicond. Sci. Technol.*, vol. 1, pp. 7-27, 1986.

[11] H. Hasegawa and H.L. Hartnagel, "Anodic oxidation of GaAs in mixed solutions of Glycol and water," *J. Electrochem. Soc.*, vol. 123, pp. 713-723, 1976.

[12] G. S. DeSalvo, W. F. Tseng, and J. Comas, "Etch rates and selectivities of citric acid/hydrogen peroxide on GaAs, $Al_{0.3}Ga_{0.7}As$, $In_{0.2}Ga_{0.8}As$, $In_{0.53}Ga_{0.47}As$, $In_{0.52}Al_{0.48}As$, and InP," *J. of Electrochem. Soc.*, vol. 139, pp. 831-835, 1992.

[13] M. Tong, D. G. Ballegeer, A. Katterson, E. J. Roan, K. Y. Cheng, and I. Adesida, "A comparative study of wet and dry selective etching processes for GaAs/AlGaAs/InGaAs pseudomorphic MODFETs," *Journal of Electronic Materials*, vol. 21, pp. 9-15, 1992.

[14] C. Juang, K. J. Kuhn, and R. B. Darling, "Selective etching of GaAs and $Al_{0.30}Ga_{0.70}As$ with citric acid/hydrogen peroxide solutions," *Journal of Vacuum Science Technology*, vol. B5, pp. 1122-1124, 1990.

[15] H. J. Lee, M. S. Tse, K. Radhakrishnan, K. Prasad, J. Weng, S. F. Yoon, X. Zhou, H. S. Tan, S. K. Ting, and Y. C. Leong, "Selective wet etching of a GaAs/$Al_xGa_{1-x}As$ heterostructure with citric acidhydrogen peroxide solutions for pseudomorphic GaAs/$Al_xGa_{1-x}As$/$In_yGa_{1-y}As$ heterojunction field effect transistor fabrication," *Materials Science and Engineering B*, vol. 35, pp.230-233, 1995.

[16] M. Otsubo, T. Oda, H. Kumabe, and H. Miki, "Preferential etching of GaAs through photoresist masks," *J. Electrochem. Soc.*, vol. 123, pp. 676–680, 1976.

[17] M. Buda, *Low-confinement high-power semiconductor lasers*, Thesis, Technische Universiteit Eindhoven, 1999.

[18] J.L. Merz, R. L. Logan, and A. M. Sergent, "GaAs integrated optical circuits by wet chemical etching," *IEEE J. Quantum Electron.*, vol. 15, pp. 72-82, 1979.

[19] X.S. Wu, L.A. Coldren, and J.L. Merz, "Selective etching characteristiscs of HF for $Al_xGa_{1-x}As$/GaAs," *Electron. Lett.*, vol. 21, pp. 558-559, 1985.

[20] Z.M. Chuang, J.W. Scott, D.B. Young, and L.A. Coldren, "Strained InGaAs/GaAs quantum well constricted-mesa lasers and application in a vertical-twin-guide tunable laser," *IEEE Photon. Technol. Lett.*, vol. 4, pp. 315-318, 1992.

[21] P. Wei-Zhen and C. Zong-Quan, "Selective etching characteristics of HF for $Al_xGa_{1-x}As$/GaAs," *Electron. Lett.*, vol. 21, pp. 558-559, 1985.

[22] E. Yablonovitch, T. Gmitter, J. P. Harbison, and R. Bhat, "Extreme selectivity in the lift-off of epitaxial GaAs films," *Appl. Phys. Lett.*, vol. 51, pp. 2222, 1987.

[23] N. J. Sauer and K. B. Chough, "A selective etch for InAlAs over InGaAs and for different InGaAlAs quaternaries," *J. Electrochem. Soc.*, vol. 139, pp. 10-11, 1992.

[24] A. Dargys and J. Kundrotas, *Handbook on physical properties of Ge, Si, GaAs, and InP*, Vilnius Science and Encyclopedia Publishers, 1994.

[25] W. Liu and J. Harris, "Diode ideality factor for surface recombination current in AlGaAs/GaAs heterojunction bipolar transistors," *IEEE Transactions on Electron Devices*, vol. 39, pp. 2726-2732, 1992.

[26] M.I. Lepsa, *Two and three terminal double barrier resonant tunneling devices*, Thesis, Technische Universiteit Eindhoven, 1997.

[27] J.S. Wellen, *Modelling, deisgn and fabrication of a GaAs-based integrated photoreceiver for short distance optical communication*, Thesis, Technische Universiteit Eindhoven, 1997.

Chapter 5

Device results

THE CORRECT VERTICAL INTEGRATION OF THE TRANSISTOR AND THE LASER HAS PROVEN TO BE THE MOST CHALLENGING PART OF THIS THESIS. THIS CHAPTER, WHICH REPORTS ON THE RESULTS OBTAINED, THEREFORE STARTS BY PRESENTING THE BASIC TRANSISTOR CURRENT-VOLTAGE CURVES. IT CONTINUES BY GIVING AN OVERVIEW OF THE OPTICAL PROPERTIES LIKE OPTICAL POWER VERSUS CURRENT CURVES, THRESHOLD CURRENT DENSITIES AND THE OPTICAL SPECTRUM. IT CONCLUDES WITH ESTIMATES FOR THE CARRIER HEATING EFFICIENCY.

5.1 Scope

The results reported in this chapter were obtained from a single epitaxial wafer grown on a semi-insulating GaAs substrate with the layer structure of table 3.3 and processed in a single run according to appendix A. Intra-wafer variations are stated where available. The mask set used for this process run included devices with emitter ridge widths equal to 4, 6, 10 and 20µm. The 4 and 6µm devices suffered from non-ohmic emitter contacts leaving only the 10 and 20µm ridge widths for these measurements. Both emitter ridge widths are available with single-sided (SB) and double-sided (DB) base contacts and cavity lengths of 300, 500, 750 and 1000µm.

5.2 Measurement set-up

The required measurements include two-terminal and three-terminal current-voltage (IV) transistor measurements and three-terminal light output-current-voltage (LIV) laser-transistor measurements. The optical behavior is characterized using its optical spectrum and light output. The low power transistor measurements are constant voltage (DC) controlled for accuracy. The higher power measurements to characterize the laser use short pulsed excitation (300-500ns) to minimize device heating. By avoiding lattice heating, variations in light output can be linked more directly to any carrier heating modulation present in the hot electron injection laser. Figure 5.1a shows the schematic diagram of the measurement set-up. A universal test set for DC and pulsed IV measurements is used to generate the results presented here [2]. This set can operate in DC, pulse only, or DC + pulse mode. It uses the common principle of a Bias Tee to mix and separate the DC and pulse signals using an inductor and capacitor respectively, as shown in figure 5.2. The test set automatically switches both DC sources and both pulse sources between the different 2-terminal and 3-terminal operating modes and allows for fully automated measurements of the integrated transistor-laser. Both 3-terminal modes used in these measurements, common-base and common-collector, are illustrated in figure 5.1b. The light generated by the device, both spontaneous emission (SE) and stimulated emission, is collected into a 1 mm diameter core multimode (MM) fiber using direct coupling between the laser facet and the fiber. This fiber is coupled to either an optical spectrum analyzer (OSA) or a PIN photodiode to measure the optical spectrum or the temporal response of the optical signal, as shown on the right-hand side of figure 5.1.

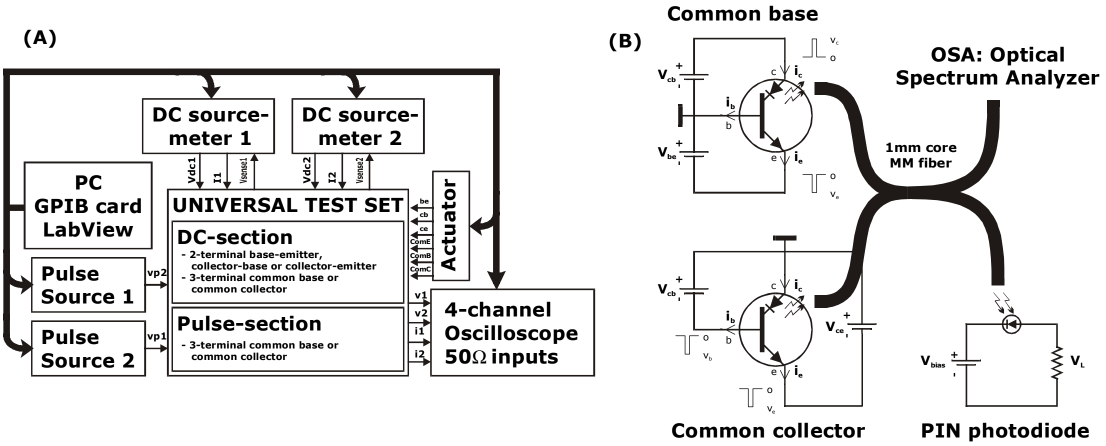

Figure 5.1: Schematic diagram illustrating from left to right the universal test set for DC and pulsed IV measurements (left), common base and common collector configurations (middle) and optical measurement set-up (right)

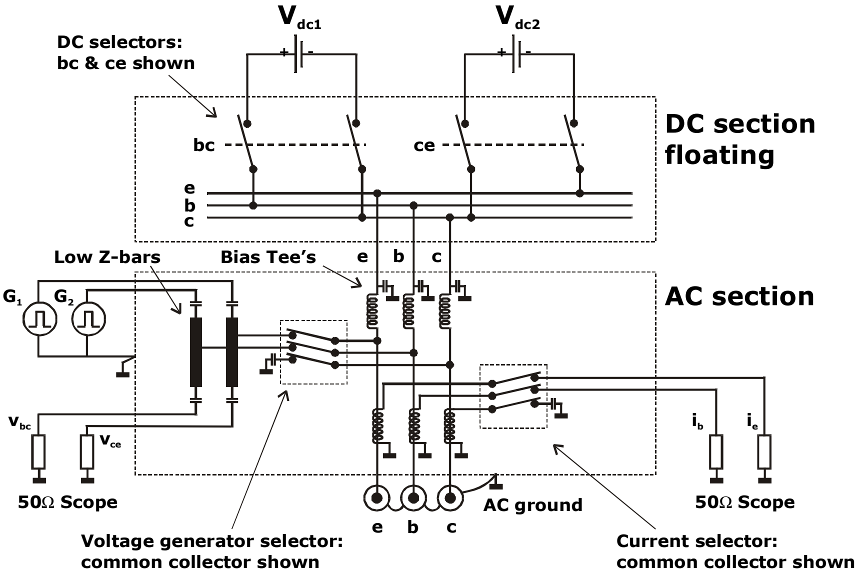

Figure 5.2: Electrical circuit of the universal test set for DC and pulsed IV measurements indicating the mixing of the DC and pulse signals using a bias-T and the switches enabling the various 2-terminal and 3-terminal operating modes [2]

Measurements can be performed at various packaging levels: on bare die (wafer, bar or chip level), on submount (Cu) and at the final package level (TO5). The results that indicate the temperature dependence of the threshold current over a wide range of temperatures (80K to 300K) have been obtained using devices packaged onto a TO5 header and inside a low pressure cryostat, which uses a closed-circuit He pump to cool its chamber and a liquid nitrogen based cold trap to avoid condensation on the transistor-laser. Most of the results have been obtained at bare die level and at room temperature (25ºC). Pulsed excitation is used here to minimize Joule heating, which enables the distinction between carrier heating and lattice heating when interpreting the carrier heating effects. To estimate the remaining amount of Joule heating under pulsed conditions, the heat capacity of the first thermal reservoir, the ridge containing the active region, has to be considered. The specific heat of GaAs is equal to:

$$C_p = 0.33 \text{ J/gK} \qquad 5.1$$

Using a density of 5.32 g/cm^3 and a minimum volume of 1.3x10^{-8} cm^3 (W_b=24µm, L=300µm, d=1.8µm) we obtain the heat capacity of this ridge:

$$C = 2.3\times10^{-8} \text{ J/K} \qquad 5.2$$

Assuming a DC dissipation of 0.5W and a pulse width of 300ns, the temperature increase is equal to 6.5K. This value is acceptable since the variation in power dissipation across one trace of the heating voltage V_{cb} will only be 0.1W and the expected difference in lattice heating will be less than 2K.

The measurements start with low power traces of the 2-terminal current-voltage curves using the voltage controlled DC source. The base-emitter trace will indicate potential problems arising from current leakage within the base-emitter junction region. High values for the base-emitter series resistance indicate serious issues with either or both the emitter and base contact resistances. In most cases the base contact resistance is the real cause of these high series resistance values. The low power transistor measurements are concluded using 3-terminal, common base and common collector, current-voltage tracing using both DC sources. The most common procedure is to control either the emitter current I_e or collector current I_c, and the collector-base heating voltage V_{cb} and it implies switching one DC source to current control and the other DC source to voltage control.

The same procedure, controlling both I_c and V_{cb}, is also used for the higher power pulsed characterization of these devices in such a way that the injection current to the active region is kept constant and the heating voltage V_{cb} is used to induce variable carrier heating inside the active layer. Any variations in the optical behavior are thus more easily linked to the heating voltage and possibly the variable carrier heating. Both pulse sources are voltage controlled. The PC and software are therefore used to measure the collector current I_c and to adjust its value. PID controller loops built into the software stabilize both I_c and V_{cb} simultaneously. The Si PIN photodiode is fast enough to follow the shape of the excitation pulses after a short delay of about 25ns due to the length of the various coaxial cables. The signal level in the optical spectrum analyzer is low however and longer integration times are needed to generate values for the optical spectrum. These integration times result in averaged optical spectra across the full width of the IV pulses, which has to be taken into account when interpreting the results as explained in section 5.4.3.

5.3 Transistor measurements

The transistor measurements are divided into low current DC IV measurements and high injection current pulsed IV measurements. Performing the low current measurements under DC conditions improves the accuracy of the measurements. The high current measurements have to be carried out under pulsed conditions to minimize Joule heating, especially when characterizing devices at bare die level (wafer, bar or chip level).

5.3.1 Low current transistor curves

The low current characterization of the transistor includes both 2-terminal and 3-terminal DC current-voltage measurements. The 2-terminal IV curves deliver insight into the behavior of the two junction regions, namely the emitter-base junction and the collector-base junction region, and the metal-semiconductor interface regions. Typical 2-terminal base-emitter and collector-base IV curves are given in figure 5.3.

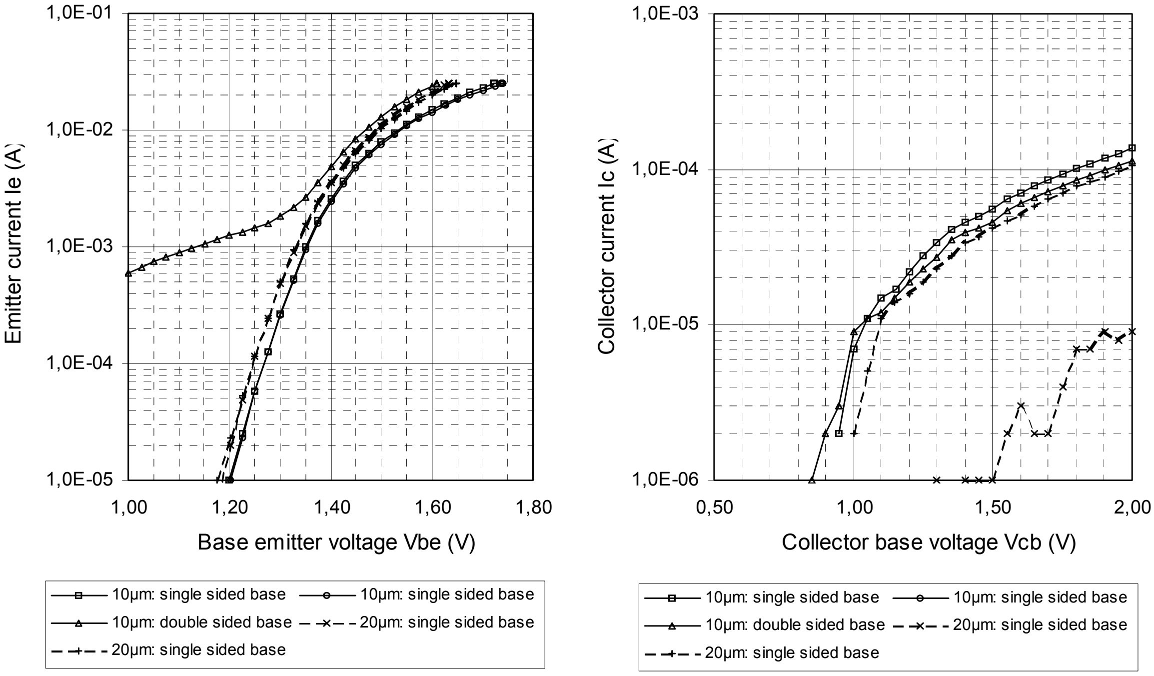

Figure 5.3: *Typical DC 2-terminal base-emitter (left) and collector-base (right) IV curves for different devices on a single bar (T_a=300K, DC, W_e=10μm and 20μm, L_c=300μm, bar level)*

The base-emitter curves scale well, at low forward currents, with the emitter ridge width shown in the legend. They also follow the basic diode equation which is extended here to include the effect of series resistance at higher forward current I_f:

$$I_f = I_0\left(e^{\frac{q(V_f - I_f R_s)}{nkT}} - 1\right) \qquad 5.3$$

Only one device, the 10μm emitter ridge with double sided base contact, deviates from the basic diode behavior by showing a low voltage leakage current path. At lower forward currents the influence of the series resistance is negligible and the natural logarithm of the forward current, $\ln(I_f)$, versus forward voltage curve shows a linear dependency with a slope equal to:

$$\frac{\partial}{\partial V_f}\ln(I_f) = \frac{q}{nkT} \qquad 5.4$$

in which n denotes the ideality factor indicating the dominant type of electron transport across the junction: n=1 for recombination dynamics predominantly inside the neutral regions and n=2 for recombination inside the transition region of the p-n junction. Modern foundries can fabricate diodes with ideality factors smaller than 1.04 at the cost of needing very tight process control. The average base-emitter ideality factor for the devices whose IV curves are shown in figure 5.3 is equal to 1.19. This number indicates the majority of recombination taking place inside the neutral region and normal efficient behavior of the emitter-base junction.

At higher forward currents the influence of the series resistance becomes increasingly important until it dominates the current-voltage behavior above 1000 A/cm^2. The total series resistance can therefore be obtained by determining the high current limit of the base-emitter IV curve's slope:

$$\lim_{I_f \to \infty} \frac{\partial I_f}{\partial V_f} = G = R^{-1} \qquad 5.5$$

The extrapolated values for the base-emitter series resistance are given in figure 5.4 for various emitter ridge widths and cavity lengths.

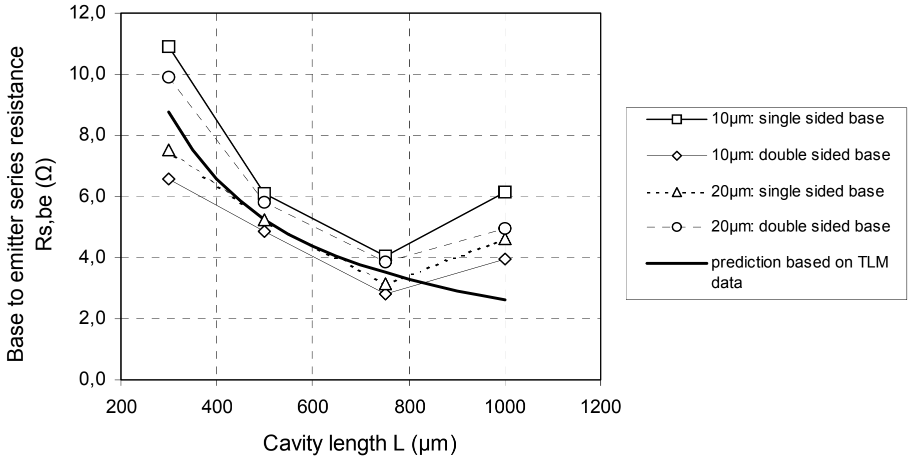

Figure 5.4: *Overview of the base to emitter series resistance as the high current limit of the 2-terminal base-emitter DC IV curve for various emitter ridge widths and cavity lengths (T_a=300K)*

The base resistance determines the amount of internal base potential modulation due to variations in the base current. This base resistance is also expected to be the biggest contribution to the total base-emitter series resistance since the base contact resistance has consistently shown the highest values, due to the limited thickness of its semiconductor contact layer (see section 4.3.4). The base-emitter series resistance values correlate well with cavity length as shown in figure 5.4. The predicted resistance versus cavity length curve is calculated using the measured linear transfer length method (TLM) values for the emitter and base specific contact resistance R_{sp}, the base sheet resistance R_{sh} and transfer length L_t as shown in tables 4.4 and 4.6. The effects of the emitter ridge width and the layout of the base contact seem to be random variations around this curve. The correlation with cavity length remains the strongest. The only exception to this rule is the 1000µm cavity length whose base-emitter series resistance increases again.

Not only base series resistance is important, but also the hole leakage current across the valence band potential barrier between active layer and launcher. This leakage current has only detrimental effects on device behavior. The order of magnitude of this current can be determined from the 2-terminal collector-base DC IV curves, as shown on the right-hand side of figure 5.3. These values are normalized in figure 5.5 by plotting the base current density J_b versus cavity length for the various devices on a single bar indicating the effect of the different ridge widths (see table 4.2). Inserting the n-type doping spike inside the post-launcher, as discussed in section 3.5.1, has succeeded in substantially decreasing the hole leakage across the launcher and into the base. The hole leakage current remains below 1mA even at a heating voltage V_{cb} of 2.0V. The effect of the hole leakage current on the modulation of the internal base potential will therefore remain below 10mV in view of the resistance values shown in figure 5.4.

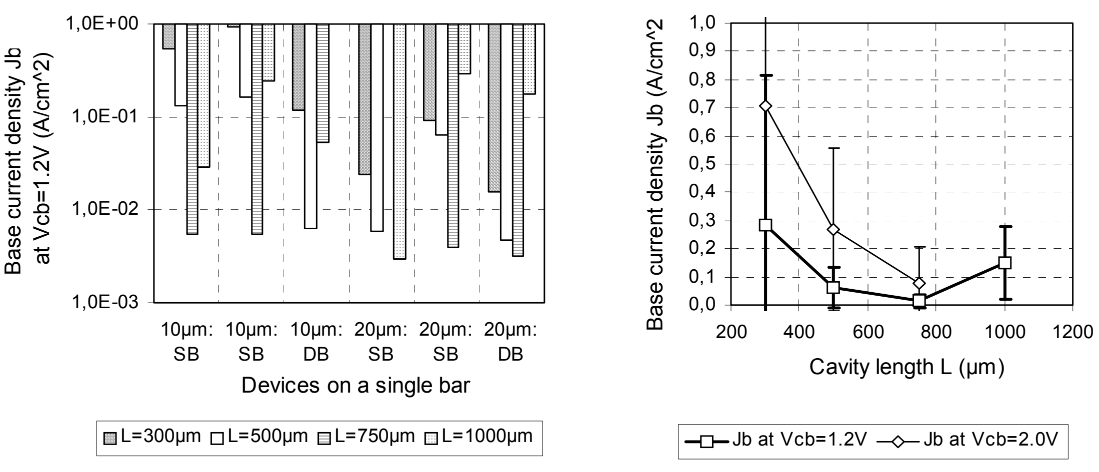

Figure 5.5: *Overview of the base leakage current density J_b at V_{cb}=1.2V versus the different devices on a single bar and for different cavity lengths (left) and overview of the base current density J_b versus cavity length and collector-base voltage V_{cb} (right) (T_a=300K, SB: single-sided base contact, DB: double-sided base contact, error bars indicate one standard deviation)*

Typical DC 3-terminal common base IV curves, in which the emitter current is kept constant at different values and the heating voltage V_{cb} is varied, are shown in figure 5.6 and indicate correct transistor behavior. The first sharp decrease in V_{be} is due to the strong reduction in base current I_b which works against the external base potential. The external base-emitter voltage required to keep the emitter current constant therefore decreases sharply with the decrease in base current I_b, as shown in the bottom left and upper right plots of figure 5.6. The base current decreases in magnitude and stabilizes at heating voltages of 0.5V and higher but does not approach zero due to recombination of electrons inside the base. Using the following definitions, the base to collector current amplification factor β and the current transfer ratio α are plotted in figure 5.7

$$\alpha = \frac{\partial I_c}{\partial I_e} \qquad 5.6$$

$$\beta = \frac{\partial I_c}{\partial I_b} \qquad 5.7$$

The full overview of the base to collector current amplification factor β at various heating voltages V_{cb} is given in figure 5.8. These values for the long elongated transistor-laser are substantially lower than the current amplification factors of normal, small footprint, transistors. Standard GaAs heterojunction bipolar transistors with $Al_{0.25}Ga_{0.75}As$ emitters show current gains ranging from 50 to 100 at collector current densities between 1 and 5 kA/cm^2. One remaining question is the effect of the p-type δ-doping inside the base on the current gain. The

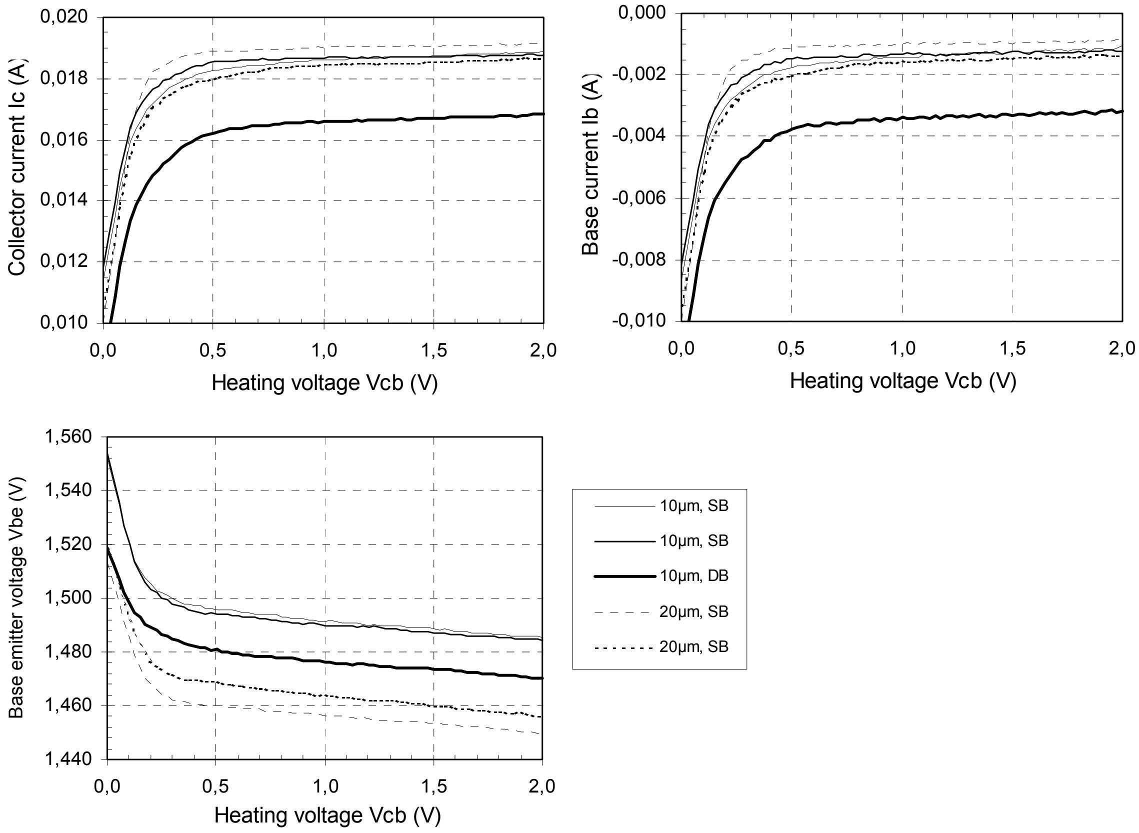

Figure 5.6: *Typical DC 3-terminal common base IV curves for the various devices on a single bar: collector current I_c (upper left), base current I_b (upper right) and required base-emitter voltage V_{be} (lower left) versus heating voltage V_{cb} (I_e=20mA, T_a=300K, L=300µm, SB: single-sided base contact, DB: double-sided base contact)*

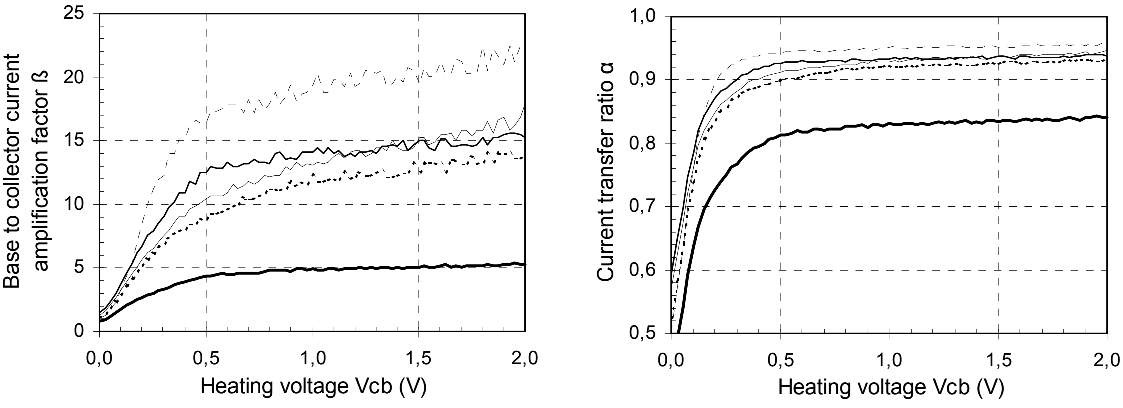

Figure 5.7: *Typical values for the base to collector current amplification factor β (left) and current transfer ratio α (right) for the various devices on a single bar (I_e=20mA, T_a=300K, DC, L=300µm, for legend see figure 5.6)*

sudden increase in β at a heating voltage of 2.0V and a cavity length of 300µm is due to the leakage current driving I_b even closer to zero and as such causing an artificial increase in the current amplification factor.

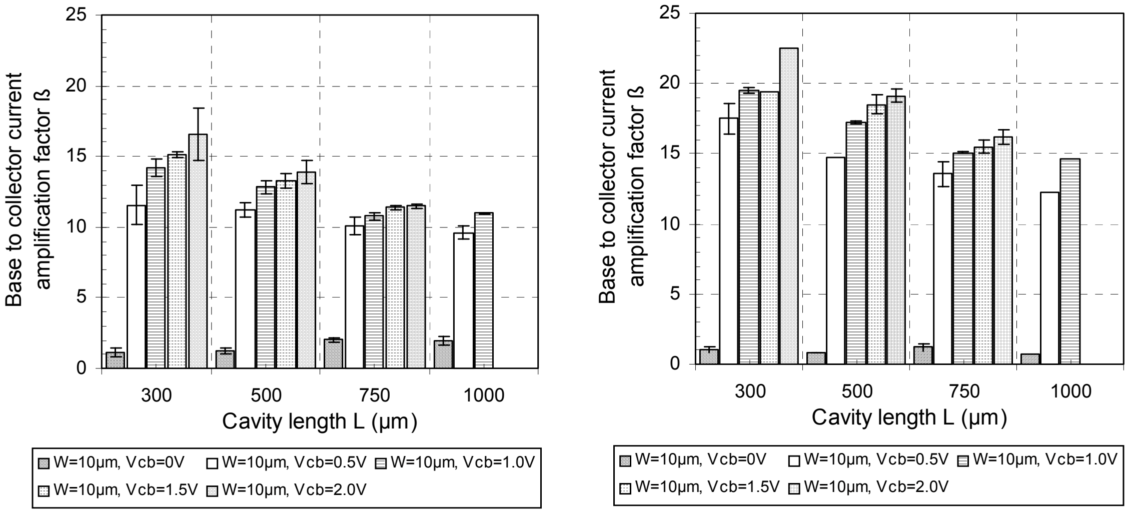

Figure 5.8: *Overview of the DC base to collector current amplification factor* β *versus cavity length and heating voltage* V_{cb} *for an emitter ridge width of 10µm (left) and 20µm (right) (*T_a*=300K,* I_e*=20mA)*

5.3.2 High current transistor curves

The high current characterization of the transistor involves pulsed current-voltage measurements using the 3-terminal common collector configuration. These results indicate the actual IV performance under normal operating conditions near the laser’s threshold conditions. Under normal operating conditions, the collector current I_c, the actual injection current to the active layer, is kept constant while the heating voltage V_{cb}, the actual measure for the electric field across the launcher, is varied to modulate the optical intensity. The common collector configuration is used due to the layout of both the interconnect pads on the device and the coplanar probes used for these measurements (see figure 3.27). Both outside tips on the 3-tip probes correspond to the collector pads on the device and are forced to common by the universal IV test set. Typical common collector IV curves are given in figure 5.9 for a device with a 10µm wide emitter ridge and a 300µm long cavity.

An external collector-base voltage of 0.5V is needed to lower the conduction band (CB) barrier between the base and the launcher and for the base current to reach small and relative constant values. For external heating voltages between 0V and 0.5V, substantial base currents are flowing through both the base layer and the base contact and their contributions have to be taken into account. The effect of the base contact resistance, as estimated in figure 5.4, is a more negative internal base potential as compared to the external base potential in case of these negative base currents due to recombination of the electrons inside the base. Another effect which alters the average internal base potential is the hole leakage current across the launcher and into the base, but it has been substantially reduced here and can be neglected. Only in the case of the shortest and narrowest device at V_{cb}=2.0V does the total base current approach zero due to the above mentioned hole leakage current. Assuming a base contact resistance of 7Ω, the common collector pulsed IV curves of figure 5.9 can be redrawn versus the average internal base potential as shown in figure 5.10.

The effect of the base layer itself, i.e. the base sheet resistance, is a non-uniform internal base potential across the width of the emitter ridge and therefore inhomogeneous injection and

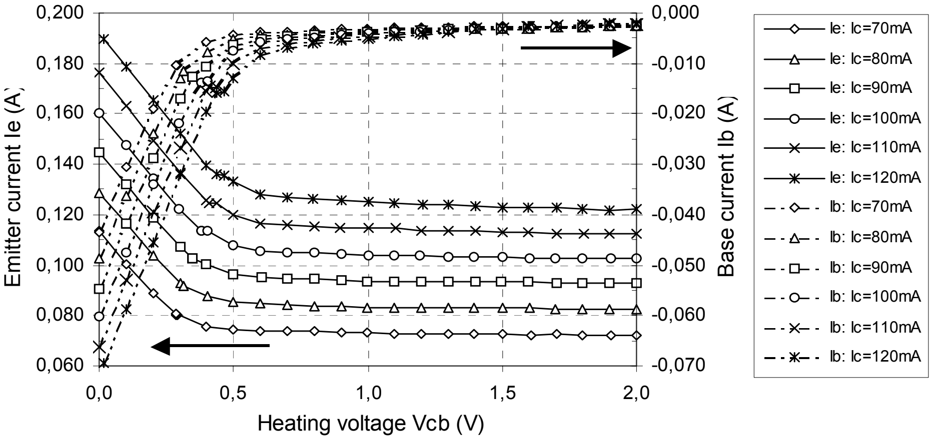

Figure 5.9: *Typical common collector pulsed IV curves indicating the emitter and base currents versus heating voltage V_{cb} at different constant collector currents I_c (T_a=300K, pulsed, t_p=300ns, duty cycle=0.7%, W_e=10μm, L_c=300μm)*

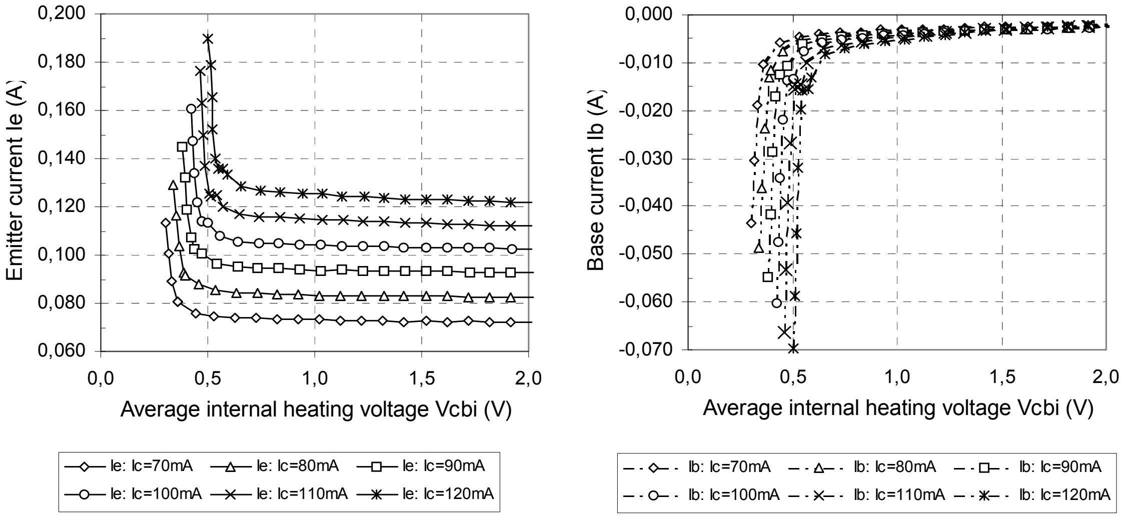

Figure 5.10: *Typical common collector pulsed IV curves indicating the emitter and base currents versus the average internal collector-base voltage V_{cbi} at different constant collector currents I_c (T_a=300K, pulsed, t_p=300ns, duty cycle=0.7%, W_e=10μm, L_c=300μm)*

carrier heating in the lateral direction. Table 5.1 shows the influence of the base layer as resistance values for the base layer from the left-hand or the right-hand side of the emitter ridge to the left-hand side of the base contact. As a result, the emphasis from here onwards will be on the range of heating voltages above 0.5V, where the term heating voltage V_{cb} still denotes the externally applied voltage. Note that part of the inhomogeneous injection and carrier heating will be reduced inside the active layer through the high mobility of the electrons and fast electron-electron interactions.

The 3-terminal common-collector pulsed IV values for the base to collector amplification factor β and current transfer ratio α are given in figure 5.11. From the point of view of transistor

Table 5.1: *Base layer resistance values for the current path from the left-hand and right-hand side of the emitter ridge to the left-hand side of the base contact metal ($W_e=10\mu m$, $R_{sh}=727\Omega/sq$)*

Cavity length L (µm)	R_{left} (Ω)	R_{right} (Ω)
300	23.0	3.6
500	13.8	2.2
750	9.2	1.5
1000	6.9	1.1

behavior and current amplification, only the range of heating voltages between 0.5V and 1.2V is stable. At higher collector-base voltages, small changes in hole leakage current on top of the small absolute base current cause large variations in the base to collector current amplification factor. The fact that the absolute values of the base currents remain low here is also the reason why the hot electron injection laser can still be operated across the full range of heating voltages between 0.5 and 2.0V. The strong variations in β do not significantly affect the device modulation through the heating voltage V_{cb}.

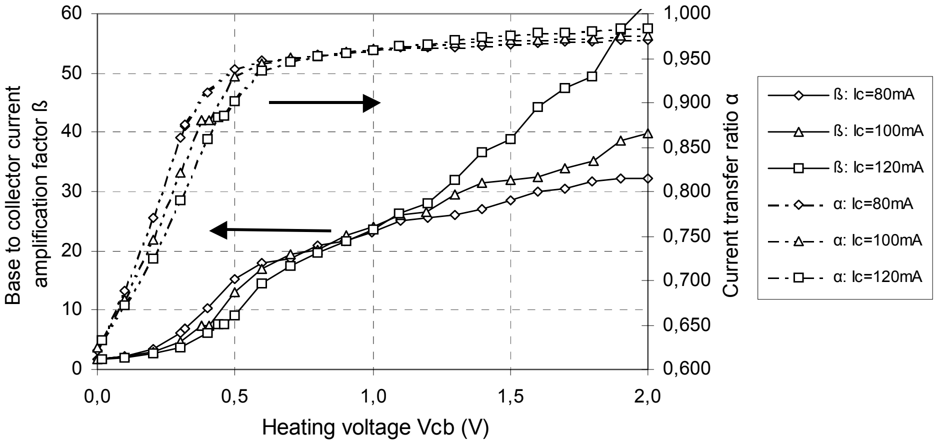

Figure 5.11: *Pulsed common-collector measurement of the base to collector current amplification factor β and current transfer ratio α versus the heating voltage V_{cb} at different constant collector currents I_c ($T_a=300K$, pulsed, $t_p=300ns$, duty cycle=0.7%, $W_e=10\mu m$, $L_c=300\mu m$)*

5.4 Optical measurements

The purpose of the optical measurements is to characterize the optical behavior of the transistor-laser and to obtain that set of data which can be used to estimate the carrier heating efficiency. This set of data includes the light output versus injection current I_c, heating voltage V_{cb} and ambient temperature T_a. Various optical spectra are also shown here but their contribution remains indicative.

5.4.1 Light output versus injection current and heating voltage

Typical curves for the optical output power versus the heating voltage V_{cb} at different constant injection currents I_c are shown in figure 5.12. The linear fit of each L-I curve above threshold is also plotted in the same figure. The crossing of each linear regression with the current axis is defined here as the threshold current at that given heating voltage V_{cb}. The slope of the L-I curve is defined as the relative external quantum efficiency (EQE). Two effects of increasing the heating voltage which are immediately visible are the steady increase in threshold current and the steady decrease in the slope of the L-I curve and thus the decrease in external quantum efficiency. Figure 5.12 also indicates that the heating voltage is still able to suppress lasing as long as the injection current remains below 100mA. At higher injection currents, the heating voltage is still able to decrease the optical output power but unable to suppress lasing all together. The shapes of the increase in threshold current and the decrease in the slope of the L-I curve versus the heating voltage are shown in figure 5.13.

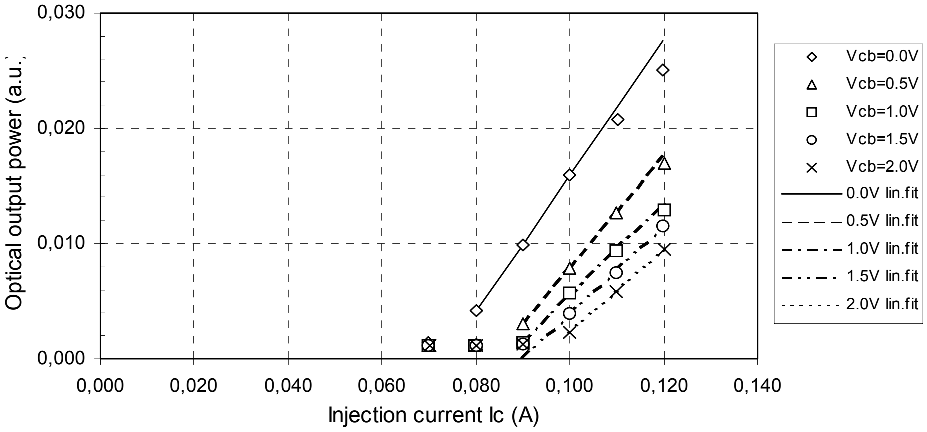

Figure 5.12: *Pulsed measurement results for the optical power L versus injection current I_c for different heating voltages V_{cb} (T_a=300K, pulsed, t_p=300ns, duty cycle=0.7%, W_e=10μm, L_c=300μm)*

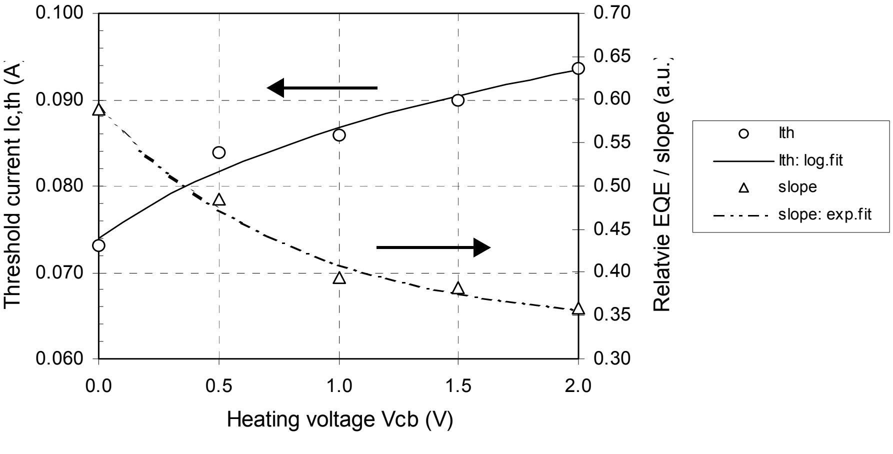

Figure 5.13: *Threshold current I_{th} and slope of the L-I curve versus heating voltage V_{cb} (T_a=300K, pulsed, t_p=300ns, duty cycle=0.7%, W_e=10μm, L_c=300μm)*

As a first indication of the effectiveness of the heating voltage, the modulation depth is defined here as the ratio of both optical output powers at the minimum and maximum heating voltage and at a constant injection current I_c. The modulation depths derived from the L-I curves, as shown in figure 5.14, include the spontaneous emission (SE) on both side of the lasing peak. WDM systems filter out the spontaneous emission and actually reduce the optical channel width to its absolute minimum. Optical spectra actually indicate possible modulation of the lasing signal itself as high as 20dB.

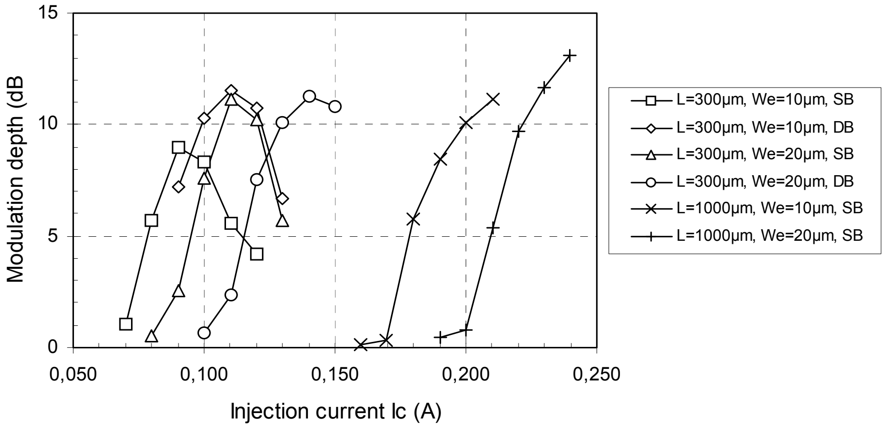

Figure 5.14: *Modulation depth of the optical power versus collector current I_c for heating voltages V_{cb} between 0V and 2V (T_a=300K, pulsed, t_p=300ns, duty cycle=0.7%, SB: single-sided base contact, DB: double-sided base contact)*

The 1000µm long cavities show the greatest modulation depths. Their effectiveness, as compared to the 300µm cavities, will become apparent towards the end of this chapter. The above procedure of obtaining the threshold current density can be applied across a wide range of device designs and cavity lengths. The overview of the threshold current density versus heating voltage V_{cb} for the different device designs and cavity lengths is given in figure 5.15.

All curves show the strongest increase in threshold current density between the heating voltages of 0V and 0.5V and increase with a relative constant slope at higher heating voltages. Increasing the emitter ridge width to 20µm and increasing the cavity length to 1000µm both result in strongly reduced threshold current densities due to reduced internal and mirror losses respectively. Figure 5.15 also indicates that switching from a single-sided base contact to a double-sided base contact substantially increases the threshold current density again. In standard ridge waveguide lasers, a substantial part of the decrease in threshold current density between a ridge width of 10µm and 20µm can be contributed to the wider ridge itself [5] due to current spreading and lateral carrier diffusion. In our case the ratio W_e/W_b also influences the threshold current density and is equal to 42% for the 10µm ridge and 59% for the 20µm ridge (table 3.4).

5.4.2 Light output versus temperature

The temperature dependence of the threshold current density has also been determined for those devices which were mounted onto a TO5 header using EPO-TEK and could subsequently be characterized inside the cryostat. This cryostat has a transparent glass cover which allows direct measurement of the laser's optical properties by aligning either the 1mm core optical fiber or

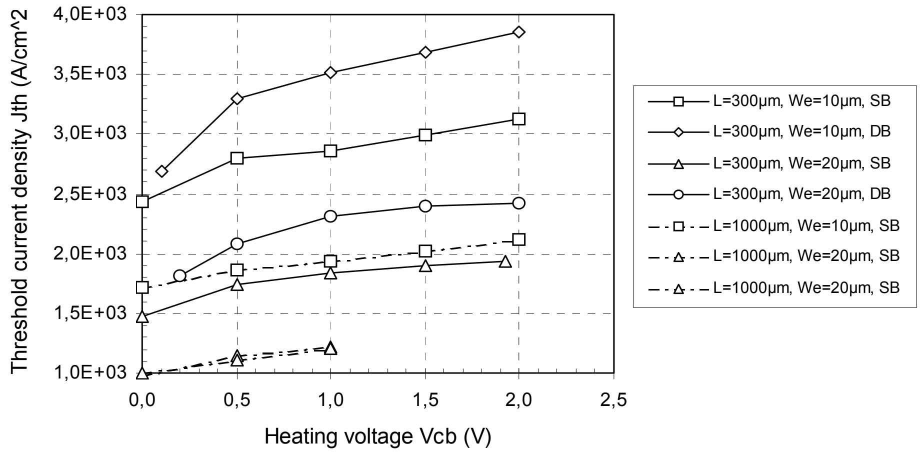

Figure 5.15: *Overview of the threshold current density versus heating voltages V_{cb} for different device designs and cavity lengths (T_a=300K, pulsed, t_p=300ns, duty cycle=0.7%, SB: single-sided base contact, DB: double-sided base contact)*

the PIN photodiode in front of it. Figure 5.16 shows the light output versus injection current I_c curves at different heating voltages V_{cb} and ambient temperatures T_a.

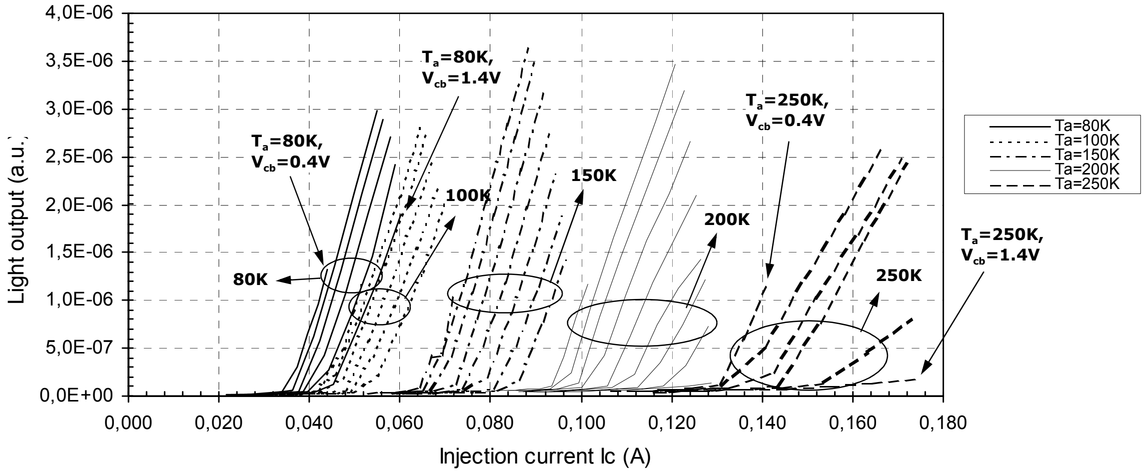

Figure 5.16: *Light output versus injection current I_c at different heating voltages V_{cb} and ambient temperatures T_a (DC, on TO5 header inside cryostat, W_e=10µm, L=500µm, single-sided base contact, V_{cb} in steps of 0.2V,*
V_{cb} from 0.4V to 1.4V for 80K/100K/250K,
V_{cb} from 0.4V to 1.8V for 150K,
V_{cb} from 0.4V to 2.0V for 200K)

The curves follow the same trend as in figure 5.12 in that increasing the heating voltage at each temperature setting also increases the threshold current and decreases the slope of the L-I curve above threshold. At the highest heating voltage at each temperature setting, the curves actually approach the curves of the next temperature setting at the lowest heating voltage (V_{cb}=0.4V). An effective carrier temperature increase in the order of 25K seems therefore feasible at lower ambient temperatures and approximately 40K at higher ambient temperatures. Figure 5.17 shows the temperature dependence of the threshold current density over a wide range of temperatures between 80K and 250K for both 10µm and 20µm emitter ridge widths.

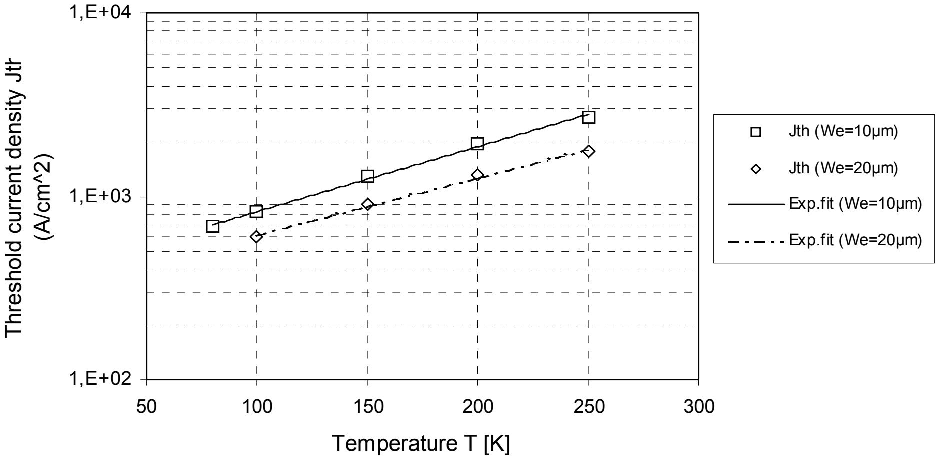

Figure 5.17: Measured threshold current density versus temperature and exponential fit to obtain T_0 (DC, on TO5 header inside cryostat, L=500µm, single-sided base contact, V_{cb}=0.4V)

These values for the threshold current density are higher than the values stated in figure 5.15 since they are extracted from DC measurements at a heating voltage V_{cb} equal to 0.4V. The higher junction and carrier temperatures are reflected in higher threshold current densities. The measured data is also fitted to the following exponential correlation between threshold current density and temperature:

$$J_{th} = J_{th,T_0} e^{T/T_0} \tag{5.8}$$

where J_{th,T_0} denotes a constant and T_0 the characteristic temperature of the laser. T_0 describes the temperature sensitivity of the threshold current density and typical values for GaAs bulk active layers fall between 120K and 200K near room temperature [3]. GaAs quantum-well (QW) lasers exhibit a much smaller temperature dependence due to their reduced dependence of the quasi-Fermi energies on the device temperature. Their characteristic temperatures typically range from 250K to 400K near room temperature [3]. T_0 tends not to be constant across the full temperature range. It actually increases towards higher temperatures. The current implementation of the hot electron injection laser utilizes a GaAs bulk active layer as explained in section 3.6. Its characteristic temperatures, fitted between 200K and 300K, are given in table 5.2.

Table 5.2: Actual values for the characteristic temperature of the current hot electron injection laser, fitted between 200K and 300K (L=500µm, single-sided base contact)

Emitter ridge width W_e	Characteristic temperature T_0
10µm	147K
20µm	169K

These are reasonable values for a newly designed fully integrated transistor-laser based on a GaAs bulk active layer. These values for the laser's characteristic temperature can now be used to estimate the carrier heating efficiency of the current hot electron injection laser, as explained in section 5.5.

5.4.3 Optical spectra

The optical spectra have the potential of giving direct insight into the carrier energy distribution through the spontaneous emission, of which the short-wavelength tail, according to the Maxwell-Boltzmann distribution, is directly proportional to [4]

$$L_{se}(\bar{h}\omega) \propto e^{\frac{-\bar{h}\omega}{kT_e}} \qquad 5.9$$

where L_{se} is the spontaneous emission intensity, $\bar{h}\omega$ the energy of the emitted photon and T_e the effective carrier temperature. The effective temperature of the carriers can therefore be estimated from the slope of the high energy, short wavelength, tail of the spontaneous emission curve where the exclusion of variations in the density of states generates an error of about 10%. Fully thermalized carrier distributions are assumed here through very fast carrier-carrier interactions on the order of 300fs.

$$\frac{\partial}{\partial \bar{h}\omega}\ln(L_{se}) = -\frac{1}{kT_e} \qquad 5.10$$

$$T_e = -\frac{1}{k\frac{\partial}{\partial \bar{h}\omega}\ln(L_{se})} \qquad 5.11$$

The pulsed optical spectra at bar level are shown in figure 5.18 versus the heating voltage V_{cb} and at three different injection currents I_c for a 10µm emitter ridge width, 300µm cavity length, and single-sided base contact.

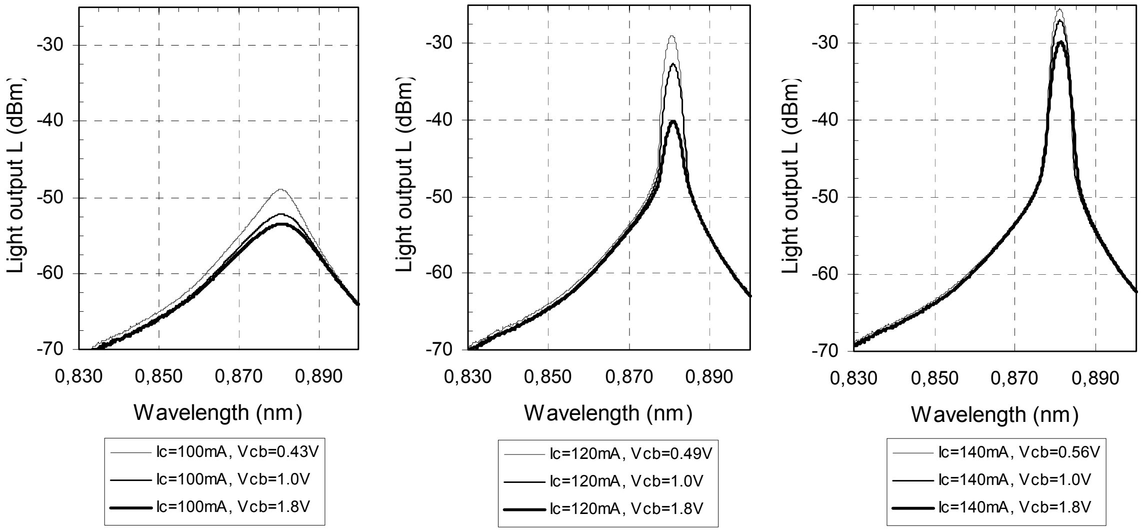

Figure 5.18: *Optical spectrum versus heating voltage* V_{cb} *at three different injection currents* I_c*: 100mA (left), 120mA (middle), and 140mA (right) (*T_a*=300K, pulsed,* t_p*=300ns, duty cycle=0.7%, bar level,* W_e*=10µm,* L_c*=300µm)*

The left-hand graph shows the influence of the heating voltage on the optical spectrum below threshold while the middle and right graphs indicate the situation above threshold. At 120mA, the curves indicate a modulation depth of the lasing peak equal to 11dB which decreases to 5dB at 140mA. Again, in good agreement with figure 5.14.

Figure 5.19 shows the pulsed optical spectra under similar conditions but for a 20µm emitter ridge width and at one constant injection current I_c equal to 130mA.

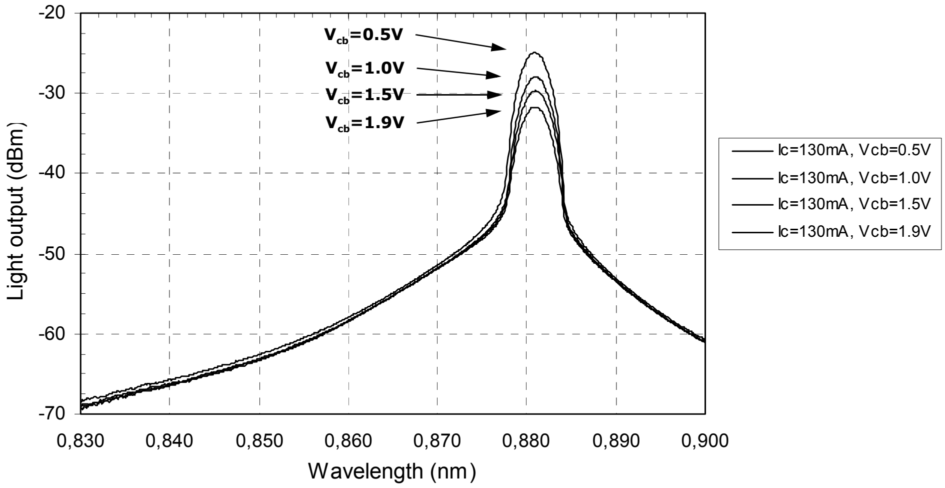

Figure 5.19: *Optical spectrum versus heating voltage V_{cb} at a constant injection current I_c equal to 130mA (T_a=300K, pulsed, t_p=300ns, duty cycle=0.7%, bar level, W_e=20µm, L_c=300µm)*

The corresponding current-voltage data is given in table 5.3.

Table 5.3: *IV data corresponding to the optical spectra as shown in figure 5.19 (T_a=300K, pulsed, t_p=300ns, duty cycle=0.7%, bar level, W_e=20µm, L_c=300µm)*

Heating voltage V_{cb} (V)	**V_{be} (V)**	**I_e (A)**	**I_c (A)**	**$P_{DC,tot}$ (W)**	**$P_{pulse,avg}$ (W)**
0.5	2.16	0.147	0.130	0.379	0.0027
1.0	1.99	0.133	0.130	0.394	0.0028
1.5	1.93	0.131	0.130	0.448	0.0031
1.9	1.92	0.131	0.130	0.498	0.0035

The consumed electrical power in pulsed mode is low and constant between curves at an average of 3mW. At this current the modulation depth has gone down from its peak value of about 7dB.

An example of the DC optical spectrum versus heating voltage V_{cb} at TO5 header level and at 200K ambient temperature inside the cryostat is shown in figure 5.20 for a 20µm emitter ridge width, 500µm cavity length and single-sided base contact. The corresponding current-voltage data is given in table 5.4. The totally consumed electric power is substantially higher but still fairly constant between the first three curves, V_{cb}=0.5, 0.7, and 1.0V, in the range of 390mW to 410mW. The corresponding modulation depth is equal to 8dB for a variation in heating voltage

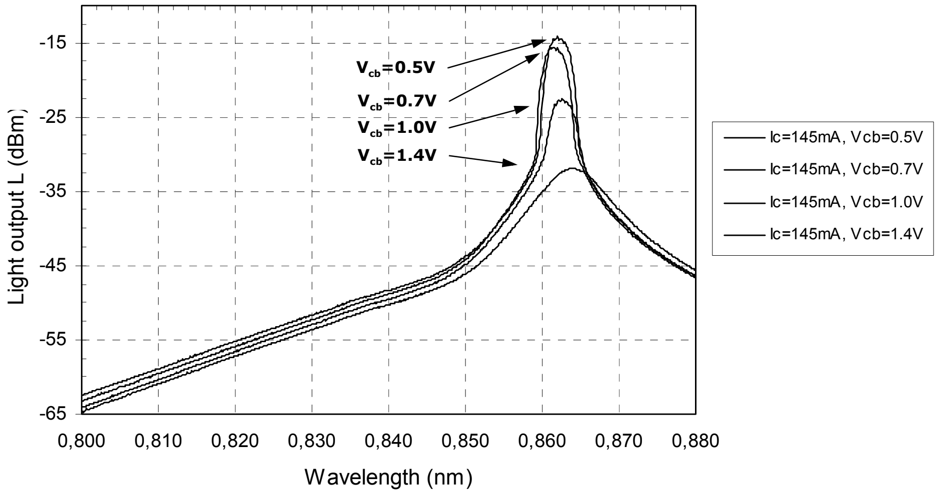

Figure 5.20: *Optical spectrum versus heating voltage V_{cb} at a constant injection current I_c equal to 145mA (DC, on a TO5 header inside the cryostat, T_a=200K, W_e=20μm, L_c=500μm)*

Table 5.4: *IV data corresponding to the optical spectra as shown in figure 5.20 (DC, on a TO5 header inside the cryostat, T_a=200K, W_e=20μm, L_c=500μm)*

Heating voltage V_{cb} (V)	**V_{be} (V)**	**I_e (A)**	**I_c (A)**	**$P_{DC,tot}$ (W)**
0.5	1.89	0.180	0.145	0.41
0.7	1.81	0.160	0.145	0.39
1.0	1.77	0.150	0.145	0.41
1.4	1.76	0.150	0.145	0.47

from 0.5V to 1.0V and equal to 17dB from 0.5V to 1.4V. Note that the consumed electrical power increases from 410mW to 470mW between the heating voltages of 1.0V and 1.4V.

None of the spectra show strong indications of a blue shift of the emission peak and a decreased slope of the high energy tail of the spontaneous emission, which are normally associated with an increased effective carrier temperature inside the active layer. Only the lasing peak in figure 5.20 shows a slight blue shift going from a heating voltage of 0.5V to 0.7V. It is difficult to obtain a clear picture with the lasing peak being an ensemble of competing longitudinal modes.

5.5 Carrier heating efficiency

The preferred method to study the carrier heating effects in this laser structure is time-resolved observation of its photoluminescence and electroluminescence spectra. The time-resolved feature is required to distinguish between carrier heating and lattice heating effects by minimizing the Joule heating of the device. Ideal would be the detection of the energy spectrum of the injected carriers themselves to investigate the ability of the device to tune the energy of these carriers. Intrinsic carrier dynamics are difficult to measure directly and usually require specific test structures containing only a subset of the features of the transistor-laser. This project has focussed on the successful vertical integration of the transistor and the laser for complementary modulation of injection current and carrier temperature, not on specific test structures to measure carrier heating efficiencies since the concept of carrier heating assisted gain switching had already been demonstrated before, both in theory and through experiments.

Another option to study the internal processes is to determine the frequency response of the laser's optical output power at different levels of carrier injection and carrier heating. Both these processes have their own characteristic frequency response [1]. Pure carrier injection modulation suffers from the electron-photon resonance, also known as relaxation oscillation, which exhibits itself as a resonance peak in the laser's frequency response as explained in chapter 2. In case of pure carrier temperature modulation, this peak is even more pronounced as compared to the case of pure carrier injection modulation. The ideal mix of carrier injection and carrier temperature modulation eliminates these relaxation oscillations and therefore the wavelength chirp [1]. The laser's frequency response will decrease with $1/\omega$, instead of $1/\omega^2$ in case of pure carrier injection modulation, enabling higher, chirp free, modulation frequencies [1]. However, these measurements are very extensive and fall outside the scope of this thesis.

Measured values for the characteristic temperature, as given in table 5.2, combined with the curves for threshold current density versus heating voltage V_{cb}, as shown in figure 5.15, can also be used to estimate the carrier heating efficiency. Taking the ratio of two threshold current densities $J_{th,1}$ and $J_{th,2}$ at temperatures T_1 and T_2, equation 5.8 yields:

$$\frac{J_{th,2}}{J_{th,1}} = e^{(T_2 - T_1)/T_0} \qquad 5.12$$

Rewriting equation 5.12 give us the change in temperature.

$$\Delta T = T_2 - T_1 = T_0 \ln\frac{J_{th,2}}{J_{th,1}} \qquad 5.13$$

Equation 5.13 is used to estimate the change in carrier temperature due to the heating voltage V_{cb} by converting the $\frac{\Delta J_{th}}{\Delta V_{cb}}$ data of figure 5.15 into $\frac{\Delta T_e}{\Delta V_{cb}}$ data as shown in figure 5.21.

The strongest increase in carrier temperature, based on variations in the threshold current density, is visible between 0 and 0.5V. The slope of carrier temperature versus heating voltage curve is relatively constant afterwards. The total increase in carrier temperature due to the heating voltage V_{cb} varies from 30 to 50K and is in good agreement with the temperature variations that can be inferred from figure 5.16.

Another way to approach the carrier heating efficiency is by starting with the expression for threshold modal gain and combining it with the threshold current density versus cavity length data:

$$\Gamma g_{mat} = g_{mod} = g_{net} + \alpha_i = \frac{1}{2L}\ln\frac{1}{R_1 R_2} + \alpha_i \qquad 5.14$$

in which Γ is the confinement factor, g_{mat} the material gain, g_{mod} the modal gain, g_{net} the net modal gain, α_i the internal cavity losses, L the cavity length, and R_1 and R_2 the reflectivities of both cleaved facets. Any change in cavity length will directly result in a change in the required

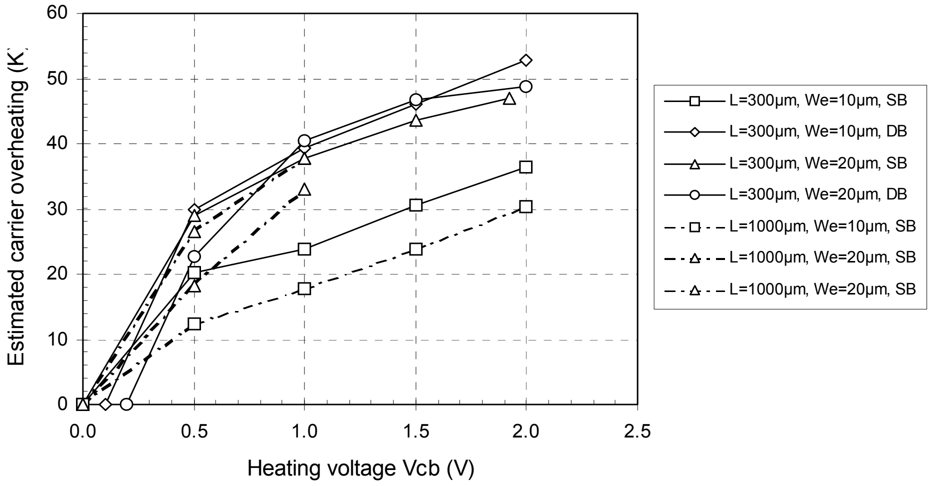

Figure 5.21: *Overview of the calculated carrier overheating versus heating voltage V_{cb} for different device designs and cavity lengths (all curves normalized to T_e=300K at V_{cb}=0V)*

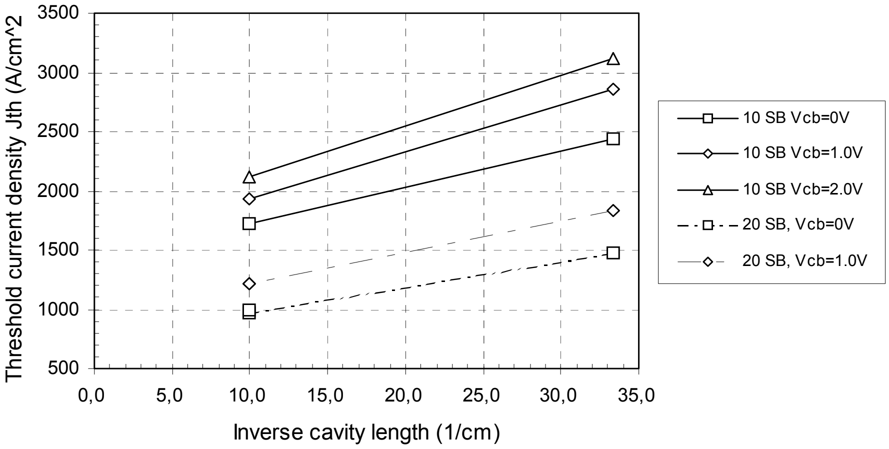

Figure 5.22: *Overview of the threshold current density versus inverse cavity length*

net gain. The derivative of the relation between net gain and inverse cavity length takes the form:

$$\frac{\partial g_{net}}{\partial(1/L)} = \frac{1}{2}\ln\frac{1}{R_1R_2} = \ln\frac{1}{R}\bigg|_{R_1 = R_2 = R} \qquad 5.15$$

We can derive the following expression for the change in net gain versus the change in heating voltage V_{cb}:

$$\frac{\partial g_{net}}{\partial V_{cb}} = \frac{\partial g_{net}}{\partial J_{th}}\frac{\partial J_{th}}{\partial V_{cb}} = \frac{\partial g_{net}}{\partial(1/L)}\left(\frac{\partial J_{th}}{\partial(1/L)}\right)^{-1}\frac{\partial J_{th}}{\partial V_{cb}} \qquad 5.16$$

which, using equation 5.15 becomes

$$\frac{\partial g_{net}}{\partial V_{cb}} = \ln\frac{1}{R}\left(\frac{\partial J_{th}}{\partial(1/L)}\right)^{-1}\frac{\partial J_{th}}{\partial V_{cb}} \qquad 5.17$$

The first factor is easily calculated using a default reflectivity for cleaved facets equal to 0.32. The data for the second part is given in figure 5.22 while the data for the third part is given in figure 5.15. Multiplied, these numbers yield the curves shown in figure 5.23, which indicates the resulting change in net gain at a certain heating voltage V_{cb}.

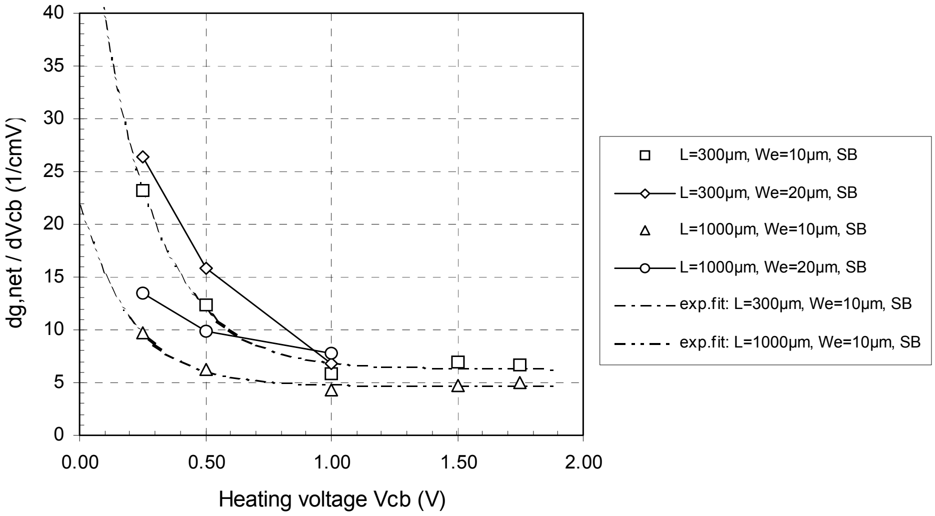

Figure 5.23: *Calculated values of the resulting change in net gain versus heating voltage V_{cb} (SB: single-sided base)*

Again, the range of heating voltages between 0V and 0.5V is a region with strong lateral inhomogeneity due to substantial base currents and non-zero base resistance. Focussing on the range of heating voltages greater than 0.5V, the $\frac{\partial g_{net}}{\partial V_{cb}}$ curves seem to level off at 7 cm^{-1} and 5 cm^{-1} per volt heating voltage V_{cb} for the 300µm and the 1000µm cavity lengths respectively. To investigate the relative change in net gain, the mirror losses need to be calculated. Table 5.5 shows these values and indicates the relative change in net gain per volt heating voltage V_{cb} to be 18% and 44% for the 300µm and the 1000µm cavity lengths respectively. The relative change in net gain is higher for the longer laser due to the lower mirror losses.

Table 5.5: *Estimated relative change in net modal gain per volt heating voltage V_{cb} for the 300µm and 1000µm cavity lengths*

Cavity length L (µm)	dg_{net}/dV_{cb} (cm^{-1}V^{-1})	α_{mirror} (cm^{-1})	dg_{mod} (%)
300	-6.8	38.0	18%
1000	-5.0	11.4	44%

References

[1] V. Gorfinkel and S. Luryi, “High-frequency modulation and suppression of chirp in semiconductor lasers,” *Applied Physics Letters*, vol. 62, pp. 2923-2925, 1993.

[2] J.J.M. Kwaspen, R.C.P. Hoskens, B. Jacobs and M.C.J.C.M. Krämer, “A Universal Test Set for DC and Pulsed I-V Characterization of Various Semiconductor Devices,” *Proc. GAAS 2002*, 23-27 september 2002, Milano.

[3] G.P. Agrawal and N.K. Dutta, *Semiconductor lasers*, Kluwer Academic Publishers, 1993.

[4] N. Balkan, *Hot electrons in semiconductors. Physics and devices,* Oxford University Press, 1998.

[5] H.C. Casey and M.B. Panish, *Heterostructure lasers. Part B: materials and operating characteristics*, Academic Press, 1978

Chapter 6

Discussion and recommendations

THE MEASUREMENT RESULTS OF THE PREVIOUS CHAPTER INDICATE A CERTAIN LEVEL OF HEATING VOLTAGE INDUCED GAIN SWITCHING TO BE PRESENT. IT'S IMPORTANT TO DISCUSS HERE THE POSSIBLE EFFECTS ON WHICH THAT GAIN SWITCHING COULD BE BASED AND TO GIVE ESTIMATES FOR THEIR RELATIVE CONTRIBUTIONS. POSSIBLE CANDIDATES ARE: THE ELECTRO-OPTIC OR POCKELS EFFECT, THE FRANZ-KELDYSH EFFECT AND THE CARRIER-HEATING EFFECT. ASSUMING A SMALLER THAN EXPECTED AMOUNT OF CARRIER-HEATING INDUCED GAIN SWITCHING, IT IS ALSO IMPORTANT TO IDENTIFY THE AREAS OF POSSIBLE IMPROVEMENTS.

6.1 Heating voltage induced gain switching

The previous chapter concluded by stating the change in net gain per volt V_{cb} (see table 5.5):

$$\frac{\partial g_{net}}{\partial V_{cb}} = \text{-6.8 to -5.0 cm}^{-1}\text{/V} \qquad 6.1$$

Net gain is defined as the threshold gain minus the internal losses. The equations used to obtain these results assume the internal losses to be constant. Figures 5.12, 5.13, and 5.16 not only show an increase in the threshold current with the heating voltage V_{cb} but also clearly indicate a decrease in the external quantum efficiency with the same heating voltage. The external quantum efficiency is defined by equation 3.28 as the product of the internal quantum efficiency, meaning the ratio of radiative recombination to the total recombination, and the ratio of the mirror losses to the total optical losses. We believe the internal quantum efficiency to decrease with V_{cb} and the internal losses to remain relatively constant due to (1) higher levels of non-radiative recombination processes at higher energy levels inside the L and X subvalleys, and (2) an increase in electron leakage into the pre-cladding region with subsequent non-radiative recombination or radiative recombination outside the measured spectral range.

6.2 Different contributions to the gain switching and their estimates

6.2.1 High electric field effects

The Lastip simulations of figures 3.21 and 3.25, without the carrier-heating effect taken into account, indicate stable lasing with constant light output levels versus the heating voltage V_{cb} at a constant injection current I_e or I_c. The measurements on the other hand do show a modulation of the lasing output versus the heating voltage V_{cb}. The biggest differences between the simulation and the real device are the possible effects that the high transverse electric field across the launcher has on the optical mode: the electro-optic or Pockels effect, the Frans-Keldysh effect and the carrier-heating effect.

6.2.2 The electro-optic or Pockels effect

The linear electro-optic or Pockels effect is based on the introduction of birefringence in a crystal when exposed to a high intensity electric field [1]. The isotropic circular indicatrix in the absence of an electric field becomes anisotropic elliptical in the presence of a high electric field with a change in the refractive index as the result [1]:

$$\Delta n = \frac{1}{2} n^3 r_{41} E \qquad 6.2$$

with n the refractive index, r_{41} the Pockels tensor, and E the transverse electric field strength. This equation applies for GaAs, InP and their alloys because for the zinc-blende type of crystals only r_{41}, r_{52}, and r_{63} are nonzero and all three tensors have the same value [1]. The value for r_{41} is given in literature to be $1.1\text{x}10^{-12}$ m/V at a photon energy of 1.38eV and a refractive index equal to 3.6 [2]. At an electric field strength of $1\text{x}10^5$ V/cm, this results in a refractive index change in the order of $2.3\text{x}10^{-4}$ which is negligible here.

6.2.3 The Franz-Keldysh effect

In case the electric field induced changes in the absorption are located near the edge of the bandgap, quadratic electro-optic effects like the Franz-Keldysh (FK) effect for bulk layers and the quantum-confined Stark (QCSE) effect for MQW semiconductor layers become dominant [1]. The FK effect is also known as the quadratic electro-optic effect because it is an even function in the electric field E. Both polarities of the high electric field result in strong tilting of both the conduction and valence band as shown in figure 6.1.

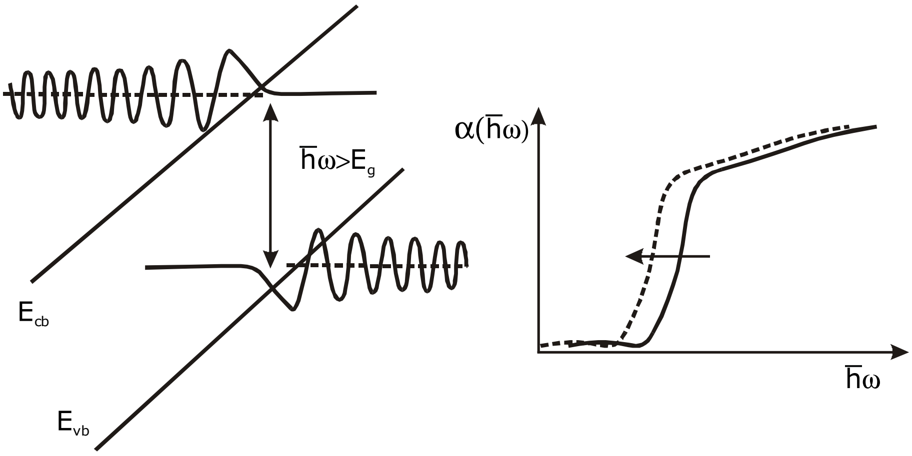

Figure 6.1: Schematic diagrams explaining the effect of the Franz-Keldysh effect within the energy band diagram (left) and the absorption function near the bandgap

Both wavefunctions penetrate slightly into the forbidden gap and their overlap increases with stronger tilting of the energy bands until a radiative recombination occurs with a photon energy smaller than the bandgap. The FK effect is therefore also known as photon assisted tunneling. The result is a net shift in the absorption edge towards lower energies and thus a matching shift in refractive index. The variation in effective bandgap is proportional to [4][5][6]:

$$\Delta E_g = -\frac{3}{2}(m_r)^{-1/3}(q\bar{h}E)^{2/3} \qquad 6.3$$

where $m_r = 1/(m_e^{-1} + m_{hh}^{-1})$ is the effective reduced mass and E the electric field strength. Assuming a $Al_{0.20}Ga_{0.80}As$ launcher, the effective masses are equal to m_e=0.08m_0, m_{hh}=0.56m_0, and m_r=0.070m_0. Equation 6.3 gives the reduction of the effective bandgap and thus the shift in the absorption edge at the electric field strength of 1x10^5 V/m to be -0.072eV. The FK effect therefore results in a substantial shift in the absorption edge and the matching shift in refractive index has to be determined. Casey and Panish state in their book the different plots for the refractive index of different $Al_xGa_{1-x}As$ compositions as a function of the photon energy [7: fig. 2.5-4]. These plots indicate a -72meV shift in bandgap around E_g=1.41eV to give a +0.03 shift in the refractive index for $Al_{0.20}Ga_{0.80}As$. Such an increase in refractive index will shift the transverse optical mode slightly towards the base layer. The slightly higher confinement inside the base will result in a small increase in internal losses which closes the loop again: the heating voltage modulates the electric field strength, which results in a shift in the absorption edge, which in its turn results in a shift in the launcher's refractive index. And that shift in the refractive index changes the transverse optical mode and increases the internal losses through slightly stronger coupling inside the base.

The increase in internal losses can be simulated by reducing the AlAs content inside the first part of the launcher by less than 5%. Using the same effective index method as used to calculate the transverse mode profiles of figures 3.17 and 3.18, the new transverse mode profile is calculated including the confinement factor inside the base and internal losses compensated for the FK effect (see table 6.1).

Table 6.1: *Overview of the contributions of the FK effect to the transverse waveguiding, the FK shift in the absorption edge of -72meV is modelled through a 5% lower AlAs content inside the pre- and main-launcher*

Parameter	Without electric field	With high electric field, compensated for FK effect
$\bar{x}$: $Al_xGa_{1-x}As$ pre- & main-launcher	0.20	0.15
confinement active layer Γ_{act}	28.4%	28.2%
confinement base Γ_{base}	6.2%	7.1
effective modal index n_{eff}	3.471	3.477
internal losses α_i	6.5 cm^{-1}	7.2 cm^{-1}
increase in α_i due to FK effect		0.7 cm^{-1}

The final verdict reads that the FK effect accounts for less than 1 cm^{-1}/V in heating voltage, and thus electric field induced, gain switching. The contribution of the FK effect to the lateral waveguiding is assumed to be even smaller due to the fact that only heating voltages V_{cb} greater than 0.5V are considered. The base current is small here and the transverse electric field will be relatively constant throughout the full width of the launcher.

6.2.4 The carrier-heating effect

After compensating for the Franz-Keldysh effect, heating voltage induced modal gain switching in the order of -6.1 to -4.3 cm^{-1}/V remains. At 28% confinement of the optical mode within the active layer, that corresponds to approximately -22 to -15 cm^{-1} material gain modulation per volt of the heating voltage V_{cb}. Table 6.2 gives the final overview of the predicted and measured values for heating voltage induced carrier heating, carrier heating induced gain switching and the overall heating voltage induced gain switching.

Table 6.2: *Overview of the predicted and measured values for the carrier heating and gain modulation efficiency. Also shown are the measured values compensated for the lateral diffusion of the electrons inside the active layer. (Note: all gain values are material gain.)*

Parameter	Predicted	Measured	Measurements compensated for lateral diffusion of electrons inside active layer
heating voltage induced carrier heating	36 K/V	13 K/V	33 K/V
carrier heating induced gain switching	-3.0 cm^{-1}/K	-1.7 to -1.2 cm^{-1}/K	-1.7 to -1.2 cm^{-1}/K
heating voltage induced gain switching	-108 cm^{-1}/V	-22 to -15 cm^{-1}/V	-55 to -38 cm^{-1}/V

The right column of table 6.2 indicates the measured values, which are compensated for the lateral diffusion of the electrons inside the active layer. Due to their high mobility and thus high diffusion constant the accelerated electrons share their additional kinetic energy with the full ensemble of electrons across the full width of the active layer. Even the electrons outside the lateral confinement of the optical mode take up part of their kinetic energy. They are heated up but do not contribute in lowering the net gain. The measured heating efficiencies are therefore multiplied by W_b / W_e to denote attainable heating efficiencies when lateral carrier confinement structures like buried heterojunction current blocking layers are included in the device design.

Table 6.2 indicates that such a structure's heating voltage induced carrier heating will be close to the theoretical efficiency as predicted by the Monte Carlo simulation based on a launcher with the n-type doping spike inside the post-launcher (see figure 3.16). The carrier heating induced gain modulation on the other hand stays well below the theoretical values as predicted by figures 2.5 and 2.6.

6.3 Recommendations

The launcher's carrier heating efficiency has to be increased by lowering or even removing the launcher's n-type doping spike. One solution might be the switch to certain types of tunneling barriers between post-launcher and active layer. Hole tunneling currents are generally much lower than electron tunneling currents and the dip inside the conduction band might be avoided. Such a solution has the potential of doubling the carrier heating efficiency. Another benefit is the potential of injecting the electrons 'cold' into the active layer at a heating voltage V_{cb} equal to 0V and avoid the heating offset in kT_e at V_{cb}=0V as shown in figure 3.16 [8]. Care has to be taken for the conduction band barriers not to interfere with the carrier heating process. Adding buried heterojunction current blocking layers on either side of the active layer will maximize the lateral overlap between the optical mode and the active layer. It will reduce optical losses due to spontaneous recombination and improve the carrier heating efficiency as explained in the previous section.

The other solution is to switch to a collector-up design in which the electrons are still accelerated inside the launcher before entering the active layer but in which the launcher, active layer, p-cladding and p-collector contact are now located on top of the base [9]. The width of these layers can now be narrowed to match the required lateral optical mode either through etching or other types of current blocking mechanisms. Besides improved carrier heating efficiency, the other expected benefit is improved lateral uniformity of the holes injected from the top collector contact into the active layer and thus improved lasing efficiency. This solution will slightly reduce the complexity of the hot electron injection laser again and bring it in line with conventional diode lasers with top p-contacts and bottom n-contacts on top of either n-type or S.I. GaAs substrates.

To become a viable option for fiber communication, it is also recommended to transfer the design of the hot electron injection laser to the InGaAsP/InP or InAlGaAs/GaAs material systems with strained MQW active layer to improve the laser's efficiency. Carrier heating also improves with a narrowing of the bandgap. The quantum wells will make the carrier heating less direct through delayed thermalization, meaning that the modulation frequency will have to be reduced slightly. The required buried heterojunction current blocking layers will benefit both the laser's quantum efficiency and the carrier heating efficiency.

References

[1] L.A. Coldren and S.W. Corzine, *Diode lasers and photonic integrated circuits*, Wiley Interscience, 1995.

[2] A. Dargys and J. Kundrotas, *Handbook on physical properties of Ge, Si, GaAs, and InP*, Science and Encyclopedia Publishers Vilnius, 1994.

[3] K. Hess, *Advanced theory of semiconductor devices*, Prentice-Hall, 1988.

[4] S.G. McMeekin, M.R.S. Taylor, B. Vögele, C.R. Stanley, and C.N. Ironside, "Franz-Keldysh effect in an optical waveguide containing a resonant tunelling diode," *Appl. Phys. Lett.*, vol. 65, pp. 1076-1078, 1994

[5] R.G. Hunsperger, *Integrted optics, theory and technology*, Springer, 1984.

[6] C.R. Pollock, *Fundamentals of optoelectronics*, IRWIN, 1995.

[7] H.C. Casey and M.B. Panish, *Heterostructure lasers. Part A: fundamental principles*, Academic Press, 1978.

[8] D. Klotzkin, X. Zhang, P. Bhattacharya, C. Caneau, and R. Bhat, "Carrier dynamics in high-speed (f-3dB > 40GHz) 0.98-µm multiquantum-well tunneling injection lasers determined from electrical impedance measurements," *Photon. Technol. Lett.*, vol. 9, pp. 578-580, 1997.

[9] G.L. Belenky, P.A. Garbinski, S. Luryi, M. Mastrapasqua, A.Y. Cho, R.A. Hamm, T.R. Hayes, E.J. Laskowski, D.L. Sivco, and P.R. Smith, "Collector-up light-emitting charge injection transistors in n-InGaAs/InAlAs/p-InGaAs and n-ÏnGaAs/InP/p-InGaAs heterostructures," *J. Appl. Phys.*, vol. 73, pp. 8618-8627, 1993.

Appendix A:

Process overview

A.1 REPETITIVE PROCESSING STEPS

A.1.1 Handling

Handling	**Comments**
Rinsing, developing, and lift-off	In quartz basket with teflon inlay
Etching	Upside down in peg-shaped etch holder

A.1.2 Cleaning

Cleaning	**Comments**		**time (m:s)**
Spray with acetone	above waste container	CH_3COCH_3	0:30
Rinse in acetone	in quartz basket		2:00
Rinse in isopropyl alcohol	in quartz basket	$CH_3CHOHCH_3$	2:00
Blow dry with nitrogen		N_2	

A.1.3 Rinsing

Rinsing	**Target**
Rinse in D.I.-H_2O	time > 1 minute and resistance water > 5MΩ
Blow dry with N_2	

A.1.4 Lift-off of evaporated metal

Lift-off	**Comments**	**time (m:s)**
Ultrasonic vibrations	use quartz basket inside glass beaker with acetone	0:30
Spray with acetone	above waste container	0:10
Repeat the above		as long as effective
Ultrasonic vibrations	at bottom of the beaker glass containing acetone	as long as required
Clean the sides of the sample	using cotton buds and acetone	
Cleaning	see A.1.2	

A.1.5 Exposure

Exposure	**Equipment**	**Wavelength**	**Optical power density**
UV300	Karl Süss MJB3 mask aligner	λ=300nm	2.0 mW/cm^2
UV400	Karl Süss MJB3 mask aligner	λ=400nm	14.0 mW/cm^2

A.1.6 Photolithography S1805

S1805	Comment	Spin speed (rpm)	T (ºC)	time (m:s)
Resist spin-on	Microposit S1805	3000 (open-air spinner)		0:30
Soft-bake			95	5:00
Mask exposure	UV300, see A.1.5			0:25
Pre-bake			105	5:00
Develop	MP2401 : D.I.-H_2O (1:10)			0:45
Hard-bake	Only when etching		105	5:00

A.1.7 Photolithography AZ5214 Lift-off

AZ5214 Lift-off	Comment	Spin speed (rpm)	T (ºC)	time (m:s)
Resist spin-on	Microchemicals AZ5214e	5000 (open-air spinner)		0:30
Soft-bake			95	5:00
Flood exposure	UV300, see A.1.5			0:01
Pre-bake			105	5:00
Mask exposure	UV300, see A.1.5			0:30
Develop	AZ developer : D.I.-H_2O (1:1)			1:45

A.1.8 Photolithography AZ5214

AZ5214	Comment	Spin speed (rpm)	T (ºC)	time (m:s)
Resist spin-on	Microchemicals AZ5214e	3000 (open-air spinner)		0:30
Soft-bake			95	5:00
Mask exposure	UV400, see A.1.5			0:06
Pre-bake			105	5:00
Develop	AZ developer : D.I.-H_2O (1:1)			0:50

A.2 PROCESS FLOW FOR THE HOT ELECTRON INJECTION LASER

A.2.1 Alignment reference metal

Step	Comment
Cleaning the sample	see A.1.2
Photolithography AZ5214e lift-off	see A.1.7, using mask plate 0:AlignRef
Metal evaporation	Ti/Au (50/200nm)
Lift-off of the metal layer	see A.1.4

A.2.2 Emitter ridge etch

Step	**Comment**	**T (ºC)**	**time (m:s)**
Prepare citric acid	200mg of citric acid monohydrate + 200ml D.I.-H_2O. Temperature of the mixture will drop to ±6ºC. Keep stirring until solution reaches room temperature.		
Cleaning the sample	see A.1.2		
Photolithography S1805	see A.1.6, using mask plate 1:EmitEtch		
Selective citric acid - hydrogen peroxide etch (r=10, 10:1)	• through the emitter • selectively stop at AlAs etch stop layer • start with dip in D.I.-H_2O • wet transfer (drop of water clinging to surface) into the etch solution: $C_6H_8O_7 : H_2O_2$ (100 : 10ml) • etch sample upside down • etch rate ≈ 195nm/min	20	4:40 (800nm)
Selective hydrogen fluoride etch	• through the AlAs etch stop layer • selectively stop at $Al_{0.07}Ga_{0.93}As$ base layer • direct wet transfer from the citric acid - hydrogen peroxide solution into this etch solution: few drops of HF (48%) in 200ml D.I.-H_2O • etch sample upside down		short dip 0:02
Rinsing	see A.1.3		
Cleaning to remove resist	see A.1.2		

A.2.3 Base, launcher, and active layer etch

Step	**Comment**	**T (ºC)**	**time (m:s)**
Cleaning the sample	see A.1.2		
Photolithography S1805	see A.1.6, using mask plate 2:BAREtch		
Non-selective citric acid - hydrogen peroxide etch (r=10, 10:1)	• through the base, launcher, and active layer • stop non-selectively inside the pre-cladding layer • start with dip in D.I.-H_2O • wet transfer (drop of water clinging to surface) into the etch solution: $C_6H_8O_7 : H_2O_2$ (100 : 10ml) • etch sample upside down • etch rate ≈ 205nm/min	20	2:10 (445nm)
Rinsing	see A.1.3		
Cleaning to remove resist	see A.1.2		

A.2.4 Collector ridge etch

Step	Comment	T (ºC)	time (m:s)
Cleaning the sample	see A.1.2		
Photolithography AZ5214	see A.1.8, using mask plate 3:CladEtch		
Non-selective phosphoric acid - hydrogen peroxide - methanol etch (1:1:3)	• through the pre-cladding, cladding and first 100nm of the collector • stop non-selectively inside the collector contact layer • etch solution: $H_3PO_4 : H_2O_2 : CH_3OH$ (20 : 20 : 60ml) • etch sample upside down • etch rate ≈ 345nm/min	0	4:10 (1440nm)
Rinsing	see A.1.3		
Cleaning to remove resist	see A.1.2		

A.2.5 Base and collector ohmic contact evaporation

Step	Comment
Cleaning the sample	see A.1.2
Photolithography AZ5214e lift-off	see A.1.7, using mask plate 4:BaCoMet
Metal evaporation	Ti/Pt/Au (50/20/200nm), ohmic on p-type AlGaAs
Lift-off of the metal layer	see A.1.4

A.2.6 SiNx isolator deposit and etch

Step	Comment	T (ºC)	time (m:s)
Cleaning the sample	see A.1.2		
SiNx deposition using Plasma Enhanced Chemical Vapor Deposition (PECVD)	• Oxford Instruments System100 for PECVD • $[SiH_4] = 16.7$ sccm • $[NH_3] = 13.3$ sccm • p = 650 mTorr • $P_{RF} = 20$ W	300	18:55 (±250nm)
Photolithography AZ5214	see A.1.8, using mask plate 5:SiNxEtch		
Selective SiNx etching using Reactive Ion Etching (RIE)	• Oxford Instruments System100 for RIE • $[SF_6] = 10$ sccm • p = 40 mTorr • $P_{RF} = 10$W • etch rate ≈ 35nm/min	20	10:00
Cleaning to remove resist	see A.1.2		

A.2.7 Emitter ohmic contact evaporation

Step	Comment
Cleaning the sample	see A.1.2
Photolithography AZ5214e lift-off	see A.1.7, using mask plate 6:EmitMet
Ammonia dip to remove oxides	30 seconds dip in NH_3 : H_2O 1:10 (5:50ml)
Metal evaporation	Ge/Ni/Au (20/15/200nm), ohmic on n-type AlGaAs
Lift-off of the metal layer	see A.1.4
Rapid thermal annealing	1 minute at 400ºC in N_2-flow

A.2.8 Interconnect metal evaporation

Step	Comment
Cleaning the sample	see A.1.2
Photolithography AZ5214e lift-off	see A.1.7, using mask plate 7:InterCMet
Metal evaporation	Ti/Au (50/200nm)
Lift-off of the metal layer	see A.1.4

A.2.9 Post-processing steps

Step	Comment	T (ºC)	time (m:s)
Attach sample to holder	using hot wax	100	
Polishing to 160µm	using 3µm Al_2O_3 powder and D.I.-H_2O on glass disk	20	160µm (±18:00)
Rinsing			
Polishing to 140µm	using 1µm Al_2O_3 powder and D.I.-H_2O on velvet disk	20	140µm (±20:00)
Rinsing			
Polishing to ±100µm	using diluted bleach (NaOCl), polishing rate ±2µm/min	20	100µm (±20:00)
Rinsing			
Removing oxides	using 60 seconds dip in HCl (32%)	20	
Rinsing			
Remove sample from holder	using trichloro ethylene	80	
Rinsing in trichloro ethylene and isopropyl alcohol			
Backside metal evaporation	Ti/Pt/Au (50/20/200nm), ohmic on p-type AlGaAs		if required
Lift-off of the metal layer	see A.1.4		if required
Rapid thermal annealing	1 minute at 400ºC in N_2-flow		if required

Separate into bars	• place sample on plastic foil and cover with dustproof foil • create vacuum • apply pressure at 150ºC for 30 seconds • place notches for 300, 500, 750 and 1000µm long lasers using Loomis scriber at 1.5 PSI • cover sample with dustproof foil • place sample on rubber mat and/or bend metal foil • cleave sample into bars by rolling a steel rod across its backside		
Separate into single lasers	• place notches for dices using Loomis scriber at 1-1.5 PSI • cover sample with dustproof foil • break bar into dices using steel rod		
Place on TO5 header	• using EPO-TEK H20E epoxy • place laser on Cu-block • place Cu-block on TO5 header • bake epoxy glue in N_2-flow oven at 150ºC for 90 minutes		
Bonding	wedge-wedge bonding on Kulicke & Soffa 4123 bonder		

Summary

The novel Hot Electron Injection Laser (HEL), a three-terminal vertically integrated transistor-laser structure, is designed to investigate and possibly utilize the effects of carrier heating on the optical gain and wavelength chirp. Simulations show the potential of carrier heating assisted gain switching to directly modulate the optical field intensity at frequencies up to 100Ghz while minimizing the parasitic wavelength chirp. The HEL is designed to demonstrate these results through independent but complementary control over both the concentration and the energy of the electrons injected into the active layer. It utilizes a strong electric field to accelerate the electrons and distributes their energy inside the active layer. There the energy is used to modulate the material gain and to control the wavelength chirp. The electrons are heated and cooled by increasing or decreasing the energy of the injected carriers. Both the effectiveness of the launcher to increase the temperature of the electrons inside the active layer as well as the effect of higher electron temperatures on the material gain are investigated here.

The Hot Electron Injection Laser derives its properties from the vertical integration of a diode laser with a heterojunction bipolar transistor. Joining the layer stacks of these devices puts extra emphasis on the epitaxial design to ensure proper transistor and laser behavior as well as the required electron heating. The epitaxial design rules are deduced and explained. Fabricating the Hot Electron Injection Laser involves the actual epitaxial growth of the designed layer stack and the subsequent characterization of these layers. It also involves transferring the patterns of the mask design onto the grown wafer. The three-terminal Hot Electron Injection Laser differs strongly from any conventional two-terminal diode laser in that it puts stronger requirements on the epitaxial layers and that it requires the additional base contact to control the base potential and thus the electric field across the launcher. And in spite of its narrow elongated design, the processing should still result in homogeneous carrier injection and a constant base potential along the cavity of the laser.

The correct vertical integration of the transistor and the laser has proven to be the most challenging part of this thesis. The basic transistor current-voltage curves were measured first. The measurements continued by obtaining the optical properties like optical power versus current curves, threshold current densities and the optical spectrum. Finally these result were used to estimate the carrier heating efficiency. The measurement results indicate a certain level of heating voltage induced gain switching to be present. The possible effects on which that gain switching could be based are discussed and estimates for their relative contributions are given. The heating voltage induced carrier heating is within the range of carrier heating predicted by simulations based on the Monte Carlo method. Compensating for other possible electric field induced gain switching, such as the Electro-Optic or Pockels effect and the Franz-Keldysh effect, the remaining carrier heating induced gain switching is smaller than expected. Various improvements to the current implementation are discussed to increase the carrier heating induced gain switching.

Samenvatting

De nieuwe Hete Elektronen Injectie Laser (HEL), een verticaal geïntegreerde halfgeleider transistor-laser, is ontworpen om de effecten van de verhitting van de ladingsdragers op de optische versterking en golflengte variaties te onderzoeken en deze mogelijk te gebruiken. De resultaten van de simulaties geven duidelijk het potentieel van deze techniek weer en voorspellen directe modulatie van de optische intensiteit tot frequenties van tenminste 100GHz waarbij de variaties in de golflengte van de laser geminimaliseerd worden. De HEL is ontworpen om de resultaten van deze simulaties in de praktijk te bevestigen door middel van het onafhankelijk maar complementair sturen van zowel de concentratie als de energie van de elektronen die in de actieve laag van de laser geïnjecteerd worden. Het ontwerp maakt gebruik van een sterk elektrisch veld om de elektronen te versnellen en verdeelt deze kinetische energie daarna binnen de actieve laag. Deze extra energie wordt binnen de actieve laag gebruikt om de optische versterking te moduleren terwijl de golflengte van de laser zo constant mogelijk gehouden wordt. De elektronen worden verhit en koelen weer af door variaties in de energie van de geïnjecteerde ladingsdragers. Dit proefschrift onderzoekt zowel de effectiviteit van de structuur waarmee de ladingsdragers in de actieve laag verhit worden als het effect van de verhoogde elektronentemperatuur op de optische versterking.

De HEL dankt zijn eigenschappen aan de verticale integratie van een diodelaser en een heterojunctie bipolaire transistor. Het integreren van deze twee lagenpakketten legt extra druk op het epitaxiale ontwerp om het gewenste transistor- en lasergedrag alsmede de vereiste elektronenverhitting te bereiken. De vereiste epitaxiale ontwerpregels worden hier afgeleid en toegelicht. Het vervaardigen van de HEL vereist de epitaxiale groei van het ontworpen lagenpakket en vervolgens de karakterisatie van deze lagen om vast te stellen of het uiteindelijke lagenpakket het ontwerp correct benaderd. Het vereist ook het overzetten van het maskerontwerp op de halfgeleiderplak door middel van nat-chemisch etsen, het opdampen van contactmetalen en het neerleggen van dielektrisch isolerende lagen. De hete elektronen injectie laser verschilt substantieel van conventionele diodelasers door de extra beperkingen die opgelegd worden op het ontwerp en door het derde basiscontact dat vereist is voor het sturen van het elektrische veld binnenin de structuur. En ondanks het langwerpige ontwerp dient de uiteindelijke structuur te resulteren in homogene injectie van de ladingsdragers en in een constant basispotentiaal in de lengterichting van de laser.

De belangrijkste uitdaging van dit proefschrift was de correcte integratie van de transistor en de laser en de implementatie daarvan. Allereerst zijn de standaard stroom- en spanningskarakteristieken gemeten gevolgd door de optische eigenschappen zoals optisch vermogen, drempelstroomdichtheden en het optische spectrum. Deze resultaten zijn gebruikt voor het afschatten van de efficiëntie van de structuur in het verhitten van de ladingsdragers. Die indicaties laten een duidelijke hoeveelheid elektronenverhitting zien veroorzaakt door het variabele elektrische veld. De mogelijke oorzaken van deze elektronenverhitting worden besproken en hun relatieve bijdragen worden tevens afgeschat. De hoeveelheid verhitting van de ladingsdragers valt binnen het bereik van de verwachtingen zoals voorspeld door de, op de Monte Carlo methode gebaseerde, simulaties. Na compensatie voor hoog-elektrische veldeffecten zoals het Elektro-Optisch of Pockels effect en het Franz-Keldysh effect blijkt dat de variaties in de optische versterking veroorzaakt door de elektronenverhitting kleiner zijn dan verwacht. Verschillende oorzaken en oplossingen tot verbetering van de efficiëntie van de HEL worden vervolgens besproken.

Dankwoord

Promoveren is de eeuwenoude beproeving in een modern jasje. Slechts met doorzettingsvermogen en ondersteuning door collega's, vrienden en familie wordt deze succesvol doorlopen. Daarom allereerst dank aan Gerard Acket en Theo van de Roer voor jullie onuitputtelijke bijdragen aan dit proefschrift en de vele trips die jullie ook na de pensionering nog richting de TU/e hebben gemaakt. Hartelijk bedankt voor de fijne samenwerking. Gerard, excuses voor de files bij knooppunt Leenderheide. Theo, *no more though or within* en dít document is hierbij wel voltooid. Verder wil ik Theo van de Roer, Leon Kaufmann, Guido van Tartwijk, Fouad Karouta en Meint Smit bedanken voor het feit dat jullie mij, onder verschillende paraplu's, de gelegenheid hebben geboden dit onderzoek te verrichten. *Hoe Tan and Chennupati Jagadish, thank you very much for the fruitful discussions, the very pleasant cooperation and the excellent epitaxial material. I would also like to thank Valery Tolstikhin for the intense discussions regarding the Hot Electron Injection Laser.* Hierbij ook mijn dank aan wijlen Willem v.d. Vleuten voor de eerste epitaxiale groei binnen dit project.

Geen resultaat zonder goede sfeer en samenwerking. Daarom ook mijn dank aan mijn kamergenoten Omar, Bart en Mark voor de dynamische sfeer, luidruchtige bestanden en de brede discussies. Omar, het systeem is echt eenvoudiger dan je denkt! Boris en Eugenio, enorm bedankt voor jullie bijdragen aan het begrip van de faalmechanismen bij de eerste generaties van de transistor-laser. Erik-Jan, bedankt voor de vele hulp in nood om mijn hectische processen in de lucht te houden in de cleanroom. Helaas geen *fly-by*, *drop-down* of *clutser tool* meer op de Zwartkop. Judith, bedankt voor de selectieve citroenzuur ets. Ben en Tjibbe, bedankt voor het opzetten en draaiende houden van beide cleanrooms, zet de nieuwe echter maar een toontje lager. Barry, deze wervelwind zal niet meer door jouw cleanroom en chemiekasten blazen. Dankzij jou heeft deze elektrotechnicus echter veel opgestoken over de wondere wereld van de chemie. Bedankt daarvoor en tevens mijn dank voor de zeer bewerkelijke Polaron analysen. Thieu, enorm bedankt voor jouw briljante ideeën en zeer praktische meetopstellingen waarmee deze typische transistor-laser gekarakteriseerd kon worden. Hans en Hans, bedankt voor de jarenlange ondersteuning op een gebied waar deze *hacker* eigenlijk iets teveel vanaf wist. Marcel en Guido, wat een half miljoen aan SIMS analyse al niet oplevert: een urgent gevoel om snel met de groeier om de tafel te gaan zitten.

Geen resultaat zonder de ondersteuning vanuit de eigen familie en vrienden. Daarom ook mijn grote dank aan mijn ouders, Cor en Bertie, voor jullie steun door al die jaren heen, ook de zorgwekkende eerste jaren. Cora, David, Patricia en Ron, bedankt voor jullie steun op velerlei vlakken en momenten. Ide en Juul, het is tijd om naar de Efteling te gaan. Rudolf, al die uithoeken van Europa, ook qua hoogtemeters, zijn nu prachtige herinneringen. Rob, Carl en Marton, tijd om ergens gezellig onderuit te zakken. Guido en Jean Paul, tijd om weer een pilsje te pakken en de discussie voort te zetten: een lap grond in Mexico of Barcelona, een toekomst in Azië of toch de *future*.

Diego, Pili (sogra bona!), Marta i granini (la iaia): moltes gràcies per acollir-me a la vostra família amb els braços oberts, per oferir-me una llar on passar les vacances, relaxar-me i carregar les piles, i per preparar-me un llenguado i unes gambes que estan per llepar-se els dits. Aquí, i per escrit, declaro la guerra a les llenties! Per últim, però no per això menys important, vull donar les gràcies a l'Ariadna: el teu carinyo i suport m'han donat la força necessària per acabar aquesta tesi que, a partir d'avui, ja no podràs comparar amb la Sagrada Família. ¡Misión cumplida!

Curriculum Vitae

Roger Hoskens was born in Bladel, The Netherlands, on July 7th, 1971. After graduating with honours from Shawnee High School (Lima, Ohio, USA), he studied electronics at the Technische Universiteit Eindhoven, The Netherlands. For his thesis, he realized the first solid-state self-pulsating diode laser to incorporate a thin quantum-well absorbing layer located just above the active layer and which serves as an optical saturable absorber. The research was carried out at the Philips Optoelectronics Centre (later JDS Uniphase) of Philips Research in Eindhoven, The Netherlands. In 1997, he accepted the position of scientist at the Technische Universiteit Eindhoven working on the first vertically integrated hot electron injection laser for complementary carrier and energy modulation induced direct gain switching. In 2001, he joined Genoa B.V., a start-up company with headquarters in Fremont (California, USA). As a development engineer he worked on the design, the modelling and the data analysis of the semiconductor linear optical amplifier. In 2003, he joined the Technische Universiteit Eindhoven as a scientist. Together with TNO FEL (The Hague, The Netherlands), he worked on AlGaN/GaN based high-frequency and high-power amplifiers and more specifically on passive circuits on AlN substrates. In 2005, he accepted the position of LED architect at Philips Lighting in Eindhoven, The Netherlands, where he now works on various lighting applications of solid-state lighting.

List of publications

R.C.P. Hoskens, T.G. van de Roer, E. Smalbrugge, J.J.M. Kwaspen, V.I. Tolstikhin, H.H. Tan, C. Jagadish, and G.A. Acket, “Hot Electron Injection Laser: Controlled Carrier-Heating Induced Gain Switching,” *Proc. of the Conference on Optoelectronic and Microelectronic Materials and Devices*, COMMAD 2004, December 8-10 2004, Brisbane, Australia.

J.J.M. Kwaspen, R.C.P. Hoskens, B. Jacobs, and M.C.J.C.M. Krämer, “A Universal Test Set for DC and Pulsed I-V Characterization of Various Semiconductor Devices,” *Proc. GAAS 2002*, 23-27 september 2002, Milano.

R.C.P. Hoskens, T.G. van de Roer, and G.A. Acket, “Hot Electron Injection Laser: The Internal Base Potential,” *Proc. of the 25th Workshop on Compound Semiconductor Devices and Integrated Circuits*, WOCSDICE 2001, May 27-30 2001, Cagliari, Sardinia.

R.C.P. Hoskens, T.G. van de Roer, E. Smalbrugge, V.I. Tolstikhin, and A. Förster, “Hot Electron Injection Laser: Vertically Integrated Transistor-Laser Structure for High-Speed, Low-Chirp Direct Modulation,” *Proc. 3rd STW Workshop on Semiconductor Advances for Future Electronics*, SAFE 2000, 29-30 November 2000, Veldhoven, The Netherlands, pp. 65-68.

R.C.P. Hoskens, T.G. van de Roer, V.I. Tolstikhin, and A. Förster, “Hot Electron Injection Laser: Vertically Integrated Transistor-Laser Structure for High-Speed, Low-Chirp Direct Modulation,” *Proc. 13th Annual Meeting of the IEEE Lasers and Electro-Optics Society*, LEOS 2000, 13-16 November 2000, Rio Grande, Puerto Rico, pp. 444-445.

R.C.P. Hoskens, T.G. van de Roer, E. Smalbrugge, V.I. Tolstikhin, and A. Förster, “Hot Electron Injection Laser: Vertically Integrated Transistor-Laser Structure for High-Speed, Low-Chirp Direct Modulation,” *Proc. 5th Annual Symposium of the IEEE/LEOS Benelux Chapter. 30 October 2000*, Delft, The Netherlands, pp. 235-238.

R.C.P. Hoskens, V.I. Tolstikhin, A. Förster, and T.G. van de Roer, “Vertically Integrated Transistor-Laser Structure, take 2,” *Proc. 24th Workshop on Compound Semiconductor Devices and Integrated Circuits*, WOCSDICE 2000, 29 May - 2 June 2000, Aegean Sea, Greece.

T.G. van de Roer, V.I. Tolstikhin, and R.C.P. Hoskens, “Monte Carlo Simulation of Electron Transport in a Hot-Electron Laser,” *Proc. 26th General Assembly of the International Union of Radio Science*, URSI XXVI, Toronto, Canada, 13-21 August, 1999, p. 247.

R.C.P. Hoskens, B. Ljevar, G. Archontopoulos, V.I. Tolstikhin, and T.G. van de Roer, “Design and First Results on a Vertically Integrated Transistor-Laser Structure for High-Speed Low-Chirp Modulations,” *Proc. 22nd Workshop on Compound Semiconductor Devices and Integrated Circuits*, WOCSDICE 99, Chantilly, France, 26-28 May, 1999, pp. 95-96.

R.C.P. Hoskens, T.G. van de Roer, and V.I. Tolstikhin, “Vertically Integrated Transistor-Laser Structure for High-Speed Low-Chirp Modulation,” *Proc. 1st STW Workshop on Semiconductor Advances for Future Electronics*, SAFE 98, Mierlo, The Netherlands, 25-26 November 1998, p. 21.

T.G. van de Roer, V.I. Tolstikhin, and R.C.P. Hoskens, “Monte Carlo Simulation of Electron Transport in a Hot Electron Laser,” *Proc. 6th International Conference on Simulation of Devices and Technologies*, Cape Town, South Africa, 14-16 October 1998, pp. 97-100.

R.C.P. Hoskens, T.G. van de Roer, C.J. van der Poel, and H.P.M. Ambrosius, “Self-pulsating lasers with QW saturable absorber,” *Appl. Phys. Lett.*, vol. 67, pp. 1343-1345, 1995.

R.C.P. Hoskens, T.G. van de Roer, C.J. van der Poel, and H.P.M. Ambrosius, “Self-pulsating lasers with QW saturable absorber,” *Proc. 2nd Int. Workshop on High Performance Electron Devices for Microwave and Optoelectronics*, EDMO '94, London, U.K., 14 november 1994, pp. 114-121.